

https://dspace.org/

# Efficiency gain of the solar trough receiver using different optically active layers

**Mohamed, Khaled Shehata Philippe**

**2019**
https://hdl.handle.net/10539/29548

Downloaded from a DSpace repository. https://dspace.org/

# EFFICIENCY GAIN OF THE SOLAR TROUGH RECEIVER USING DIFFERENT OPTICALLY ACTIVE LAYERS

Khaled Shehata Baiuomy Mohamad

Supervised by: Professor Philippe Ferrer
University of Witwatersrand

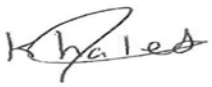
Johannesburg, 24th October 2019

*A dissertation submitted for the fulfillment of the requirements of the degree of Doctor of Philosophy to the Faculty of Science, University of Witwatersrand*



## Declaration

I declare that this thesis is my own, unaided work. It is being submitted for the Degree of Doctor of Philosophy at the University of the Witwatersrand, Johannesburg. It has not been submitted before for any degree or examination at any other University.

Student: Khaled Shehata Baiuomy Mohamad 

Supervisor: Professor Philippe Ferrer

## Dedication

To my family.

# Presentations arising from this study

**Paper Presentation**, "Thermal performance analysis of novel alternative designs for parabolic trough solar collector," 64th Annual Conference of the South African Institute of Physics (July 2019).

**(Granted an award for the best Ph.D. oral presentation in Applied Physics division)**

**Paper Presentation**, "Experimental and numerical study of a cavity and hot mirror receiver of the parabolic trough collector," 63rd Annual Conference of the South African Institute of Physics (June 2018).

**Invited presentation**, "Parabolic trough Efficiency gain through the use of a cavity absorber with a hot mirror," Material and Energy research group, workshop, (November 2017).

**Invited Presentation,** "Experimental and Numerical Heat Transfer Analysis of Cavity absorber and The Application of Different Optically Active Layer for Parabolic Solar Trough Concentrator," Physics school, Wits University, (October 2017).

**Paper Presentation**, "Experimental and Numerical Heat Transfer Analysis of Cavity absorber and The Application of Different Optically Active Layer for Parabolic Solar Trough Concentrator," 62nd Annual Conference of the South African Institute of Physics (July 2017).

**(Granted an award for the best Ph.D. oral presentation in Applied Physics division)**

# Publications and patents arising from this study

## Patent

**Khaled Mohamad**, Philippe Ferrer, "Thermal radiation loss reduction in a parabolic trough receiver by the application of a cavity mirror and a hot mirror coating" International Patent Application No. PCT/IB2019/053531 " [1].

## Papers

**Mohamad K** and Ferrer P. Parabolic trough efficiency gain through the use of a cavity absorber with a hot mirror *Appl. Energy* **238** 1250–1257. 2019 [Published][2].

**Mohamad K** and Ferrer P. Computational comparison of a novel cavity absorber for parabolic trough solar concentrators. Proc. 62th Annu. Conf. South Afr. Inst. Phys. SAIP2017 [Published][3].

**Mohamad K** and Ferrer. Experimental and Numerical Measurement of the thermal performance for parabolic trough solar concentrators. Proc. 63th Annu. Conf. South Afr. Inst. Phys. SAIP2018 [Published][4].

Kaluba V.S, **Mohamad K,** and Ferrer P. Experimental and simulated Performance of Heat Mirror Coatings in a Parabolic Trough Receiver. Applied Energy Journal. 2019 [Submitted] [5].

**Mohamad K** and Ferrer P. Cavity receiver designs for parabolic trough collector. Renewable & sustainable energy Journal. 2019 [Forthcoming] [6].

**Mohamad K** and Ferrer P. IR Reflection mechanism inside the annulus between two concentric cylindrical tubes . Renewable & sustainable energy Journal. 2019 [Forthcoming][7]

**Mohamad K** and Ferrer P. Guide for the properties of the materials required for the parabolic trough collector receiver. Applied Energy Journal. 2019 [Forthcoming].

**Mohamad K** and Ferrer P. Experimental and numerical study analysis of the thermal performance of novel alternative designs for parabolic trough solar collector. Renewable & sustainable energy Journal. 2019 [Forthcoming].

# Abstract

The Parabolic Trough Collector (PTC) technology is the most widely used Concentrated Solar Power (CSP) technology. This is due to its maturity, promising cost-effective investments and the possibility to be hybridized with fossil fuels or other renewable power plants. Furthermore, it ensures the best land use among CSP technologies.

The PTC receiver unit is the central component of the solar collecting plant, which is designed to absorb a large amount of the concentrated solar irradiation and minimize the thermal and optical losses. The research of finding an optimum design of the receiver unit that provides higher thermal and optical efficiency than the alternatives is a very active area of research in this field. The receiver unit with high efficiency will help to maximize electricity production and to reduce the cost of thermal storage due to a decrease in the requirements of the storage quantity. In addition, it will achieve optimum plant temperature within a shorter length, thus reducing the needed receiver unit length.

The alternative optimized PTC receiver in this work is a novel design of a mirrored cavity receiver with a hot mirror application. The design incorporates different optically active layers in conjunction with a cavity absorber. The cavity geometry and a hot mirror coating at the aperture enable heightened retention of thermal radiation in the receiver.

The design was analyzed numerically and studied experimentally. Novel aspects of the background theory for the design were presented and implemented in a simulation code. Three experimental setups, including the cavity receiver unit, were introduced. The experimental results were compared to our model and simulation results. It was seen that the correspondence between the experiments and simulation results was encouragingly close, and we proceeded to investigate simulations of the performance regarding the receiver design. The simulation results for receiver temperature profiles, heat transfer fluid temperature, and efficiencies were shown. It was seen that our proposed design had advantages in terms of thermal behavior over conventional designs in that it could exceed the heat transfer fluid temperature and the efficiency of existing alternatives.

# Acknowledgments

The work accomplished in this thesis could not have been any easier without the support of many people and organizations. Firstly, I would to deeply thank my supervisor, Professor Philippe Ferrer, for his enduring patience, trust, and encouragement. Your guidance and insight made executing this study more bearable. “You always lifted me up”.

To John, Vincent and all who helped me in the Mechanical workshop at physics school. To my friends I met during the course of our study, I appreciate the companionship and sharing moments of difficulties. You all could rise to the occasion whenever called upon.

Lastly, I would like to thank the following entities for their kind support: MERG (Materials for Energy Research Group) and MITP (Mandelstam Institute for Theoretical Research), at the University of the Witwatersrand.

# TABLE OF CONTENTS

**Declaration** ..... ii

**Dedication** ..... iii

**Presentations arising from this study** ..... iv

**Publications and patents arising from this study** ..... v

**Abstract** ..... vi

**Acknowledgments** ..... vii

**List of figures** ..... xi

**List of tables** ..... xiv

**Chapter 1 : Introduction** ..... 1

1.1 Introduction ..... 1
1.2 Concentrated Solar Power (CSP) ..... 1
1.3 Parabolic Trough Collector (PTC) technology ..... 3
1.3.1 PTC components, materials, and physical aspects. ..... 4
1.4 Problem statement ..... 8
1.5 Objective and research justification ..... 8
1.5.1 Specific objectives ..... 9
1.5.2 Some of the research questions ..... 9
1.6 Research organization ..... 10

**Chapter 2 : Literature review** ..... 11

2.1 Introduction ..... 11
2.2 Thermal radiation ..... 11
2.3 Solar radiation ..... 12
2.3.1 Sun Geometry ..... 13
2.3.2 Sun Tracking System ..... 15
2.4 The Parabolic Trough Collector ..... 16
2.4.1 Some of the conventional receiver unit problems and their solutions ..... 16
2.4.2 Cavity receiver overview ..... 18
2.5 The proposed design of the receiver unit ..... 30
2.5.1 Hot mirror coatings and its application on the conventional receiver ..... 30
2.5.2 The proposed cavity design with the hot mirror application ..... 32

**Chapter 3 : The theoretical model of the cavity receiver with a hot mirror** ..... 34

3.1 Introduction ..... 34
3.2 The cavity receiver design description ..... 34
3.3 Descriptions of the heat fluxes ..... 34
3.4 Discretization of the receiver unit ..... 35
3.5 The description of the heat transfers ..... 35
3.5.1 Conduction heat transfer ..... 36
3.5.2 Convection heat transfer ..... 37

3.5.3 Radiation heat transfers....40

**Chapter 4 : Derivation of the reflection mechanism....43**

4.1 Introduction....43
4.2 The reflected radiation terms....43
4.3 The first reflected radiation term $\dot{Q}_{IR,1\ ref}$....43
4.3.1 Summation of all first reflection contributions to $A_{il}$....45
4.3.2 The effect of the first reflection on the hot and IR mirrors control volumes....46
4.4 The second reflected radiation term $\dot{Q}_{IR,\ 2ref}$....47
4.4.1 The effect of the second reflection on the hot and IR mirrors control volumes....47

**Chapter 5 : Description of experiments and the adaptation of the theoretical model for the receiver unit operating indoor....49**

5.1 Introduction....49
5.2 Experiment setup description for the conventional receiver unit without coating "bare" and with hot mirror coating over the glass cover....49
5.3 Experiment setup description for the proposed cavity design....51
5.4 Theory adaption for the indoor experiment....53

**Chapter 6 : Numerical model and simulation implementation....55**

6.1 Introduction....55
6.2 The numerical models of the parabolic trough receiver unit....55
6.2.1 The numerical model of the receiver unit that operates with non-uniform solar flux....55
6.2.2 The numerical model of the receiver unit that operates with uniform heat flux....57
6.3 Simulation algorithm description....58
6.3.1 Simulation algorithm of the receiver unit that operates with non-uniform heat flux....58
6.3.2 The simulation algorithm for the receiver unit that operates with uniform heat flux....59
6.4 Simulation outputs and efficiency calculations....60

**Chapter 7 : Results and discussion....62**

7.1 Introduction....62
7.2 Convergence tests....62
7.2.1 Grid dependency....62
7.2.2 Convergence criterion....63
7.3 Code validation....64
7.3.1 Experimental validation of the simulation code with non-uniform heat flux....66
7.3.2 Experimental validation of the simulation code with uniform heat flux....68
7.4 The proposed Cavity design results....72
7.4.1 The effect of the different cavity opening sizes on the HTF temperature and the system efficiency....72
7.4.2 Effect of the reflectivity of the cavity mirror on the HTF temperature and the system efficiency....74
7.4.3 The role of the hot mirror coating over the cavity opening....75
7.4.4 The performance of the cavity design with a different mass flow rate....77
7.4.5 Evaluating the performance of the cavity design compared to selective coating and bare receiver....79

**Chapter 8 : Conclusion and recommendations....80**

8.1 Introduction....80
8.2 The mathematical model....80
8.3 The simulations....81

8.4 The experiments and simulation validation ..... 81
8.5 The results discussions ..... 82
8.6 Recommendations ..... 83
**References ..... 84**
**Appendix I ..... 91**
**Appendix II ..... 96**
**Appendix III ..... 101**
**Appendix IV ..... 104**
**Appendix V ..... 117**

# List of figures

Figure 1-1: CSP collector technologies [14]. 2
Figure 1-3: Direct normal irradiance map for CSP [21]. 3
Figure 1-4: Parabolic solar trough system [24]. 4
Figure 1-5 The relation between the focal point *f* and the rim angle $\psi$ at fixed aperture length a [25][13]. 5
Figure 1-6: Multi-layered mirror [26]. 6
Figure 1-7: Refletech films [27]. 6
Figure 1-8: Alanod mirror films [28]. 7
Figure 1-9: Structure of a parabolic trough receiver [34]. 8
Figure 2-1: Spectral blackbody emission power at different temperatures [42]. 12
Figure 2-2: The solar spectrum and its atmospheric influence [45]. 13
Figure 2-3: A plane with a tilt angle $\beta$, surface azimuth angle $\gamma$, incidence angle $\theta$, solar zenith angle $\theta z$and solar azimuth angle $\gamma s$ [44]. 14
Figure 2-4: Single-axis tracking mechanism of PTC [49]. 15
Figure 2-5: PTC tracking angles with North-South alignment [44]. 15
Figure 2-6: Schematic representation of the linear cavity receiver [36]. 19
Figure 2-7: Schematic representation of the cavity receiver design proposed by[77] 20
Figure 2-8: The modified design [42]. 21
Figure 2-9: Vertical cross-section of the cavity receiver [82]. 22
Figure 2-10: Vertical cross-section of the suggested optimized cavity receiver[82]. 22
Figure 2-11: Arc-shaped linear cavity receiver with a lunate channel [84]. 23
Figure 2-12: Elliptical cavity receiver [85]. 24
Figure 2-13: Heat and light flux distributions around the receiver cavity [85]. 24
Figure 2-14: Elliptical cavity with flat plate reflector [86] a) Structure schematic b) light distribution around the receiver. 24
Figure 2-15: Darkness of the modified elliptical cavity receiver under different tracking angle and PTC focal distances [86]. 25
Figure 2-16: Cross-section of the triangle cavity receiver [87]. 26
Figure 2-17: Cross-section of the V-shape cavity receiver [92]. 27
Figure 2-18: Cross-sectional of the trapezoidal cavity with round pipe absorber [95]. 29
Figure 2-19: Cross-sectional of the trapezoidal cavity with rectangular pipe absorber [95]. 29
Figure 2-20: The arrangement of multi-tube absorber with plate [97]. 29
Figure 2-21: The arrangement of multi-tube absorber with plate [97]. 29
Figure 2-22: The cross-section of the receiver unit with a hot mirror coating on the glass cove envelop [48]. 32
Figure 2-23: Cross-section of the cavity receiver with a hot mirror coating on the cavity aperture [52]. 33
Figure 3-1: Schematic representation of the cavity design with the possible heat transfer modes (except conduction). 34

Figure 3-2: Discretization of the absorber pipe and the cavity cover into control volumes. ..... 35
Figure 3-3: Heat exchange terms on the absorber pipe (AP) and the cavity cover (IRM or HM). ..... 36
Figure 3-4: Illustration of the view factor determination between two surfaces..... 41
Figure 3-5: Determination of the view factor in the discretized receiver unit using the crossed string method. .. 41
Figure 4-1: Simple schematic representation to show the mechanism of the first reflection between absorber pipe (AP) and hot mirror (HM). ..... 44
Figure 4-2: Discretize the HM into normal and offset CVs (the index in the axial direction is "l", see Figure 3-2). ..... 45
Figure 4-3: Absorber pipe control volume with index *i* receives reflected radiation from $Ai$, $Ai+1$ and $Ai-1$via reflection over $HMm$, $HMm+1$, and $HMm-1$, respectively. ..... 45
Figure 4-4: HM control volume received the emitted absorber pipe control volumes radiation (case 1). ..... 46
Figure 4-5: HM control volume received the emitted absorber pipe control volumes radiation (case 2). ..... 46
Figure 5-1: The receiver unit set up in the laboratory, behind a PERSPEX safety shield, on the left. On right, top: the heating element. Right center: vacuum pump (left) and variac, and temperature logging unit below. ..... 49
Figure 5-2: The right one-half of receiver unit. T represents the thermocouple position. ..... 50
Figure 5-3: The receiver unit set up in the laboratory. The vacuum pipe can be seen connected to the center. ... 52
Figure 5-4: A section of the receiver unit. Cavity cover, absorber pipe (AP), spacers, heaters, wiring, and thermocouples are shown. "T" represents the thermocouple position. ..... 52
Figure 5-5: Receiver unit cross-section. ..... 53
Figure 6-1: Illustration of the algorithm of the simulation code in case of the receiver that operates with non-uniform heat flux. Black arrows are for the primary processes execution and true conditions and the blue arrows, for the false and iterative conditions. ..... 59
Figure 6-2: Illustration of the algorithm of the simulation code in case of the receiver unit that operates with uniform heat flux. Black arrows are for the primary processes execution and the true conditions and the blue arrows, for the false and iterative conditions. The colored blocks indicate a difference to the previous algorithm. ..... 60
Figure 7-1: Convergence test of the control volumes (CVs) number to select the minimum number of CVs along the circumference. ..... 63
Figure 7-2: Convergence test at different convergence criterion values for the outer cover function. ..... 64
Figure 7-3: Convergence test at different convergence criterion values for the AP function. ..... 64
Figure 7-4: Convergence test at different values of the AP function CC for the simulation code of non-uniform solar flux case. ..... 64
Figure 7-5: Convergence test at different values of the outer cover function CC the simulation code of non-uniform solar flux case. ..... 64
Figure 7-6: Heat transefer fluid (HTF) temperature at zero value of solar irradiation, absorber material conductivity, and HTF convective heat transfer coefficient. ..... 65
Figure 7-7: The absorber pipe surface temperatures at zero emissivity of the absorber pipe. ..... 66
Figure 7-8: Temperature variation along the axial direction at different positions across the circumference of the AP. ..... 67
Figure 7-9: Temperature profile around the AP circumference at 6 m length. ..... 68

Figure 7-10: Temperature profile around the AP circumference at 8 m length. ..... 68
Figure 7-11: Temperature profile around the GC circumference at 4 m length..... 68
Figure 7-12: Experimental and simulated results for the temperature profile at different heating powers for the receiver unit without any coating, designated "bare". ..... 70
Figure 7-13: Simulated and experimental results of the receiver unit coated with a hot mirror at various temperatures ..... 70
Figure 7-14: Comparison between experimental results from the bare and hot mirror receiver. The hot mirror absorber pipe is capable of reaching much higher temperatures at the same power input. ..... 71
Figure 7-15: Experimental and simulated results of the temperature profile at different heating powers for the cavity receiver unit ..... 72
Figure 7-16: Cross-section of the cavity design with different cavity opening sizes..... 73
Figure 7-17: HTF temperature as a function of the length of the receiver unit with different cavity opening sizes ..... 73
Figure 7-18: Efficiency of the parabolic trough collector with the cavity design of the receiver unit..... 74
Figure 7-19: HTF temperature as a function of the length of the receiver with different cavity mirror reflectivity. ..... 75
Figure 7-20: Efficiency of the parabolic trough collector with different cavity mirror reflectivity..... 75
Figure 7-21: HTF temperature as a function of the length of the receiver with a hot mirror coating and without over the cavity opening..... 76
Figure 7-22: Efficiency of the parabolic trough collector with and without hot mirror coating over the cavity opening. ..... 76
Figure 7-23: The surface temperature of the outer surface of the cavity receiver at length 100 m..... 77
Figure 7-24: The surface temperature of the outer surface of the cavity receiver at length 200 m..... 77
Figure 7-25: HTF temperature as a function of the length of the receiver with different values of the mass flow rate of the HTF. ..... 78
Figure 7-26: The total efficiency of the system as a function of the length of the receiver with different values of the mass flow rate of the HTF (cavity with 30 CVs). ..... 78
Figure 7-27: HTF outlet temperature for 375 K inlet temperature of different designs..... 79
Figure 7-28: Integrated efficiency of the parabolic trough collector with different designs..... 79
Figure 7-29: The total efficiency of the system as a function of the length of the receiver with different designs. ..... 79

# List of tables

Table 5-1: List of different equipment/instrument used with error involved. ..... 51
Table 7-1: Design parameters of the SEGS LS2 used in our simulation. ..... 66
Table 7-2: Optical properties of the absorber pipe and outer cover of the receiver unit at different scenarios [50][29][26]. ..... 69
Table 7-3: Results and relations that are related to Figure 7-25. ..... 78
Table 0-1: List of all PTC in the world at the time of writing [124]. OP, U.D, U.C, and N.OP mean operating, under development, under construction, and currently non-operation. ..... 91

# ABBREVIATIONS

| | |
|---|---|
| **A** | Area |
| **AP** | Absorber pipe |
| **CSP** | Concentrated solar power |
| **CV** | Control volume |
| **CC** | Convergence criterion |
| **DSG** | Direct steam generation |
| **ET** | Equation of time |
| **FVM** | Finite volume method |
| **GC** | Glass cover |
| **HM** | Hot mirror |
| **HCE** | Heat collecting element |
| **HTF** | Heat transfer fluid |
| **IEA** | International energy agency |
| **IR** | Infrared radiation |
| **ITO** | Indium Tin Oxide |
| **IRM** | Infra-red reflective mirror |
| **LST** | Local standard time |
| **$MW_e$** | Megawatts electricity |
| **$MW_{th}$** | Megawatts thermal |
| **PTC** | Parabolic trough collector |
| **RU** | Receiver unit |
| **SC** | Selective coating |
| **SEGS** | Solar electricity generating system |
| **ST** | Standard time |
| **UNFCCC** | United Nations framework conference on climate change |

# NOMENCLATURE

| | |
|---|---|
| $B_\lambda$ | Blackbody emissive power (W) |
| $C_p$ | Specific heat capacity |
| $DOY$ | Day of the year |

| | |
|---|---|
| **d** | Distance (m) |
| $dA_1$ | Differential area on a surface 1 |
| $F_{12}$ | View factor from emitting area 1 to receiving area 2 |
| $F_{km}^{HM,A}$ | View factor from "*k*" CV in HM to "*m*" CV in AP. |
| $\dot{F}$ | Mass flow rate kg/s |
| $G_s$ | Solar constant (W/m$^2$) |
| $I$ | Radiation intensity (W/m$^2$) |
| **K** | Kelvin scale (K) |
| $k_A$ | AP Thermal conductivity of a material |
| $k_{HM}$ **or** $k_{IRM}$ | HM or IRM Thermal conductivity of a material |
| **L** | Length (m) |
| $L_{st}$ | Local meridian where standard time is based |
| $L_{loc}$ | The meridian of the location |
| **LST** | Clock time or Local standard time |
| **N** | n$^{th}$ day of a year |
| $Nu$ | Nusset number |
| $P_{sun}$ | Total radiant emittance of the sun (W) |
| $Pr$ | Prandtl number |
| $\dot{Q}$ | Heat transfer rate (W) |
| $\dot{Q}_{cond}$ | Conduction heat flux (W/m$^2$) |
| $\dot{Q}_{conv}$ | Convection heat flux (W/m$^2$) |
| $\dot{Q}_{rad}$ | Radiation heat flux (W/m$^2$) |
| $\dot{Q}_{sol}$ | Solar irradiance (W/m$^2$) |
| $\dot{Q}_{A,\theta,m\pm1}$ | Conduction heat transfer rate along AP circumference |
| $\dot{Q}_{HM,\theta,m\pm1}$ | Conduction heat transfer rate along HM/IRM circumference |
| $\dot{Q}_{A,z,m\pm1}$ | Conduction heat transfer rate along AP length |
| $\dot{Q}_{HM,z,m\pm1}$ | Conduction heat transfer rate along HM/IRM length |
| $\dot{Q}_{A,r,m\pm1}$ | Conduction heat transfer rate along AP radial direction |
| $\dot{Q}_{HM,r,m\pm1}$ | Conduction heat transfer rate along HM/IRM radial direction |
| $\dot{Q}_{HM,sol}$ | Solar irradiance on HM (W/m$^2$) |
| $\dot{Q}_{A,sol}$ | Solar irradiance on AP (W/m$^2$) |
| $\dot{Q}_{A,HM,IR}$ | Infrared radiation from AP to HM/IRM (W/m$^2$) |
| $\dot{Q}_{HM,HM,IR}$, | Infrared radiation from HM/IRM to HM/IRM (W/m$^2$) |
| $\dot{Q}_{HM,A,IR}$ | Infrared radiation from HM/IRM to AP (W/m$^2$) |

| | |
|---|---|
| $\dot{Q}_{IR,refl}$ | Back reflected Infrared radiation |
| $\dot{Q}_{IR,1\,refl}$ | Singly reflected infrared radiation |
| $\dot{Q}_{IR,2refl}$ | Doubly reflected infrared radiation |
| $\dot{Q}_{HM,O,IR}$ | Infrared radiation from GC to Environment ($W/m^2$) |
| $\dot{Q}_{AF,conv}$ | Convection heat transfer rate from AP to HTF ($W/m^2$) |
| $\dot{Q}_{HM,O,conv}$ | Convection heat transfer rate from GC to Environment |
| $r_A$ | AP Radius |
| $r_{HM}$ | HM/IRM Radius |
| $Re$ | Renold's number |
| $R_{ij}^{A}$ | Radiation emitted from a point $ml$ on AP |
| **ST** | Solar time |
| $T_l^F$ | Temperature of the $(l)^{th}$ HTF control volume |
| $T_{ml}^{A}$ | Temperature of the *ml* AP control volume |
| $T_{ml}^{HM}$ | Temperature of the *ml* HM/IRM control volume |
| $T_{Sun}$ | Sun surface temperature |
| $T_f$ | Fluid temperature |
| **T** | Temperature |
| $h_f$ | Convective heat transfer coefficient for the HTF |
| $h_w$ | Convective heat transfer coefficient for the wind |
| **ΔL** | Difference in length (m) |
| $\Delta T$ | Difference in temperature (K) |
| $\Delta s_A$ | Arc length on AP (m) |
| $\Delta s_{HM}$ **or** $\Delta s_{IRM}$ | Arc length on HM or IRM (m) |
| $\frac{dT}{dx}$ | Temperature gradient along length (K/m) |

# GREEK LETTERS

| | |
|---|---|
| $\alpha_h$ | molecular diffusivity of heat |
| $\rho$ | Material density |
| $\varepsilon$ | Surface emissivity |
| $\eta$ | Efficiency |
| $\theta$ | Angle in radians |

| | |
|---|---|
| $\boldsymbol{\lambda}$ | Wavelength |
| $\boldsymbol{\delta\omega}$ | Solid Angle |
| $\boldsymbol{\mu}$ | viscosity |
| $\boldsymbol{\nu}$ | molecular diffusivity of momentum |
| $\boldsymbol{\sigma}$ | Stefan-Boltzmann constant ($5.67 \times 10^{-8}$ W/m$^2$K$^4$) |
| $\boldsymbol{v_w}$ | wind velocity |
| $\boldsymbol{\omega}$ | Hour angle |
| $\boldsymbol{\pi}$ | Pi |
| $\boldsymbol{\tau_\lambda}$ | Spectral transmissivity |
| $\boldsymbol{\rho_{HM,sol}}$ | Solar reflectivity on HM/IRM |
| $\boldsymbol{\rho_{A,sol}}$ | Solar reflectivity on AP |
| $\boldsymbol{\rho_{A,IR}}$ | Infrared reflectivity on AP |
| $\boldsymbol{\rho_{HM,IR}}$ | Infrared reflectivity on HM/IRM |
| $\boldsymbol{\rho_{A,IR}}$ | Infrared reflectivity on AP |
| $\boldsymbol{\alpha_{A,sol}}$ | Solar absorption on AP |
| $\boldsymbol{\alpha_\lambda}$ | Spectral absorptivity |

# Chapter 1 : Introduction

## 1.1 Introduction

Electricity and energy consumptions in the world are increasing rapidly due to demographic change, industry, and urbanization. For example, electricity consumption worldwide will double within 15-20 years [8]. The primary energy supply of most of the countries comes from fossil fuels, e.g., petroleum, natural gas, and coal. The continued use of fossil fuels to meet global energy needs not only depletes the resources but is also responsible for significant greenhouse gases such as $CO_2$ emissions. It was estimated that the global $CO_2$ emissions from fuel combustion were 32.31 Gt $CO_2$ in 2016. However, $CO_2$ emissions were relatively stable between 2013 and 2016. The International Energy Agency found that $CO_2$ emission increased by 1.5% led by the European Union, India, and China in 2017. Most of these increases are related to the current industry-based economy[9]. The United Nations Framework Convention on Climate Change (UNFCCC) reached a landmark agreement (the "Paris agreement") to confront climate change and to force actions and investments needed for a low carbon future. The target of this agreement is to keep global temperature rise below 2 ℃ [10]. Despite, the $CO_2$ emission problem, the oil prices are expected to increase from $ 125/barrel in 2011 to $ 215/barrel in 2035 [11]. This is due to increasing the demand where the consumption is expected to grow from 87.4 Mb/d (million barrels per day) in 2011 to 99.7 Mb/d in 2035[11].

Moreover, nuclear power generation in the energy mix is decreasing due to catastrophic events such as the Fukushima nuclear power plant in 2011. The disturbance in some parts of North Africa and the Middle East have forced some countries to rethink and change their policies and refrain from building these nuclear power plants[11][12].

For these reasons, need for renewable energy has increased. According to the International Energy Agency, 50% of the new power infrastructure will be based on clean, sustainable energies by 2035. Making it the world's second-largest source of power generation [11][13]. It could deliver about 30% of the electricity needs by the year 2035[11][13]. Also, renewable energy with the current infrastructure development will contribute to an overall $CO_2$ reduction of 30% by 2050, compared to 2012 [11].

Concentrating Solar Power (CSP) technology is expected to be the fastest growing technology among the other renewable energy resources [14][15]. This technology is capable of satisfying the demand of electrical energy, as well as thermal energy and offering dispatchable power (it refers to the source of energy that can be used on-demand or at the request of power grid operators) on demand by integrating thermal energy storage or in hybrid operation [4][6].

## 1.2 Concentrated Solar Power (CSP)

The use of CSP has been reported since antiquity. One historic account mentions Archimedes repelling the invading Roman fleet from Syracuse using concentrated sunlight [16]. In 1615, the French engineer Salomon De Caux developed a small solar-powered motor consisting of glass lenses and an airtight metal vessel containing water and air [17]. In the 1860s, August Mouchet, a French mathematician, used a parabolic trough to produce

steam for the first solar-powered steam engine [17]. In 1913, the first CSP-plant, powered by a parabolic trough solar field, was installed at Al Maadi (Egypt)[18]. This CSP- plant was used for pumping water for irrigation [18]. In the 1960s, the focus shifted to photovoltaic for the space program. After 1970, interest in the CSP was renewed, boosting R&D activities, testing, and bringing CSP collector technology to the industrial and commercial level [19]. Numerous new CSP plants were built. The first largest commercial plants were built in California, USA, which operated throughout 1984-1991. Subsequently, CSP collector technology became popular in many countries such as Spain, China, and India.

Currently, one distinguishes between four CSP collector technologies, namely Solar Power Tower, Parabolic Trough Collector, Linear Fresnel Reflector, and Parabolic Dish, as shown in Figure 1-1. Generally, the CSP plant consists of three major subsystems a solar collector field, a solar receiver and a power conversion system. Storage and backup-up systems can be added to increase the capacity and enhance the performance [18]. Further, CSP is classified according to the type of the concentrator, such as a linear focus concentrator type and point focus concentrator type. Parabolic Trough Collector and Linear Fresnel Reflector utilize a linear focus concentrator, while Solar Tower and Parabolic Dish utilize a point focus concentrator [20].

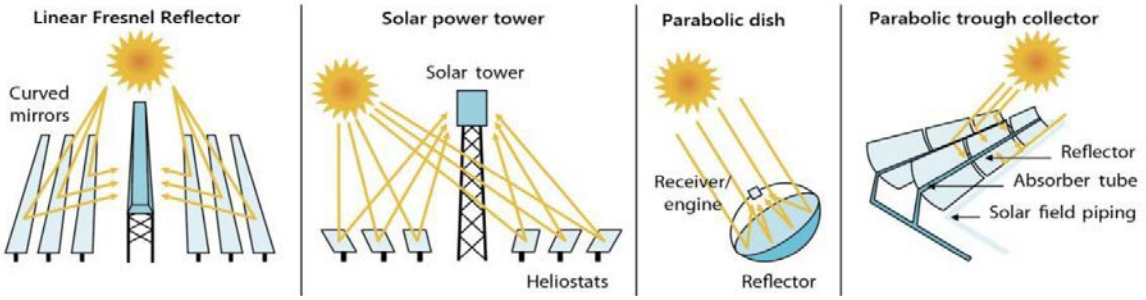



Figure 1-1: CSP collector technologies [15].

The suitability of building CSP plants depends on the region's solar radiation, especially Direct Normal Irradiance (DNI), the fraction of solar radiation which is not deviated by clouds, fumes or dust in the atmosphere and that reaches the Earth's surface as a parallel beam [18]. Solar flux density outside the atmosphere is 1367 W/m$^2$ and gets attenuated to an average value of about 1kW/m$^2$ on the earth's surface [21]. Figure 1-2 shows solar radiation distribution over the world. The countries that are located within the equatorial" Sun Belt", such as the Middle East, Arabia, Gulf countries, and California, get an enormous amount of available solar energy and are considered as an ideal for solar thermal power plant sites.

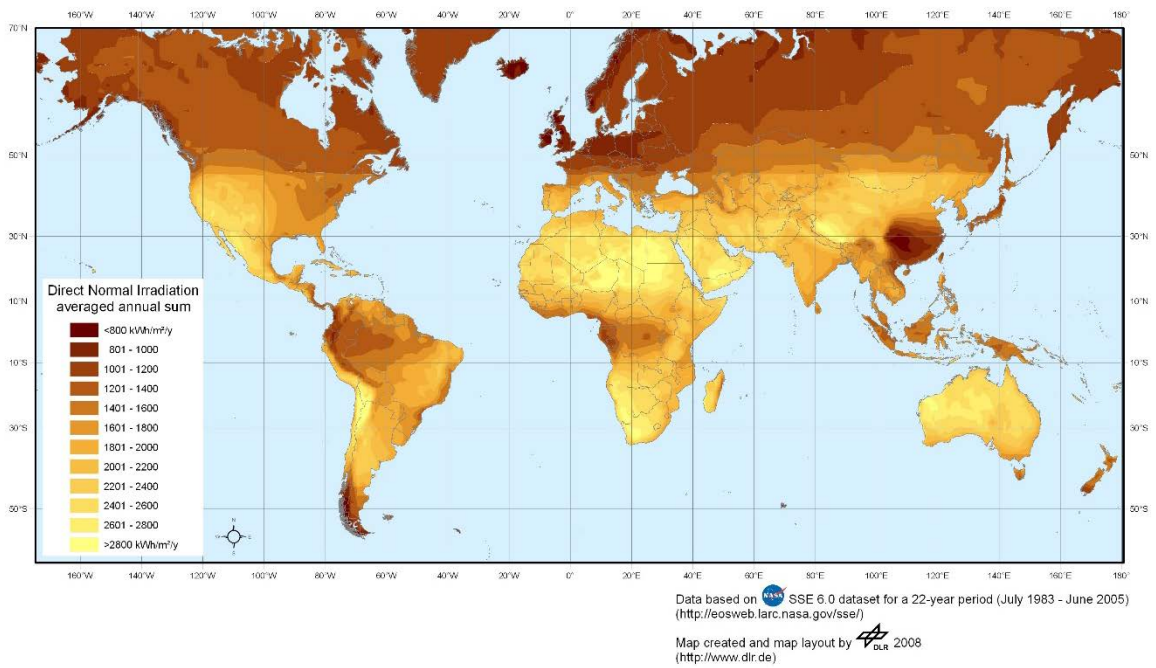



Figure 1-2: Direct normal irradiance map for CSP [22].

CSP technology has been utilized in 23 countries around the world at the time of writing [23]. The United States and Spain share the most installed CSP projects capacity worldwide.

## 1.3 Parabolic Trough Collector (PTC) technology

In PTC, Figure 1-3, the sunlight strikes the parabolic mirror of the PTC. The solar radiation is focused onto a focal line aimed at the receiver unit. The receiver heats up and in turn, imparts a significant portion of its heat to a Heat Transfer Fluid (HTF) circulating within. The hot HTF can be used to generate electricity through a steam cycle or in thermochemical applications, i.e., industrial processes (chemical, textile, and food industries).

At the time of writing, there are 86 out of 102 operational parabolic trough power plants worldwide, and the rest are under construction or development, mostly in Spain and the United States [23]. Up until 2016, the total installed capacity of PTC power plants in the United States and Spain are 1255.8 MW and 1871.9 MW, respectively [24]. A table of current PTC power plants worldwide is shown in Appendix I.

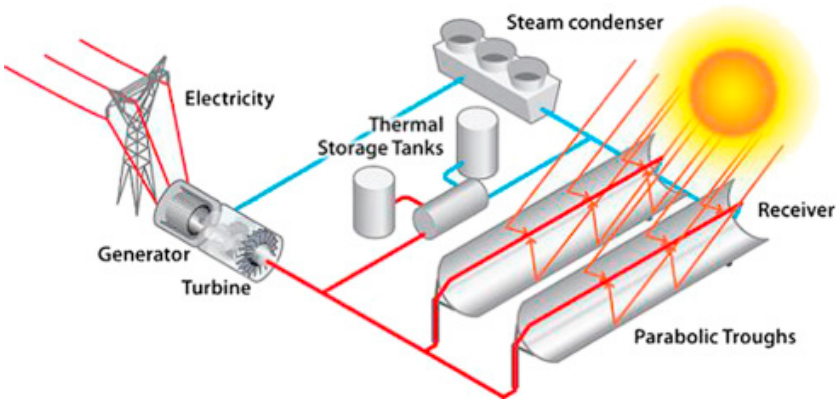



Figure 1-3: Parabolic solar trough system [25].

### 1.3.1 PTC components, materials, and physical aspects.

The collector of PTC is a cylindrical surface with a parabolic shape. More precisely, it is asymmetrical section of a parabola around its vertex [14]. The focal line of the parabolic trough is the line that connects the focal points of parabolic cross-sections along the trough length. The equation of the parabola involving the focal distance from the vertex of the parabola, *f*, is

$$y = \frac{1}{4f} x^2. \tag{1.1}$$

#### 1.3.1.1 The geometry

The geometry of the parabolic trough can be determined by four parameters - first, the length of the trough, which is the distance measured along its length. Second, the focal length, *f*, which is the distance between the focal point and the vertex of the parabola. Third, aperture width, a, which is the distance between one rim to the other. Forth, Rim angle,$\psi$, which is the angle between the optical axis (vertical line pass through the focal point and the vertex of the parabola) and the line between the focal point and the mirror rim. The three parameters a, *f*, and $\psi$, are related to each other, and their values can change the cross-section, shape and size of the parabolic trough, see Figure 1-4. $\psi$ is considered to be a critical parameter in the collector construction due to its effect on irradiance per meter of the receiver unit of PTC and in turn on the concentration ratio[14]. $\psi$ is expressed as a function of the ratio of aperture width *a* to the focal length *f* [14]:

$$\tan\psi = \frac{a/f}{2-\frac{1}{8}(a/f)^2}. \tag{1.2}$$

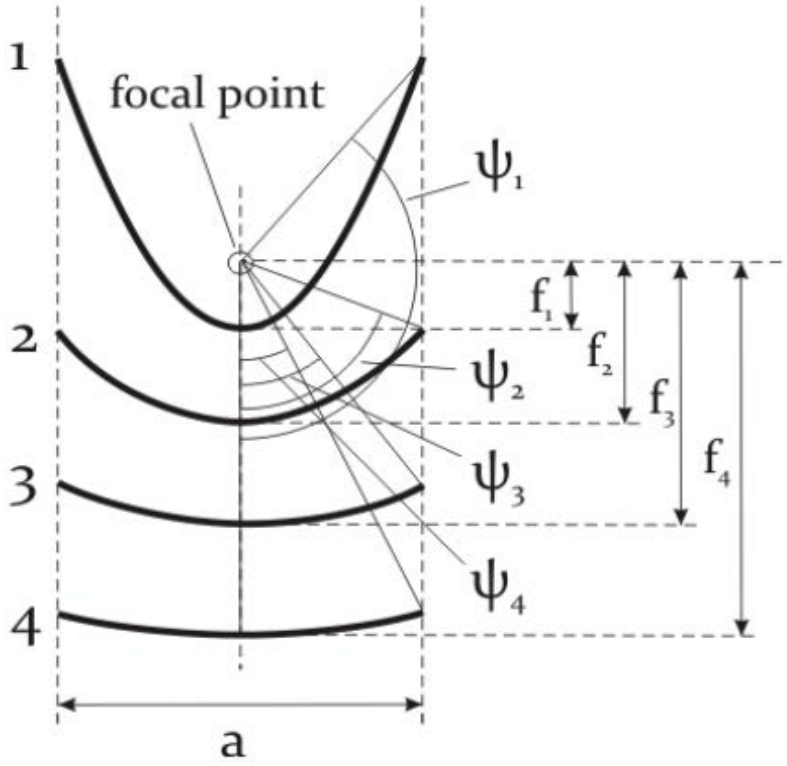



Figure 1-4 The relation between the focal point *f* and the rim angle $\psi$ at fixed aperture length a [26][14].

The central parameter of the collector is the concentration ratio, C. It is defined as the mean irradiance at the focal line to the direct normal irradiance at the aperture of the collector. Another useful parameter is the geometrical concentration ratio, $C_G$, which is the ratio of the collector aperture, $A_{ap,C}$, to the receiver area, $A_R$.

$$C_G = \frac{A_{ap,C}}{A_R} = \frac{a\,.\,l}{d\,.\,l} = \frac{a}{d} \quad , \tag{1.3}$$

where *l* is the receiver, or collector length and *d* is the diameter of the absorber pipe of the PTC receiver [14].

#### 1.3.1.2 Mirror materials

The main feature of the mirror material is its reflectivity. In solar applications, the solar spectrum is of interest. Researchers sometimes define the "solar weighted reflectivity", which is the fraction of solar energy that is reflected from the surface of a mirror. The reflection process can be a diffuse reflection or specular reflection due to the smoothness or texture of the surface. In a diffuse reflection, the incident light is reflected in a wide range of directions, while in the specular reflection, the angle of an incident light ray is equal to the angle of reflected ray. In this case the surface imperfections are smaller than the wavelength of the incident light. It is important that a reflecting surface is as specular as possible for a working solar concentrator. Different types of mirrors can be used for the collector of PTC, such as:

**Silver coated glass mirrors,** most of commercial parabolic trough power plants use them. This mirror is very durable, with its specular reflectivity hardly changing after more than ten years [14]. These mirrors have a multi-layered structure, as shown in Figure 1-5.

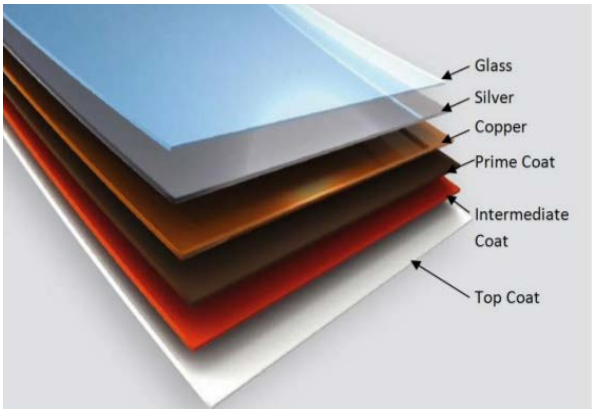



Figure 1-5: Multi-layered mirror [27].

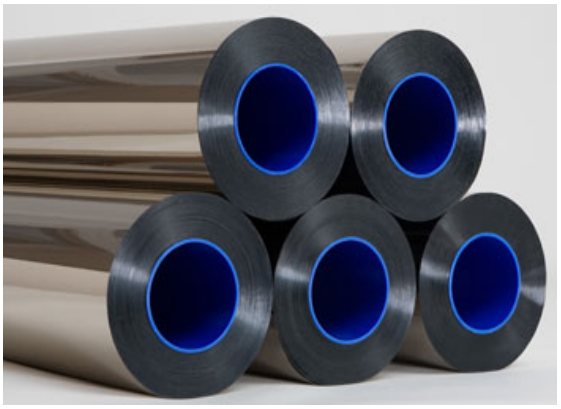


Figure 1-6: Refletech films [28].

The first layer below the glass is the reflective layer, i.e., the silver coating. Next to the silver layer is a protective layer from copper. Then, three epoxy layers are added, a prime, intermediate, and protective coat. The thickness of the complete mirror amounts to 4 or 5 mm. This mirror has an average solar weighted reflectivity 93.5%. The disadvantage of silver coated glass mirror is that it is not constructed in one piece, and they are composed of mirror facets. Ceramic pads with a bolt are glued on the back of the mirror facet for the mounting on the metallic bearing structure, which is an additional cost. Numerous efforts are underway to find alternative materials that could lower the cost of mirrors [14].

**Silver coated polymer films**, commercially known as ReflecTech. Mirrors with ReflecTech have been tested since 2002 in the SEGS plants in California. They come in rollable sheet form, which can be applied to any non-porous smooth surface, see Figure 1-6. It is claimed that ReflecTech offers a considerable economic advantage compared to glass mirrors. The advantages of this mirror type were not being susceptible to breakage and indicated the reflectivity of 94%. Skyfuel Company commercializes this mirror technology (ReflecTech).

**Front side aluminum mirrors**, this mirror film is manufactured by Alanod Company, see Figure 1-7. It consists of an aluminum reflective layer, an anodized layer beneath and above as well as further protective coatings. The PVD coating is applied to achieve a maximum total light reflection. A Nano-composite protects the mirror in a coil-coating process. This mirror type has a value of 95% of total light reflection [29].

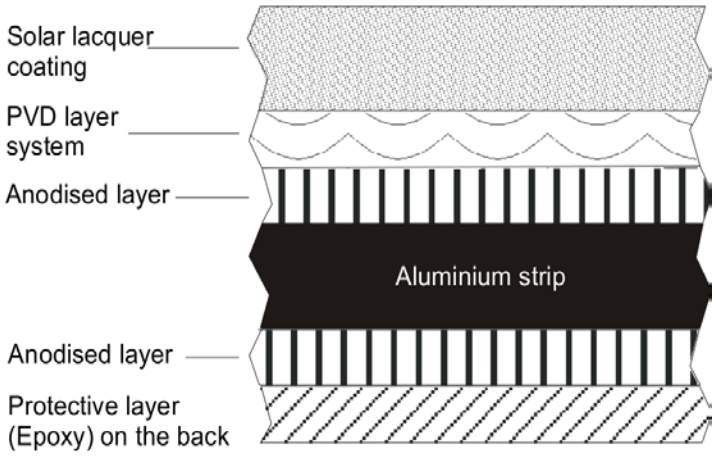



Figure 1-7: Alanod mirror films [29].

#### 1.3.1.3 Bearing structure

The bearing structure includes the mirror support, receiver support on the frame structure, pylons, and structure for mounting the pylons. The design of the parabolic trough collector differs with producers. The bearing structure of the parabolic solar trough needs to carry the mirrors with high stability to the trough and to be movable in order to make a precise sun tracking. The structure should be both stiff and lightweight. Further, it should not be deformable under its weight and withstand potential wind load which the parabolic aperture area is often exposed to. These considerations will avoid losses in optical efficiency and prevent the parabolic collector shape from any deformation. Moreover, the lightweight structure will reduce the energy demand for the collector sun tracking system [30]. In section 2.3.2, Sun tracking system will be discussed.

#### 1.3.1.4 Receiver unit

In the receiver, solar radiation is focused onto a focal line aimed at the receiver unit. The receiver heats up and in turn, imparts a significant portion of its heat to a Heat Transfer Fluid (HTF) circulating within. The hot HTF can be used to generate electricity through a steam cycle (Power block) or directly in thermochemical applications. The receiver has to follow physical and geometrical requirements in order to have high radiation absorption and low thermal losses. The reflected radiation by the parabolic collector mirror has to be absorbed as complete as possible and then converted into heat, while minimizing the thermal and optical losses.

Figure 1-8 shows the conventional type of the PTC receiver unit. It consists of an absorber pipe, which carries the heat transfer fluid inside it, encapsulated by the glass cover. An evacuated region in between minimizes conduction/convection losses [31][32]. Further, a study found that vacuum loss induced thermal losses were double that of a receiver with a good vacuum [33].

Contact between the receiver pipes with the glass sleeve is minimized to reduce conduction losses. The other receiver components are constructed with some specific considerations; the glass to metal-insulator should not experience too much stress caused by the temperature gradient, which its material has very close thermal expansion coefficient to glass. The getter is integrated into the receiver to maintain the vacuum [30]. Getters are made from a metallic compound that can absorb hydrogen and other gases that permeate into vacuum [34]. Price

H. et al. [30] showed that the permeation of hydrogen in the annulus could cause thermal losses to be almost four times that of a receiver with a good vacuum.

Every part of the receiver unit is a topic of ongoing research, such as the working fluid that can be used, as well as the optical, chemical, and thermal properties of the concerned material [12].

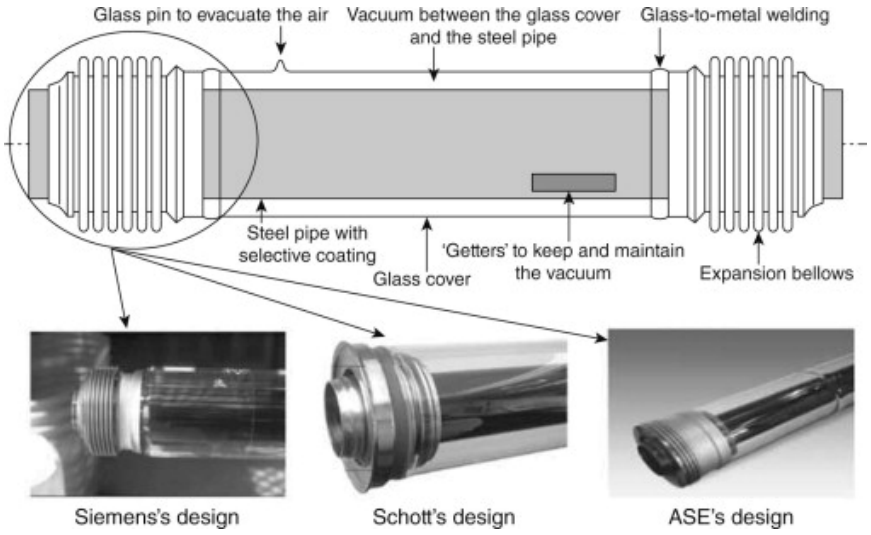



Figure 1-8: Structure of a parabolic trough receiver [35].

## 1.4 Problem statement

The prime objective of this research is to study an alternative to the existing evacuated receiver units of the Parabolic Trough Collector (PTC) that can overcome its shortcomings and compete in terms of efficiency, performance, and cost-effectiveness. Although the conventional receiver has advantages such as high efficiency and low heat loss, it has some deficiencies, such as:

- The breakage of the glass and the metal glass seal, which leads to vacuum loss in the annular region between the absorber pipe and the glass cover [36].
- The permeation of hydrogen gas into the annular region is due to the thermal decomposition of the organic heat transfer fluids (HTF) such as Therminol VP-1. The hydrogen gas in the annular region is found to increase the heat losses to four-times that in the evacuated receiver [37].
- Lower efficiency at high temperatures [2][38].
- Non-uniform thermal distribution and thermal stress problems [38][39].
- High capital outlay and high maintenance cost [40][41].

## 1.5 Objective and research justification

The maximum attainable efficiency in heat to work conversion systems is limited by the HTF outlet temperature and the Carnot efficiency [42]. In existing parabolic trough solar receivers, the selective coating is placed on the

absorber surface and is directly subjected to absorber temperatures. Consequently, the thermal degradation temperature of the coating material becomes an upper operation limit for the receiver. In this study, the possibility of raising the temperature limit, and consequently the efficiency is investigated. Specifically, the absorber pipe is encapsulated by a metallic cavity, whose inside is highly reflective in the IR region. This prevents thermal radiation from leaving the receiver. The aperture, which allows concentrated solar radiation into the cavity, is coated with a hot mirror coating, which also reflects thermal radiation back into the cavity for reabsorption by the absorber pipe. Higher operating temperatures become possible in the cavity design, since the optically active hot mirror coating is situated on the aperture window, which experiences a significantly lower temperature than the absorber pipe. Such a system with a higher efficiency will allow the HTF to achieve optimum plant temperature within a shorter length, thus reducing the needed receiver unit length as well as reducing the cost of thermal storage due to a decrease in the requirements of the storage quantity.

### 1.5.1 Specific objectives

1) To design and construct experimental rigs to validate the computational predictions for the case of applying a hot mirror coating on the glass cover of the receiver unit and for the case of a cavity receiver with a hot mirror application.

2) To construct the theoretical model with the IR reflection mechanism (a novel addition) and implement simulation code for the cavity receiver with hot mirror application, taking hot mirror and cavity mirror interactions into account.

3) To write two python codes to simulate the experimental setup in the lab (Indoor) and to simulate the receiver unit as it is in a power plant operation (outdoor).

4) Using the gathered information, we shall further explore ways of optimizing the parabolic trough receiver unit.

### 1.5.2 Some of the research questions

1) Does the simulation we developed describe the experimental data adequately?

2) How do the heat mirror and selective coating differ in terms of their optical and thermal performance?

3) How does the cavity design with the hot mirror coating on the aperture behave in terms of the efficiency of heat transfer to the working fluids?

4) What are the parameters that affect the efficiency of the system?

5) How does the cavity system behave with and without the hot mirror coating over the aperture glass cover?

6) How does the cavity design compare with the conventional receiver under different conditions?

## 1.6 Research organization

**Chapter 1:** This introductory chapter starts with a general background of this study. The objectives and main problem are stated.

**Chapter 2:** A literature review of different cavity receiver unit designs of Parabolic Trough Collector (PTC) technology is presented. Furthermore, the chapter explains the fundamental theories of solar radiation and concentrating solar radiation. Moreover, this chapter presents the main work of this study, which is a novel design of a cavity receiver unit with the application of a hot mirror coating.

**Chapter 3:** This chapter is focused on the theoretical model.

**Chapter 4:** The derivation of the reflection mechanism of the IR internal reflections inside the receiver unit is discussed.

**Chapter 5:** The description of the experiments and the adaption of the theoretical model for the receiver unit are presented.

**Chapter 6:** The chapter describes the simulation implementation that is based on the theoretical model of this study for the indoor and outdoor system as well as the simulation algorithms.

**Chapter 7:** In this chapter, the results and discussion are discussed.

**Chapter 8:** This draws the conclusions of the study and gives recommendations.

# Chapter 2 : Literature review

## 2.1 Introduction

This chapter starts by describing some concepts related to solar radiation, which is the energy source of all CSP technologies. Previous work done on cavity type receiver is discussed, and finally earlier work related to the current project is presented.

In order to understand the characteristics of the energy source for CSP systems, it is essential to understand thermal and solar radiation. There are some concepts of radiation that require conceptual clarification: a) Radiation is the energy emitted by an object in the form of electromagnetic waves/photons as a results of changes in the electronic configurations of atoms/molecules [43], b) Radiant energy, in Joule [J], is the energy of electromagnetic waves, c) Radiant power, in Watt [W] or [J/s], is the radiant energy per unit time, d) Irradiation, in [J/m$^2$], is the incident radiant energy per unit area, e) Irradiance, in [W/m$^2$] or [J/s.m$^2$], is the incident radiant power per unit area, f) Radiant emittance, in [W/m$^2$] or [J/s.m$^2$], is the emerging radiant power per unit area of a surface.

## 2.2 Thermal radiation

Thermal radiation is the radiation that is continuously emitted over a wide range of wavelengths in all directions by any object which has a temperature above absolute zero. It is a portion of the electromagnetic spectrum, which extends from 0.1 to 100 $\mu$m [43]. Consequently, the thermal radiation includes the entire range of infrared and visible wavelength as well as a portion of ultraviolet radiation. Solar radiation is the electromagnetic radiation emitted by the sun, falling into the wavelength range from 0.3 to 3 $\mu$m. Different objects at the same temperature may emit different amounts of energy per unit surface area because the energy emission at a particular wavelength depends on the material and surface conditions [1]. The definition of an idealized body, which is a perfect emitter and absorber of radiation is required to be served as a standard against the real bodies in terms of radiation properties. This idealized body is called a blackbody. The total radiation emitted by a blackbody per unit time per unit surface area is determined by the Stefan-Boltzmann law as $B(T) = \sigma T^4$, where $\sigma = 5.67 \times 10^{-8}$ W/m$^2$.K$^4$ is the Stefan Boltzmann constant and, *T* is the surface temperature in Kelvin. Determining the amount of radiation in a certain wavelength leads to the introduction of the spectral blackbody emissive power definition, which is the radiation energy emitted by a blackbody at absolute temperature *T* per unit time, per unit surface area and per unit wavelength about the wavelength $\lambda$. It is defined by Planck's law as:

$$B_\lambda(\lambda, T) = \frac{2\pi hc^2}{\lambda^5\left(e^{hc/\lambda kT}-1\right)}, \tag{2.1}$$

where $k = 1.38065 \times 10^{-23}$ J/K is the Boltzmann's constant, $h = 6.62607 \times 10^{-34}$ J.s is the Planck's constant, and $c = 2.998 \times 10^8$ m/s is the speed of light in vacuum. The relation in Eq. (2.1) is valid for an object in a vacuum or a gas. For other mediums, the speed of light in vacuum *c* needs to be modified by replacing *c* to *c/n*, which represents the speed of light in a medium with a refraction index *n.* The spectral blackbody emission power, $B_\lambda$, with wavelength for different temperature is shown in Figure 2-1. As the temperature increases, the curves with their peaks shifts toward the shorter wavelength regions. As a result, at a higher temperature, a

significant fraction of the blackbody radiation is emitted at shorter wavelengths. At a specified temperature, the wavelength at which the maximum intensity of the emitted radiation occurs is shown with dotted lines in Figure 2-1. The maximum $\lambda_{max}$ as a function of temperature in Kelvin is given by Wien's displacement law as

$$\lambda_{max} = \frac{2.8978 \times 10^{-3}}{T}. \quad (2.2)$$

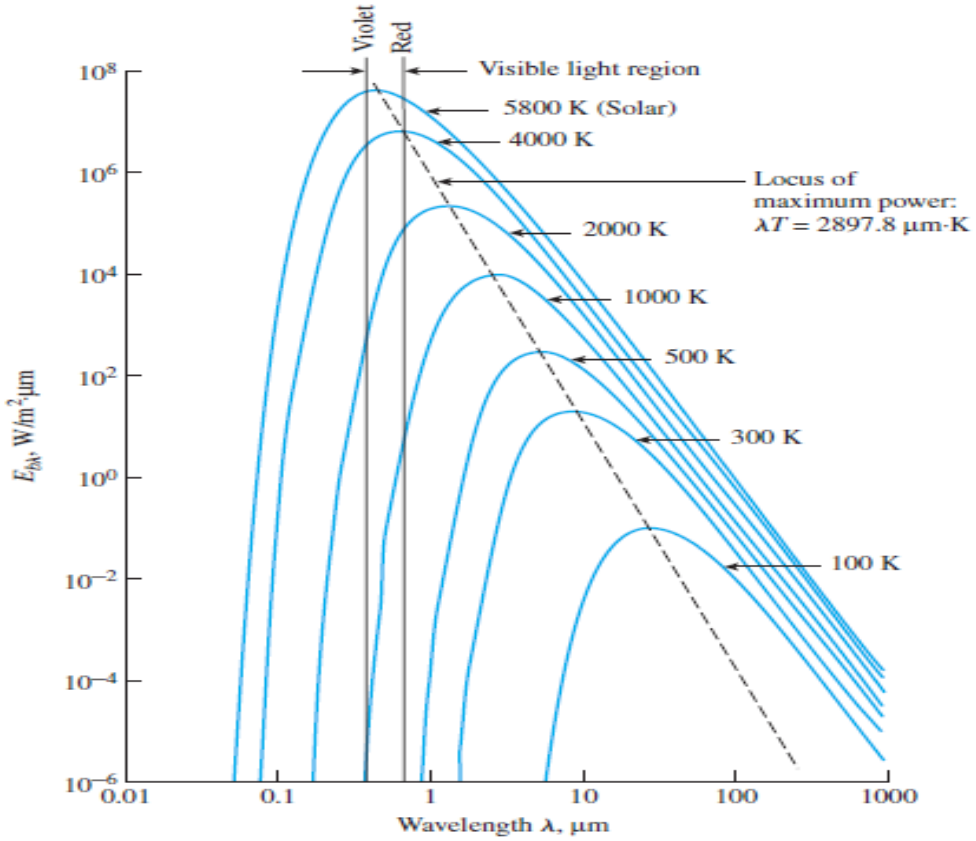



Figure 2-1: Spectral blackbody emission power at different temperatures [43].

## 2.3 Solar radiation

The electromagnetic radiation of the sun resembles, in its spectrum, the thermal radiation of a blackbody at around 5780 K, see Figure 2-2. It reaches its peak in the visible range, where the wavelength is at about 0.5 $\mu$m, using Eq. (2.2), of the spectrum.

The direct energy source for the Parabolic Trough Collector (PTC) operation is the solar irradiance at the Earth's surface. The solar irradiance outside the terrestrial atmosphere (solar constant) is used to estimate the solar irradiance on the Earth's surface. By approximating the sun as a blackbody with a surface temperature $T_S = 5780$ K and the sun radius $r_S \sim 6.965 \times 10^8$ m, the power that is emitted by the sun into space can be calculated using Stefan-Boltzmann law, where $P_{Sun} = 4\pi r_S \, \sigma \, T_S^4 = 3.85 \times 10^{26}$ W. The solar irradiance of the outer border of the Earth's atmosphere, which is called solar constant $G_S$ is then determined by calculating the irradiation at the sphere with a radius $r_{SE} \sim 1.496 \times 10^{11}$ m (the mean Sun-Earth distance) on which the Earth' orbit is located. Consequently, the solar constant is obtained by dividing the total radiant emittance of the sun $P_{Sun}$ by the area of

a sphere with radius $r_{SE}$, where $G_S = P_{Sun}/4\pi r_{SE} \sim 1367$ W/m$^2$. The World Meteorological Organization concurs with this value as a result of different measurements [44]. The irradiance at the Earth's surface is much smaller because it undergoes significant attenuation as the solar radiation passes through the atmosphere due to absorption, reflection, and scattering, see Figure 2-2. Consequently, the irradiance at the Earth's surface is reduced to about 950 W/m$^2$ in a clear day with a range of wavelength from 0.3 to 2.5 $\mu$m [43]. Scattering of the solar radiation through the atmospheres' components causes part of the radiation to be diffused rather than direct radiation. The diffuse solar radiation is assumed to be uniform from all direction, but direct radiation reaches the Earth's surface in straight lines. In CSP technologies, direct radiation is used rather than diffuse because the latter cannot be concentrated [45].

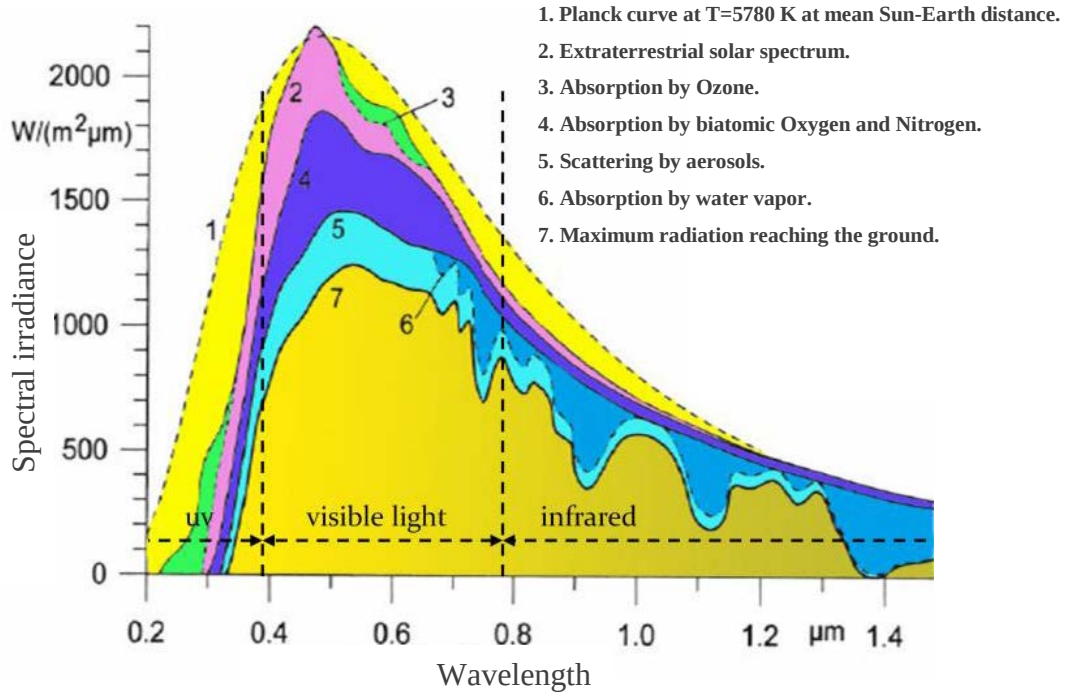



Figure 2-2: The solar spectrum and its atmospheric influence [46].

### 2.3.1 Sun Geometry

To localize the sun with respect to a terrestrial observer or a geometric plane, the position of the plane on the earth, the sun-earth geometry and time are required [45][47]. The position of the Sun is determined by using two angles in relation to the earth. The common coordinate systems that will be used to map a celestial object in relation to earth are the equatorial and horizontal coordinate systems. In the equatorial coordinate system, the fundamental plane passes through the terrestrial equator. The declination angle $\delta$ and the hour angle $\omega$ are used in this coordinate system. The declination angle is the angle between the line to the Sun and the equatorial plane. It is a function of time, and its value oscillates with a period of one year between $23.45^\circ$ and $-23.45^\circ$ due to the inclination of the earth axis to the orbit by $23.45^\circ$. The declination can be written as a function of the day of the year (*DOY*) as [48][49]

$$\delta = 23.45^{\circ} \sin\left(360 \times \frac{284+DOY}{365}\right). \quad (2.3)$$

$\delta$ is positive during summer and spring of the northern hemisphere and negative in the southern hemisphere. The hour angle $\omega$ is the angular displacement of the sun east or west of the local meridian due to the rotation of the earth around its axis at $15^{\circ}$ per hour. It is defined in terms of Solar Time (ST) in hours as

$$\omega = 15 \times (ST - 12), \quad (2.4)$$

where $\omega = 0^{\circ}$ at 12:00h of solar time. It is positive in the morning and negative in the afternoon. It must be converted from clock time or Local Standard Time (LST) to ST to get $\omega$

$$ST = LST + 4 \times (L_{st} - L_{loc}) + A, \quad (2.5)$$

where $A = 9.87 \sin 2B - 7.35 \cos B - 1.5 \sin B$ and $B = \frac{360}{365}(DOY - 1)$. This conversion as it was seen in Eq. (2.5) requires the location's longitude $L_{loc}$and local standard meridian $L_{st}$, which is the time zone reference longitude at which the clock time or LST is based [45][47]. In the horizontal coordinate system, the fundamental plane is the observer's horizontal plane. The solar altitude angle $\alpha_s$ and the solar azimuth angle $\gamma_s$ are used. The solar altitude angle $\alpha_s$ is the angle between the horizontal plane and the line to the sun, while the solar azimuth angle $\gamma_s$ is the angular displacement from the south projection of the beam radiation on the horizontal plane. The displacement to the West is positive, and the East is negative.

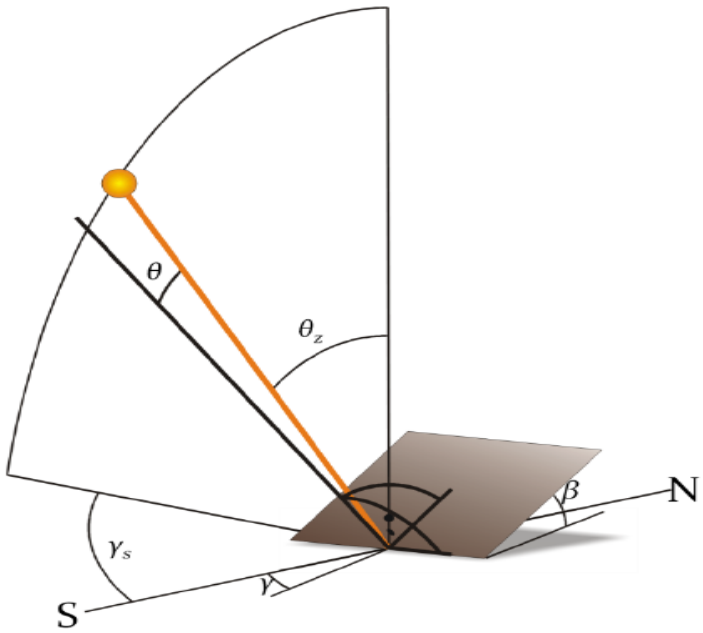



Figure 2-3: A plane with a tilt angle $\beta$, surface azimuth angle $\gamma$, incidence angle $\theta$, solar zenith angle $\theta_z$and solar azimuth angle $\gamma_s$ [45].

Other angles in Figure 2-3 are used to define the sun's position relative to a tilted plane on the Earth's surface. These angles are as follows: 1) Tilt angle $\beta$ is the angle between the plane of the surface and the horizontal, 2)

Zenith angle $\theta_z$ is the angle between the vertical and the line to the sun (the complement of solar altitude angle $\alpha_s$), 3) Surface azimuth angle $\gamma$ is the angle from the deviation of the projection on a horizontal of the normal to the surface from the local meridian where $\gamma = 0^\circ$ at south and $\gamma = 90^\circ$ at West, positive to West and negative to East ($-180^\circ \leq \gamma \leq 180^\circ$), 4) Angle of incident $\theta$ is the angle between the beam radiation on a surface and the normal to that surface [18].

### 2.3.2 Sun Tracking System

To obtain a continuous concentration of the direct solar radiation using a parabolic trough, the sun has to be continuously tracked. In CSP, there are two different concentration types of systems: Point-Focusing and Line Focusing systems. In Point–Focusing systems, such as Solar Dish and Solar Power Tower, a two-axis tracking system is required. In Line-Focusing systems, such as PTCs and Linear Fresnel Reflectors, a one-axis tracking system is sufficient, see Figure 2-4. The tracking system in PTC can be East-West aligned, where the sun is tracked from north to south, or a North-South alignment, where the sun is tracked from West to East, see Figure 2-5. The North-South alignment is more common due to the higher annual energy yields, and higher average daily collector performance [45]. In the tracking mechanism, the parabolic mirror orientation can be described by the surface azimuth angle $\gamma$ and the collector zenith angle *S*, which is the angle between the line of the zenith and the optical plane, see Figure 2-5. Therefore, the angle *S* is the tracking angle, which is calculated as

$$\tan S = \tan \theta_Z \, |\cos(\gamma - \gamma_S)|, \tag{2.6}$$

where $\gamma_S$ and $\theta_Z$ are the solar azimuth and zenith angles, respectively. The parabolic aperture in the morning is oriented to the east and in the afternoon to the west so that $\gamma = -90^\circ$ when $\gamma_S < 0^\circ$ and $\gamma = 90^\circ$ when $\gamma_S > 0^\circ$.

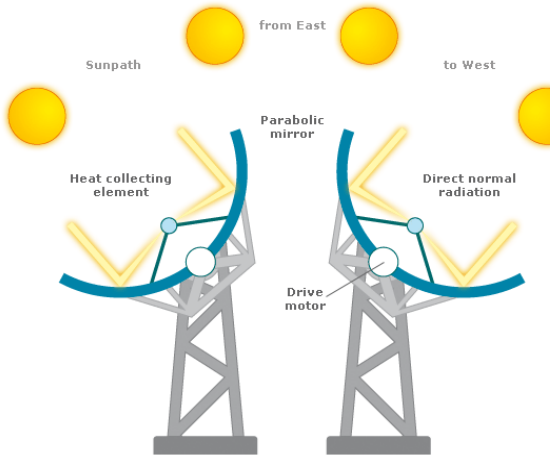



Figure 2-4: Single-axis tracking mechanism of PTC [50].

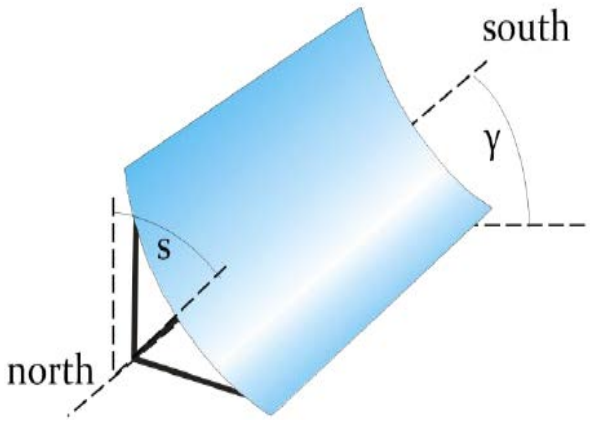



Figure 2-5: PTC tracking angles with North-South alignment [45].

The incident angle of solar beams $\theta$ on PTC with one-axis tracking depends on the Sun position and the collector alignment. In the common alignment, which is North-South alignment, $\theta$ is defined as [45]

$$\cos\theta = \sqrt{\cos^2\theta_z + \cos^2\delta \times \sin^2\omega}. \tag{2.7}$$

In the case of the East-West alignment, $\theta$ is defined as

$$\cos\theta = \sqrt{1 - \cos^2\delta \times \sin^2\omega}. \tag{2.8}$$

Alternatively, full tracking with two axes of rotation for PTC is possible. It ensures that $\theta$ is always about $0^{\circ}$, but implementing two axes is costly [51].

## 2.4 The Parabolic Trough Collector

As mention in Chapter 1, the Parabolic Trough Collector (PTC) is the most common and mature technology among concentrated solar technologies used in solar electricity generation and thermochemical applications. The receiver unit see Figure 1-8, is one of the most complex parts, and the efficiency of the whole system largely depends on it. It has to be carefully designed in such a way as to minimize energy losses. Every part of the receiver unit is a topic of ongoing research, such as the working fluid that can be used, and the optical, chemical, and thermal properties of the concerned material [52]. In the following section, some of the conventional receiver problems and their solutions are discussed, especially the heat losses and thermal performance problems that appear when the Heat Transfer Fluid (HTF) temperature increases.

### 2.4.1 Some of the conventional receiver unit problems and their solutions

Increasing the outlet HTF temperature is one of the main challenges to improve the overall efficiency of the PTC power plant and to reduce the Levelized Cost of energy and the combined thermal storage. For example, thermal storage quantity can be reduced to one third, if the HTF temperature increases from 350 °C to 600 °C [37]. The dominant heat losses mechanism at high temperatures is the thermal emission (IR) from the receiver pipe. This loss is conventionally minimized by painting the receiver pipe with a spectrally selective coating, which absorbs well in the visible region of the solar spectrum and emits poorly in the IR region. Much work has been published on selective coatings and improving their properties [53]. Dudley et al. [32] investigated the performance of black chrome and cermet selective coatings, and found that the Cermet had lower emissivity values and thus reduced thermal losses and improved efficiency. Forristal [54] compared six different selective coating materials to evaluate receiver unit performance. He showed that the receiver performance is susceptible to the optical properties of the selective coatings and improving the coatings could result in significant efficiency gain. Cheryl et al.[55] Investigated spectrally selective coating materials for CSP applications, and concluded that the ideal selective coating material should be easy to manufacture, low-cost, chemically and thermally stable in air at operating temperature of 500 °C. Because the selective coatings are placed on absorber pipe of the receiver, the receiver operation temperature is limited and hence thermal efficiency. Kennedy et al. [56] were able to successfully model a solar-selective coating composed of materials stable to 500 °C using computer-aided design software. Archimede Solar Energy (ASE) [57] manufactured the world's most advanced solar receiver tube with selective coating. It operates at temperature up to 580 °C with molten salts as HTF.

Further, the solar receiver SCHOTT PTR 70 is designed for solar thermal power plants operating with oil-based HTF at a temperature up to 400 °C [58], where most of the power plant used oil-based fluids. The heat loss measurements for SCHOTT PTR 70 were carried out in a round-robin test performed by SCHOTT Solar CSP in

cooperation with Deutsches Zentrum für Luft-und Raumfahrt (DLR) and US National Renewable Energy Laboratory (NREL). The tests confirmed that the heat loss is less than 250 W/m at working temperature 400 °C [58].

A hot mirror coating application on the glass cover inner surface helps by reflecting IR radiation, thereby cooling the glass cover surface [59] and possibly reducing thermal stresses there. It is alternative to the selective coating, where the coating is on the absorber pipe instead of the glass cover inner surface. It is a dielectric material that is transparent to the visible region of the solar spectrum and reflects well in the IR region. Hot mirror coating was first implemented for energy-efficient windows in automobiles and buildings [60] as well as for applications related to concentrating photovoltaics and thermophotovoltaics [61][62]. There are two general types of hot mirror films: a semiconducting oxide with a high doping level and a very thin metal film sandwiched between two dielectric layers (see [63][64][60] for more details). The thin metal film coating shows some unavoidable losses. Besides, the highly doped semiconducting oxide shows more advantages, i.e., Indium-Tin-Oxide (ITO). The hot mirror coating for a solar collector must meet some performance specifications. It needs to be highly transparent in the visible region and have high reflectivity in the IR region of the solar spectrum. Granqvist et al. [60] and Lampert et al. [63] focused on improving the transparency in the visible region and the reflectivity in the IR [63]. In section 2.5.1, more details about the hot mirror coating will be discussed.

Some complications start to appear at a high temperature (> 300 °C) and with a non-uniform solar flux distribution such as the thermal performance and thermal stress of the receiver unit. When a non-uniform heat flux profile is incident on the receiver unit, the temperature across the circumference varies, and peaks/hot spots in the receiver start to increase with temperature. It leads to bending of the absorber pipe and breaking of the glass cover. P Wang et al. [39] found that the maximum temperature gradient for the safe operation of receiver tubes is about 50 K. These complications have been addressed to increase the life span of the receive absorber. Some recent research focused on improving both thermal transfer and uniformity of the thermal distribution [38], but sacrifice pressure drop of the receiver unit or increase the quality of the absorber pipe and other components, adding cost [2].
Some of these studies suggest applying inserts into the absorber pipe such as metal foam, porous discs, perforated plates or coiled wire turbulators inserts. A metal foam inserted into the absorber pipe facing the concentrates sunlight reduces the thermal stress, decreases the temperature difference on the outer surface of the absorber pipe by about 45%, but increases flow resistance [39]. Experimental [65] and theoretical work [66] was conducted for the porous disc insert application (a disc perforated with holes inserted into the pipe), increasing the thermal efficiency between 1.2% and 8% according to the numerical study [67]. The coiled wire turbulators insert application has been examined experimentally and numerically [68]. At the pitch distance 30 mm of coiled wire turbulator (a coil-shaped wire inserted into the absorber pipe), the heat transfer enhancement is approximately twice that of the smooth tube [68].
Other studies focus on geometrical structure improvement for the absorber pipe of the receiver unit such as a dimpled tube, unilateral milt-longitudinal vortex-enhanced tube as well as symmetric and asymmetric outward convex corrugated tubes. These inserts manipulate the Reynolds number, substantially improving the "mixing" of different temperature layers of fluid. A numerical study showed improved performance of a dimpled absorber pipe under non-uniform heat flux over uniform heat flux [69]. Similar improvements were found for the unilateral

milt-longitudinal vortex-enhanced tube, with better heat transfer performance than the smooth pipe under a wide range of working conditions [70]. The introduction of symmetric [71] and asymmetric [72] outward convex corrugated tubes, regular outwards “bulges” in the absorber pipe, effectively decrease the thermal strain and enhance the heat transfer performance.

Further, researchers have investigated nanofluids (with suspended nanoparticles) to enhance the heat transfer. The most used nanofluids contain nanoparticles such as Al, $Fe_2O_3$, $Al_2O_3$, Cu, $TiO_2$, and $SiO_2$ [73] [74]. Nanofluids tend to have more significant thermal conductivity than normal heat transfer fluids. The thermal conductivity increases by decreasing the particle size and increasing the volume fraction and temperature[74]. E. Bellos found that the use of the nanofluids increases the efficiency of the collector by 4.25% [73].

Some of the limitations associated with evacuated receivers have been overcome. Nevertheless, the monopoly over this technology and the cost of the receivers hinder solar projects, especially in the developing countries [75]. Accordingly, finding alternatives to the evacuated receivers that can compete in terms of efficiency and cost-effectiveness is the prime target. Such alternatives are expected to have a significant impact on the already long-standing industry. An alternative to the evacuated receiver is the cavity receiver, which could make up those shortages of the evacuated receiver. The alternative uses the idea of the cavity receiver, which originates from the concept of the blackbody object “cavity”. In the following sections, a review of different cavity receiver designs is discussed next.

### 2.4.2 Cavity receiver overview

The concept of the cavity receiver comes from the blackbody principle. The blackbody is an ideal object, absorbs all incident radiation, regardless of direction and wavelength [43]. The object that most closely resembles a blackbody is a large cavity with a small opening. The radiation that is incident through the opening has very little chance to escape, it is either absorbed or undergoes multiple reflections before being absorbed [43].

The following review is intended for the receiver of a parabolic trough collector, but some designs are suitable for the receiver of the linear Fresnel reflector systems. The review discusses cylindrical and non-cylindrical receiver unit designs separately.

#### 2.4.2.1 Cylindrical receivers

The base design of the cavity receiver consists of a cylindrical metal tube with a cavity opening for the incident solar radiation. In most of the normal cavity receivers that have been studied, the space inside the cavity was at atmospheric pressure. The inner cavity surface opposite to the aperture window was mirrored. The aperture window of the cavity was at the bottom, facing the parabolic mirror collector and it was closed by a transparent cover to reduce convection and re-radiation heat loss. Moreover, the outer cavity surface was thermally insulated to minimize the effect of heat loss by convection and radiation to surroundings.

#### A. Mirrored glass cover with uncoated aperture

Ramchandra et al. [37] studied and optimized the cavity receiver shown in Figure 2-6 for minimum heat loss. The study intended to evaluate and compare different PTC cavity receiver alternatives using a validated numerical

model. Their cavity receiver, shown in Figure 2-6, consists of a mirrored cavity surface facing the absorber pipe. The cavity aperture is closed by a transparent glass cover to reduce re-radiation and convection heat losses. The annulus between them is separated by an air gap at atmospheric pressure. An annular ring of microtherm between the absorber and glass envelope at both ends is placed to suspend the absorber [37].

The dimension of the cavity aperture was carefully selected alongside with the focal line of the collector to ensure that all reflected radiation enters the cavity through the aperture and to minimize inaccuracies in both tracking and directional errors due to the suns shape. The optimum annulus dimension between the absorber pipe and the cavity envelope was selected to reduce convection and conduction heat loss. The optimum dimension of the annulus largely depended on the diameter of the receiver components [76].

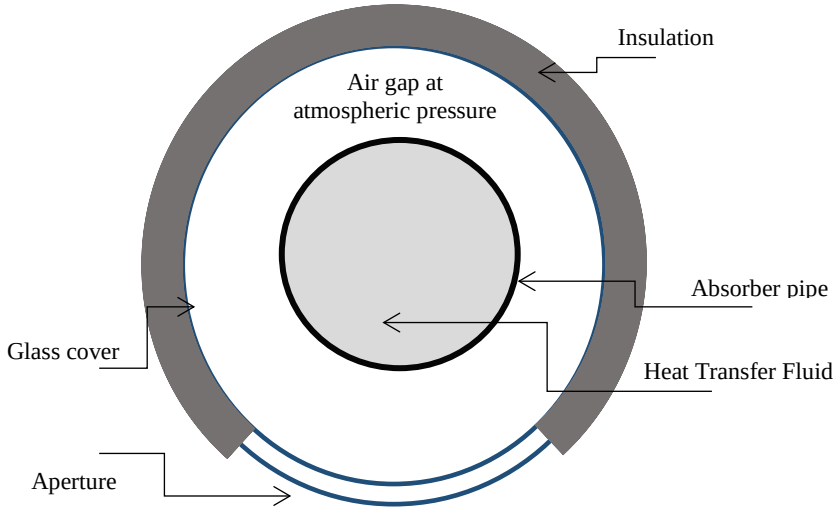



Figure 2-6: Schematic representation of the linear cavity receiver [37].

Although this cavity receiver was capable of being a suitable alternative to the conventional receiver with a parabolic trough that has a smaller rim angle around 45°, it had some limitations. First, the intercept factor (the incident energy that enters the aperture and reaches the absorber) was lower than that of a conventional receiver. This problem was addressed by coupling this cavity design with a lower rim angle (around 45°) for the parabolic trough. The conventional receiver had a maximum concentration at rim angle = 90°, whereas the concentration ratio for this design was maximum at rim angle = 45° [37]. Second, the selective coating failed because the air in the annular gap oxidized the coating. The oxidation of the selective coating in the presence of the air in the annulus was expected to be resolved with the progress in developing selective coatings [77]. Third, at a higher temperature, the thermal conductivity of the insulation material increased, thus the heat loss also increased [76]. This issue was solved by selecting a better-suited insulation material.

### B. Cavity receiver with asymmetric compound parabolic concentrator

Roman Bader et al. [78] has proposed a cavity receiver, presented in Figure 2-7, with the aim to significantly cut the costs per unit PTC through a decrease in the PTC size and use of low-cost materials as well as using the air as the heat transfer fluid. The cavity design consists of an absorber tube enclosed by an insulated stainless steel cylindrical cavity with an asymmetric compound parabolic concentrator (CPC) at the cavity aperture, shown in

Figure 2-7. This design was tested with a 43 m long prototype installed and a 9 m aperture solar trough concentrator to study the efficiency of receiver under different operating conditions and validate the heat transfer model of the receiver that based on Monte Carlo ray-tracing and finite-volume methods [78].

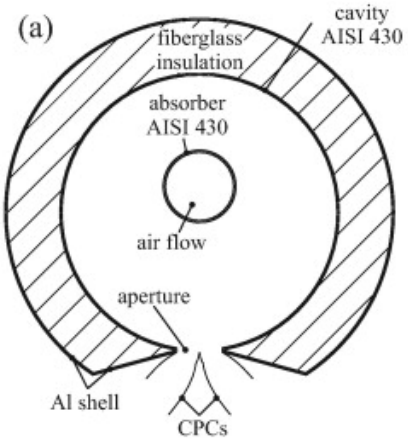



Figure 2-7: Schematic representation of the cavity receiver design proposed by[78]

At HTF inlet temperature of 120 °C, HTF outlet temperature was expected in the range of 250-450 °C, at summer solstice solar noon (input of 280 kW), while the efficiency of the receiver ranged from 45% to 29%. The optical losses were one-third of the total incident radiation on the receiver, due to the spillage at the aperture and reflection inside the cavity. The thermal losses due to the natural convection from the cavity insulator were 5.6 - 9.1%. Another heat loss was due to the re-radiation through the cavity aperture (6.1 - 17.6%). Moreover, HTF pumping work had an associated energy penalty of 0.6 – 24.4% of the total power generated [79].

The authors suggested a modified cavity receiver design that evolved from the initial design, which is discussed next.

### C. Corrugated cavity receiver

Roman Bader et al. [78] suggested modifications to their previous cavity design. The modified design is shown in Figure 2-8. It consisted of a cylindrical cavity with a smooth or corrugated black inner surface with a single- or double-glazed aperture window. The modification can be summarized as follows:

The absorber pipe was eliminated to allow the HTF (air) to flow in a sufficiently large cross-section through the cavity to compensate for the lower volumetric heat capacity. The cavity from the inside (surface 1, Figure 2-8) was enhanced with V-corrugations to increase the heat transfer surface area. The cavity aperture was made from glass to reduce the convective heat loss at the aperture, where the glass is almost opaque for the radiation emitted from a blackbody at < 600 °C [78]. The two window panes of a double-glazed window with air in between were used to trap the emitted radiation of surface 1 and the inner window to reduce the heat conduction through the window.

The authors studied this design with four different receiver configurations: smooth, V-corrugated absorber tube, single, and double-glazed aperture window.

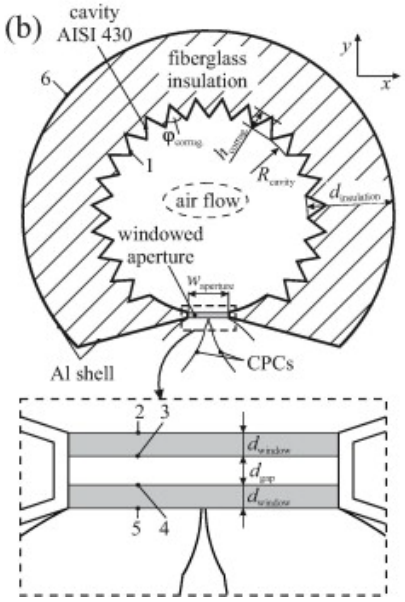



Figure 2-8: The modified design [42].

Using the air as a HTF in this design is to avoid the chemical instability during the operation and to allow the direct coupling of the solar collector with a packed bed thermal storage [80][81]. However, the air has a lower volumetric heat capacity, which leads to lower convective heat transfer compared to conventional HTFs, such as molten salt and thermal oils. This problem could be solved by designing a receiver with a larger diameter and higher heat transfer area than that of the conventional receiver [82]. In the modified design, V- corrugations were used to increase the heat transfer of the surface area.

The simulation was validated with the experimental work for the design in Figure 2-7, and then used to analyze the modified design. The modified design Figure 2-8 was simulated during the summer solstice at solar noon in Sevilla, Spain, with direct normal solar irradiance equals 847W/m$^2$. It had a collector efficiencies between 60% and 65% at HTF temperature of 125 °C and between 37% and 43% at 500 °C. The largest source of energy loss was the optical loss, which was more than 30% of the incident solar radiation. It was mainly because of the absorption by the concentrators and reflection at the receiver's aperture window [78]. Moreover, the required pumping power for the HTF through a 200 m long receiver operated between 300 °C and 500 °C was between 11 and 17 kW.

Furthermore, increasing the HTF mass flow rate would cause a decrease in heat loss with the corrugated absorber pipe, which led to an increase in receiver efficiency. At the expense of additional reflection loss, the double-glazed aperture window significantly reduced the re-radiation loss from the receiver's aperture compared to the single-glazed window, where the double-glazed acted as an effective radiation trap. However, the single-glazed receiver led to higher collector efficiencies at low HTF temperature (< 300 °C), the double-glazed receiver led to higher collector efficiency at high HTF temperatures. The author suggested using a material with a high reflectivity on the aperture window to improve the overall efficiency of the PTC [78].

### D. Cavity receiver with copper pipes and copper annulus

Barra et al. [83] proposed a different design of the cavity receiver shown in Figure 2-9. The motivation of their study was to design a blackbody cavity receiver more efficient and less expensive than the conventional receiver

units. The structure of that cavity receiver was made from iron and copper pipes, which were selected for economic and stability reasons. The iron oxidation was to induce high visible absorption in the cavity. The V-shape Pyrex glass in the cavity opening was removable and selected for low-cost commercial availability and to reduce the convection loss. This design was tested with 50 $m^2$ parabolic trough prototype, and the experiment parameters and results used to build a mathematical model to simulate the system. The working conditions of this cavity receiver were not optimum, but the performance of that design appeared promising compared to those obtained from a more expensive receiver. The study showed less solar interception with the cavity and more thermal losses, which were strongly depending on wind intensity and direction. Furthermore, the cavity receiver without a vacuum and selective treatments reached a good performance, but still inferior to the current receivers with highly selective coating and vacuum. The author suggested that the cavity receiver needed a design improvement and proposed the substitution of copper pipes with a copper annulus, as shown in Figure 2-10. This design was first proposed by Boyd et al. [84] to achieve better performance without requiring advanced materials and coating. The inside of the annular tube was coated with black paint. The entrance aperture with the insulation on the wall side was cut in V- shape to limit the thermal radiation loss from the collector aperture. It was assumed to have a diffuse surface to reduce the effect of radiative field view of the aperture to the surrounding [84]. In addition, the natural convection loss could be restricted by adjusting the entrance angle of the aperture because the narrow passage causes flow restrictions [84]. The receiver efficiency has been calculated for the hot end of the receiver, where it is lowest, and also averaged over the length of the collector, as a measure of overall performance [84]. The hot end efficiency was 53%, and the average was estimated to be 76% at 370 °C. Furthermore, the conduction through the insulator was dominant at a lower temperature (at 130 °C) and radiation loss was dominant at a higher temperature (at 370 °C).

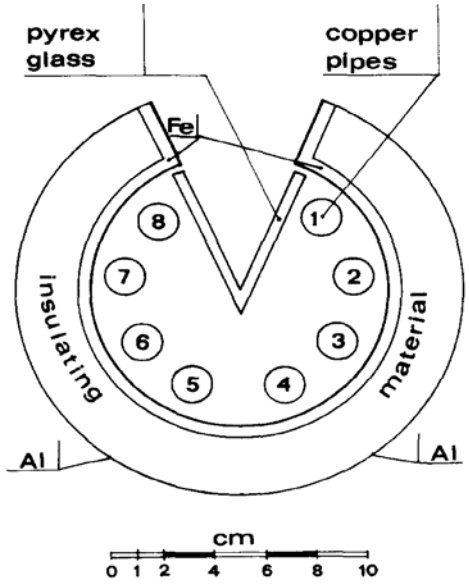



Figure 2-9: Vertical cross-section of the cavity receiver [83]

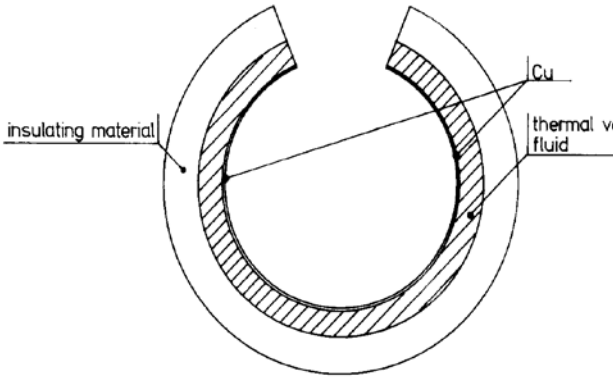



Figure 2-10: Vertical cross-section of the suggested optimized cavity receiver[83].

### E. The arc-shaped cavity receiver

Xueling Li et al. [85] studied an arc-shaped linear cavity receiver, where the absorber has a crescent shaped channel, as seen in Figure 2-11, with the aims to raise the HTF temperature and reducing the cost of production and maintenance as well as having a similar shape and size to the conventional receiver [85]. The crescent shaped

channel was made from a copper and the outer surface of the channel covered with opaque insulation. The cavity aperture window was fabricated from borosilicate glass, see Figure 2-11.

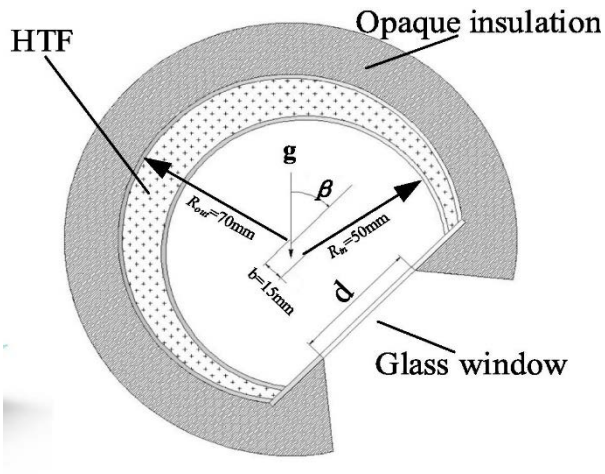



Figure 2-11: Arc-shaped linear cavity receiver with a lunate channel [85].

The thermal performance of this design was studied theoretically using a numerical model [85]. The effects of the HTF temperature, surface emissivity, inclination angle, and aperture width were analyzed and displayed some of the following characteristics: the total heat loss of the receiver decreased from 394.5 W/m to 335.8 W/m, when the inclination angles increased from 0° to 90°. The heat loss of the receiver increased with the aperture width of the cavity at the same collecting temperature. A reasonable aperture width of this cavity design is about 50 - 70 mm, where the dimensions of the cavity are shown in Figure 2-11. Generally, at a larger aperture width, the heat loss increased, and the optical loss (which could be from installation and tracking errors, mirror roughness and manufacturing error) decreased. At a high temperature ( > 400 K), a comparison between the proposed design and an evacuated receiver (Solel's UVAC) showed that the heat loss of the proposed design was less and slower than that of the evacuated receiver [85].

#### 2.4.2.2 Non-cylindrical receiver unit geometries

### A. Elliptical cavity receiver

Fei Cao et al. [86] studied the elliptical cavity receiver, as shown in Figure 2-12, with the aim of having a receiver with high thermal performance, low cost, and not frangible. The outer cover was elliptic with an open inlet towards the parabolic trough mirror. The incoming concentrated solar radiation was incident on the receiver and entered into the absorber pipe through the opening.

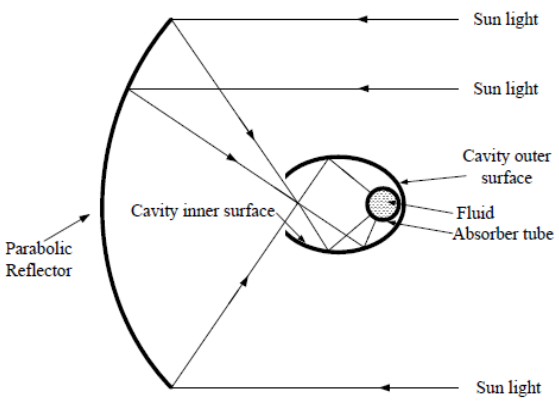



Figure 2-12: Elliptical cavity receiver [86].

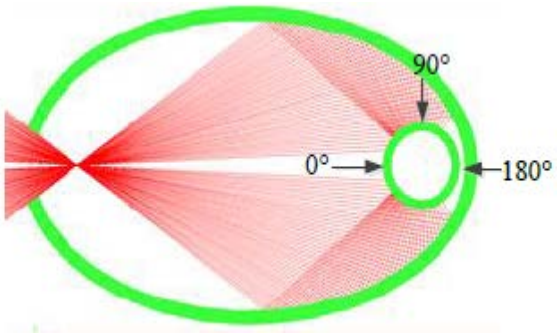



Figure 2-13: Heat and light flux distributions around the receiver cavity [86].

The position of the absorber pipe was on the opposite focus from the opening. The design was studied using a ray-tracing model and a heat transfer model. The study focused on analyzing the heat transfer and the heat flux distribution in a 1m cavity receiver tube as well as the thermal stress distributions of the absorber pipe. The geometry of the design and its dimension were mentioned in [86]. The light and heat flux distribution around the absorber pipe outer surface is summarized in Figure 2-13. There was no light and heat flux from $0^{\circ}$ to $10^{\circ}$ and from $125^{\circ}$ to $215^{\circ}$, see Figure 2-13 . Most of the other light entered the cavity and reflected from the elliptic inner surface to the absorber surface. This led to a non-uniform heat flux absorption along the circumference of the absorber tube. The thermal stress was found to cause a maximum deformation of the receiver tube along the fluid direction of 3.1 mm at 0.82 m. The thermal stress was generated by the temperature difference between the tube inner/outer wall and the heat transfer fluid pressure and phase. This, in turn was caused by the fluid and steel characteristic, solar heating flux and the characteristics of the heat transfer fluid and the absorber material. Besides that, equivalent stress along the absorber pipe was found at higher fluid mass flow rates.

### B. Elliptical cavity receiver with optical funnel

Fei Cao et al. [87] proposed a modified design that evolved from their initial design in Figure 2-12 to improve the performance of the elliptical cavity. The authors modified the design by adding a flat plate reflector at the cavity aperture, see Figure 2-14, to diminish the effect of changing the PTC focal length on the cavity opening length and the effect of tracking error angle on the cavity performance.

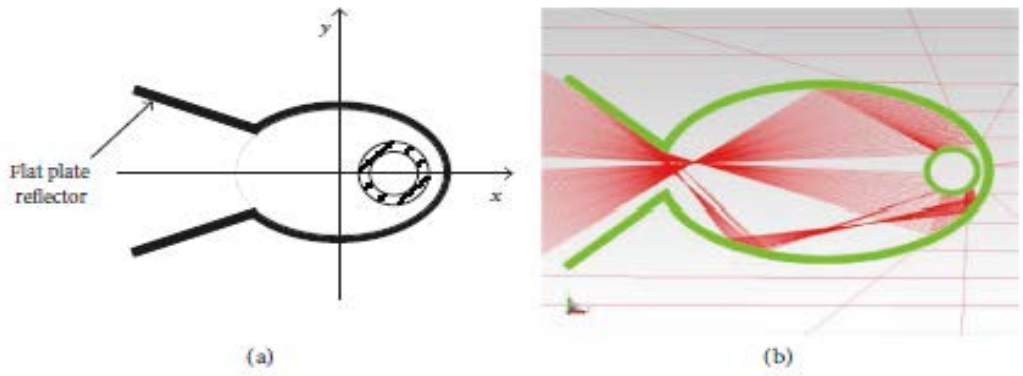



Figure 2-14: Elliptical cavity with flat plate reflector [87] a) Structure schematic b) light distribution around the receiver.

Figure 2-15 shows the effects of different tracking error angles and PTC focal distances on the cavity darkness of the modified cavity receiver. Cavity darkness is the percentage of the sunlight on the absorber surface to the total incident sunlight. It was found that introducing the flat plate reflector can significantly increases the cavity darkness, where the flat plate breaks the monotonic relationship of the cavity darkness under different focal distances. Further, at different tracking error angles the incident sun radiation is reflected by the flat plate, which causes different multi-reflections inside the cavity, which leads to the curves in Figure 2-15 [87].

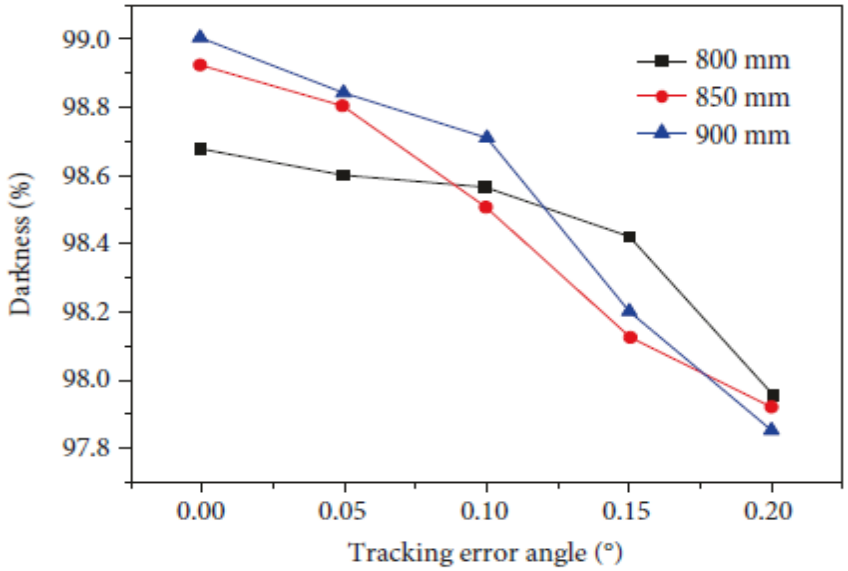



Figure 2-15: Darkness of the modified elliptical cavity receiver under different tracking angle and PTC focal distances [87].

### C. Triangular and V cavity receivers

F Chen et al. [88] studied the triangle cavity receiver experimentally and theoretically with the aims to provide high efficiency and make up the shortages of the conventional receivers such as high cost, leakage during long-term running, and challenging technology. The cavity was made from aluminum, and the absorber surface was a triangle or V-shape structure with fins in the dorsal side to enhance the thermal performance between the absorber surface and the HTF, see Figure 2-16.

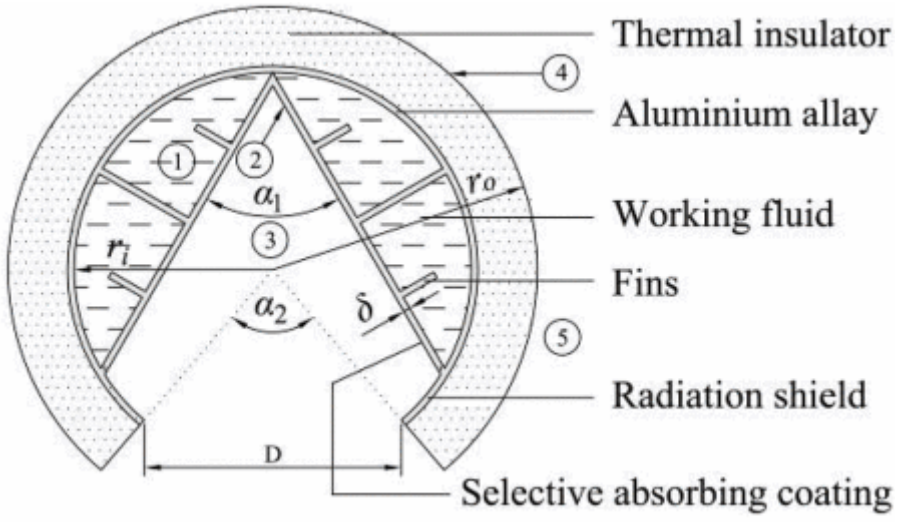



Figure 2-16: Cross-section of the triangle cavity receiver [88].

A radiation shield was placed at the aperture to reduce the view factor of the absorber pipe to the surrounding ambient. Experimental and theoretical work was conducted to study the heat loss due to the absorber inclination and the ambient wind speed. The results showed that the ambient wind speed had a relatively significant effect on heat loss, while the impact of the absorber inclination was relatively small. The heat loss was found to be 51.2 W/m, 53.2 W/m, 59.7 W/m and 61.8 W/m, when the inclination angles were 0°, 30°, 60° and 90°, respectively, at temperature differences between the working fluid and ambient of 150 ± 3 °C. At the inclination of 60° and temperature differences of 27 °C, 84.5 °C, 126.7 °C and 176.3 °C, the heat losses were 11.5 W/m, 30.4 W/m, 48.25 W/m and 71.55 W/m, respectively.

Furthermore, the heat losses of the cavity receiver were 76.6 W/m, 85.5 W/m, 96 W/m and 102.6 W/m, when the wind speeds were 1 m/s, 2 m/s, 3 m/s and 4 m/s, respectively, at the temperature difference of 150 ± 3 °C. At the wind speed of 3 m/s the temperature differences were 27.6 °C, 85.6 °C, 124.4 °C and 172.6 °C, and the heat losses were 17.3 W/m, 63 W/m, 83.85 W/m and 104 W/m, respectively.

In a windless case, the heat loss of this design is equivalent to that of UVAC3 evacuated receiver and the new-generation (UVAC2008)[89].

Two studies investigated the same design with an additional glass cover on the aperture [90][91]. Their objective was to reduce the heat loss from the aperture. The first study focused on heat transfer performance, where the investigation was theoretically and experimentally. The optical performance was studied using Monte Carlo ray-tracing method [90]. The design showed high optical efficiency of about 99% because the concentrated sunlight repeatedly reflected by the triangular shape with almost no escape [90]. Furthermore, the heat flux distribution of the heating surface of the design was heterogeneous, which could cause thermal stress at higher temperature [90]. The second study focused on thermal performance, also from a theoretical and experimental perspective [91]. The design had a good thermal performance in the medium temperature range, and it was comparable to that of the evacuated tube in that temperature range. The study involved the effect of the glass cover and the fins. These additions showed an improvement in thermal performance. Moreover, the heat transfer fluid temperature in this cavity design could exceed 570 K [91].

Fei Chen et al. [92] studied the optical properties of the triangular cavity absorber using a theoretical method. They found that the cavity absorber's aperture width, depth to width of the triangular shape, and the offset distance

from the focus of the triangular cavity were important parameters to improve the optical performance, where the cavity optical efficiency was 89.23%. It was recommended to select the depth to width ratio of 0.8 to 1, the aperture width of 70 mm, and the offset distance of 15 mm [92].

Figure 2-17 shows another design that is similar to the V- shape or triangular cavity. It consists of a center tube as absorber and two inclined fins which acted as the inner cavity surface with the glass cover over the aperture. A rectangular shell separated the cavity from the surrounding. The space between the shell and the absorber was filled with aluminum silicate fiber and asbestos rubber sheet between the glass cover and the end of the inclined fins. At the sides of the shell, there was a fixed axle to make the whole cavity movable. It rotated the system when solar irradiance was high enough to collect the concentrated solar energy[93][94]. The movable cavity mechanism was a novel design to prevent overheating while reducing heat loss. The study was based on experimental and theoretical investigations.

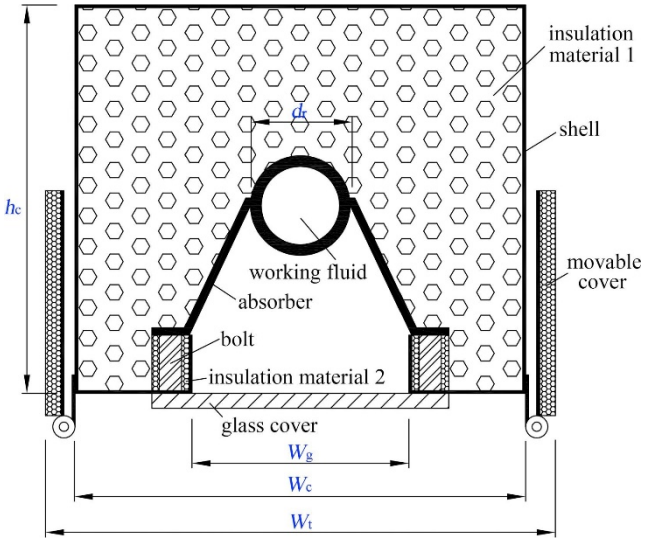



Figure 2-17: Cross-section of the V-shape cavity receiver [93].

Regarding the effect of the on-off state of the cover on heat loss, it was found that the heat loss of turning off the movable cover was less than that of turning on [94], where the heat loss reduction rate varied from 6.36% to 13.55%. The author found that the movable mechanism should be optimized for thermal insulation performance and operation control strategy [94]. The collector efficiency was tested at different inlet temperatures ranging from 80.6 ℃ to 160.5 ℃ and the mass flow rate from 170 to 181 g/s. The efficiency was in the range of 34.2% to 48.5% [93]. Further, the thermal conductivity of insulation materials was significantly improved the thermal performance of the design, i.e., the collector efficiency increased by 1.47 times, if the thermal conductivity of the insulation materials changed from 0.1 to 0.02 W. K/m [93]. Besides, the collector efficiency could increase by decreasing the emittance of the absorber and glass cover, i.e., the collector efficiency increased from 34.45% to 38.49% if the emittance of the absorber $\varepsilon_{ab}$and the glass cover $\varepsilon_G$ drop down from 0.9 and 0.95 to 0.1 and 0.15, respectively.

The efficiency of this design was comparable to the efficiency of the metal glass evacuated tube (64.25%). If we use the following optimized parameters:

- $\varepsilon_{ab} = 0.15$,

- $\varepsilon_G = 0.1$,
- absorption coefficient of the absorber in the visible region = 0.935,
- thermal conductivity of insulation material 1 (Figure 2-16) = 0.02 W/m.K,
- thermal conductivity of insulation material 2 = 0.1W/m.K [93].

Zhai H et al. [95] studied a triangle cavity at a lower temperature (< 200 °C). The optical efficiency simulated by using a light tracking method and the thermal performance was tested experimentally under temperature levels of 90 °C and 150 °C [95]. This study found that the triangle shape cavity receiver optical efficiency was 99%, and thermal losses were 20 W and 41 W (measured at 0.5 m of the receiver length) at the inlet temperature of 90 °C and 150 °C, respectively. Moreover, the solar conversion efficiency could be beyond 67% for the triangle cavity [95].

### D. Trapezoidal cavity receiver

Singh et al. [96][97] studied the effects of various design parameters of a trapezoidal cavity absorber on the thermal performance. The trapezoidal cavity absorber with a round pipe is shown in Figure 2-18. The absorber pipe was made of six mild steel round tubes brazed together in a single layer. The absorber pipe was at the upper portion of the cavity. Glass wool insulation was provided at the top and the sides of the pipes. At sidewalls of the cavity, ceramic tiles plates were provided. At the bottom part of the cavity, a glass plane was provided as a window for transmitting the solar radiation. Also, this study proposed another trapezoidal cavity receiver with a rectangular pipe absorber instead of round pipes to compare and evaluate their performance, see Figure 2-19. The dimensions of the designs were mentioned in detail in [96]. The thermal performance was measured for eight sets of identical designs with round pipe and rectangular pipe absorbers. The trapezoidal cavity with round pipe absorbers was tested in four different setups. The first two, the round pipe absorbers, were painted with ordinary matt black paint and black nickel coating (selective coating) with emissivity 0.91 and 0.17 at 100 °C, respectively. The other two, the cavity was fabricated with double (10 mm spacing) and single glass cover. Similar to the above mentioned scenarios, the trapezoidal cavity with the rectangular pipe absorbers was tested with four different setups. The experimental results showed that the difference between the heat loss coefficient of rectangular and round pipe absorbers in the trapezoidal cavity were not significantly different – they differed by a factor of 3.3 to 8.2 W/m$^2$, respectively [96]. The selective coating on the absorbers had a remarkable reduction of overall heat loss coefficient by 20% to 30 % compared to ordinary black paint. In addition, using double glass cover reduced the overall heat loss by 10% to 15 % compared to single glass cover [96].

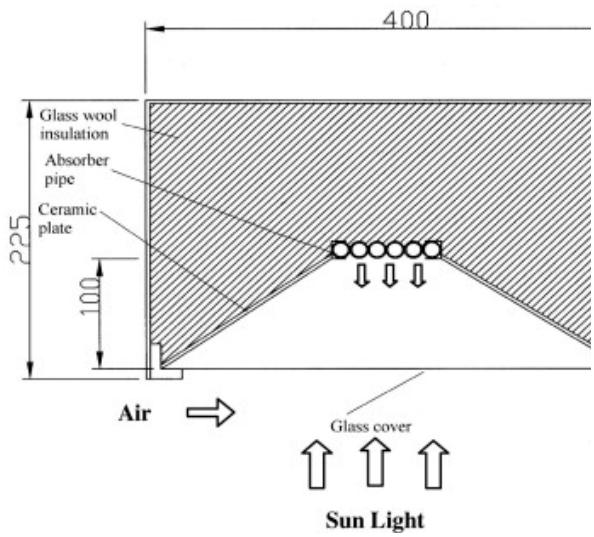



Figure 2-18: Cross-sectional of the trapezoidal cavity with round pipe absorber [96].

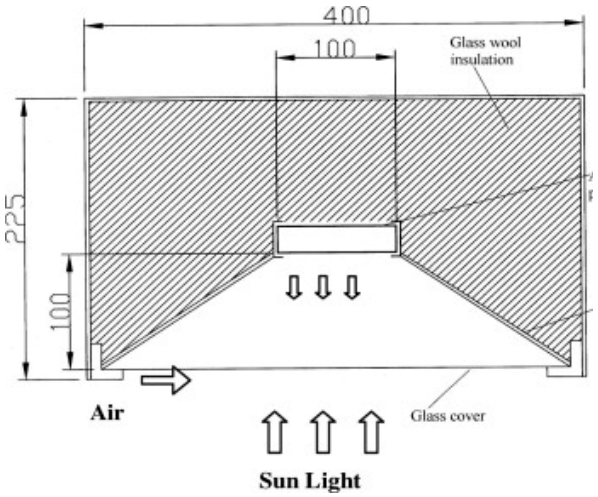



Figure 2-19: Cross-sectional of the trapezoidal cavity with rectangular pipe absorber [96].

Manikumar et al.[98] analyzed trapezoidal cavity numerically and experimentally. The cavity had a multi-tube absorber with a plate and without plate underneath, see Figure 2-20 and Figure 2-21 for various values of gaps between the tubes and depths of the cavity. The values of the overall heat loss and convective heat transfer coefficient were observed to increase with gaps between the tubes and the tube temperature. The thermal efficiency of the cavity with a plate was higher than without.

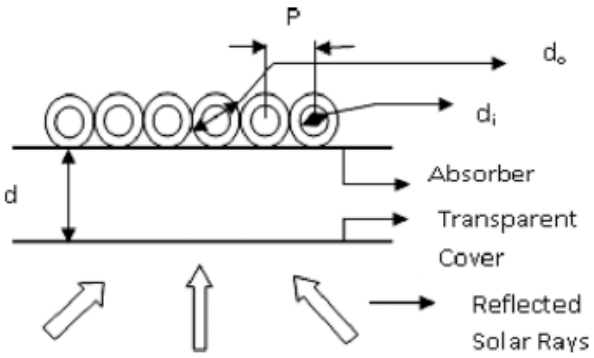



Figure 2-20: The arrangement of multi-tube absorber with plate [98].

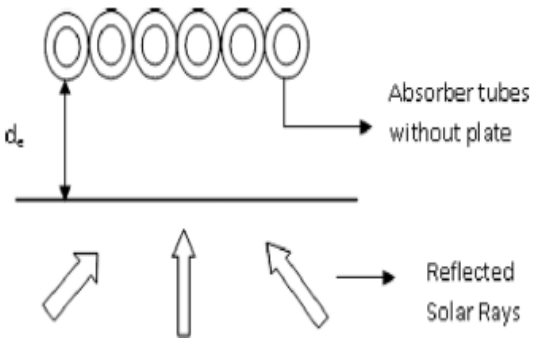



Figure 2-21: The arrangement of multi-tube absorber with plate [98].

Oliveira et al. [99] analyzed and optimized a trapezoidal cavity receiver via ray-trace and computational fluid dynamic (CFD) simulations. It was found that the cavity with six absorber tubes of 1/2" / 5/8" inner/outer diameters collects had higher optical efficiency. Further, the maximum inclination of 50° of the lateral cavity wall with respect to the bottom base was found to be optically acceptable. CFD simulation was used to optimize the cavity depth and rock wool insulation thickness. The lowest heat transfer coefficient was observed at the cavity depth of 45 mm. The insulation thickness of 35 mm of rock wool showed a good compromise between shading and insulations.

Reynold et al. [100] studied the heat transfer rate and the heat loss of the trapezoidal cavity experimentally with the aim of optimizing the cavity design to achieve maximum thermal efficiency and to develop a numerical model. Furthermore, the cavity was modeled by using a computational fluid dynamic (CFD) software package. The heat transfer rate and flow patterns showed reasonable agreement between the computational and experimental works,

but the heat loss that was measured by CFD was underestimated by about 40% compared to the experimental results. This discrepancy could not be explained. The heat transfer rate was compared between a uniform and non-uniform heating of the bottom wall with natural convection flows in a trapezoidal cavity using a finite element analysis with bi-quadratic elements (a method for evaluating the nonlinear coupled partial differential equations for flow and temperature fields) [101]. It was found that for all Raleigh numbers, the non-uniform heating of the bottom wall has a significant heat transfer rate as compared to uniform heating [101].
Moreover, the trapezoidal cavity receiver has been studied optically by Liang et al. [102]. The optical efficiency (it is the ratio between the solar radiation reaching the receiver absorber and the solar radiation coming from the concentrator mirror) of the total configuration was around 85% while the optical efficiency (the ratio of the solar radiation reaching the receiver absorber and the solar radiation coming from the concentrator mirror) of the absorber tube was about 45%.

Natarajan et al. [103] studied the effect of the Grashof number, absorber angle, aspect ratio (ratio of width and depth of cavity), surface emissivity and temperature ratio (ratio of the bottom and top surface temperature of the cavity) of the trapezoidal cavity. In their model, radiation and convection heat transfer was included. Consequently, the Grashof number has been included in the Nusselt number correlations. It was found that the effect of Grashof number on the combined heat loss (natural convection and surface radiation) was negligible. Further, the combined Nusselt number on the absorber angle was also negligible. The Nusselt number was decreased by increasing the aspect ratio and the temperature ratio, while an increase was observed in surface emissivity. Beyond the temperature ratio of 0.6 and aspect ratio 2.5, the combined heat loss variation in the cavity was not notable.

## 2.5 The proposed design of the receiver unit

### 2.5.1 Hot mirror coatings and its application on the conventional receiver

Materials for the use in solar applications are selected according to their optical properties in the visible and IR regions. These properties are absorptance $\alpha$, emittance $\varepsilon$, reflectance $\rho$, and transmittance $\tau$. Generally, the optical properties of the material surface can be changed entirely by coating on their surfaces with different materials. These properties are a function of the radiation wavelength, and each property has a spectral distribution. For example, the spectral transmittance $\tau_\lambda$, spectral absorption $\alpha_\lambda$, spectral reflection $\rho_\lambda$, and spectral emittance $\varepsilon_\lambda$ are the ratio of incident radiation transmitted, absorbed, reflected, and emitted from the medium at wavelength $\lambda$ to that of the total incident radiation at $\lambda$, respectively.

Hot mirror or low emittance coatings play a significant role in solar thermal conversion, transparent insulation for architectural windows, and photovoltaic conversion[60][104]. A hot mirror is a coating that is predominately transparent for over the visible wavelengths (0.3 to 77 micron) and reflective in the infrared wavelengths (2.0 – 100 micron) [104]. Hot mirror coatings can be a thin metal layer, doped semiconductors, or composite layer [64]. The thin metal layer is made by depositing a thin metal film on the glass substrate. Metals with a low IR emissivity are, for example, silver, gold, copper, or aluminum. Although, these materials have an excellent IR reflectivity

(>80%), the solar transmissivity is quite limited (less than 40%) [64]. Semiconductors thin layers are doped for an appropriate bandgap to have good transparency for visible light (up to 80%) and a lower IR-reflective coefficient, usually less than 85%. For example, Indium Tin Oxide ($In_2O_3$: Sn) with 200 nm film thickness has an average solar transmissivity of about 80% and an IR-reflective coefficient of 75% [64]. Composite layers are usually made by a thin noble metal layer between transparent dielectric layers. The solar transmissivity of this composite can be increased using a material with a high refractive index as an antireflective layer. The difficulty of increasing solar transmissivity is related to an accurate thickness deposition of different layers. For this reason, this solution is expensive and technically challenging [64].

Much work has been done on materials for hot mirror applications. A study by Lampert C.M [105] has suggested the application of a hot/heat mirror to be used as an alternative to selective absorbers in solar thermal collectors. This study focused on examining the optical properties of materials and coatings in a broad range. Granqvist C.G. [60] has found out from a survey of works on spectrally selective coatings that noble metals have poorly visible transmissivity, due to the shortwave reflection that occurs on the air/metal and metal/glass interface. The solar optical properties of thin films of noble metals (gold, silver) and transition metals were studied by Valkonen E. et al. [106]. Gold has shown the best properties for a coating which transmits visible solar radiation but reflects infrared radiation.
Furthermore, a comparison of hot mirror made from metal mesh grid and a selective absorber was made by Sievers A.J [59]. It was observed that the metal mesh hot mirror would be ideal at a higher temperature (800K). Also, Hamberg I. [107] and Granqvist C.G., studied the doped semiconductor Indium Tin Oxide (ITO). They reported that ITO is highly transparent for shortwave lengths and highly reflective for long wavelengths.

In analyzing the heat losses of the PTC receiver, all the infrared radiant and convection energy (in case of no vacuum in the annulus) transferred from an absorber, is conducted away through the glass cover. Therefore, the thermal losses from the receiver are directly related to the glass envelope temperature, and it does not matter what is happening inside the glass tube [108]. This raises the possibility of reducing heat losses by reducing the glass cover temperature. The effects of applying a hot mirror film have been modeled and studied previously. Grena [64] simulated the system, including heat reflection using hot mirror films with simplifying assumptions, and his results showed an increase in overall efficiency tested over a year by 4%. Also, a 2D simulation in this regard showed the possibility of increasing the working fluid's temperature to over $400^{\circ}C$ [52]. Other efforts of this type used a three-dimension model to take into account the radiation exchange by using different segmented surfaces inside the receiver along the pipe's length. This study showed that the hot mirror receiver effectively reduced the IR losses at higher temperatures, reduced the thermal stress on the glass cover and suggested use in a hybrid system [109], see Figure 2-22.

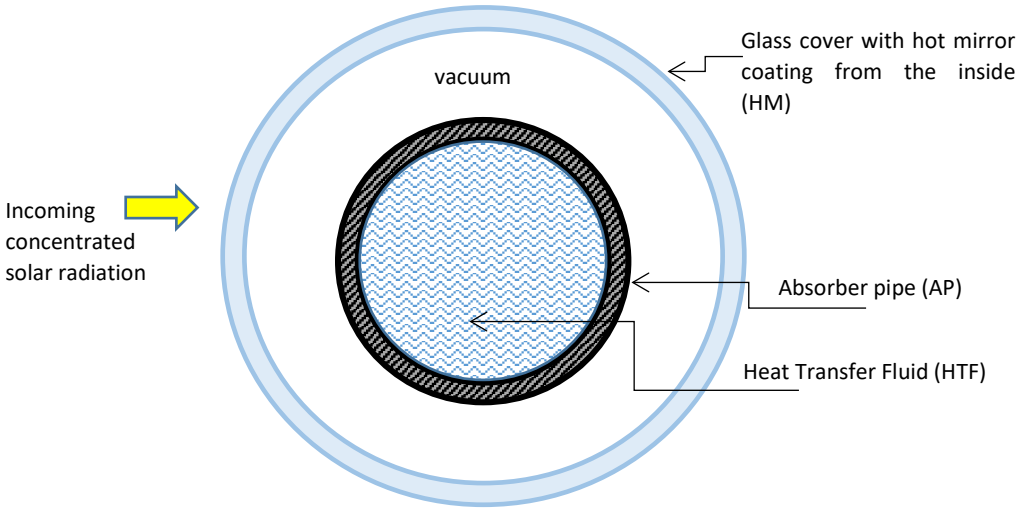



Figure 2-22: The cross-section of the receiver unit with a hot mirror coating on the glass cove envelop [48].

In practice, hot mirror coatings have not shown an improved overall efficiency of solar plants, but the advantage is their capacity of reaching much higher temperatures than their selective coating counterpart. Currently, hot mirror type systems are investigated, which may, in the near future, surpass selective coating technology [109].

### 2.5.2 The proposed cavity design with the hot mirror application

This design combines the use of the cavity receiver and hot mirror coating in a novel way [110]. The receiver consists of a highly reflective hot mirror coating on the inside of the borosilicate glass cover on the cavity aperture. The cavity inner surface is coated with a highly IR reflective material, such as polished aluminum. A vacuum in between minimizes convective losses, see Figure 2-23. The highly polished inner cavity surface reflects thermal radiation onto the absorber much more effectively than even a hot mirror coating.

The radiation interactions inside the cavity with additional novel aspects of the background theory are described and implemented in a validated simulation code, which are subsequently discussed in Chapter 3, Chapter 4, and Chapter 6. The simulation results indicate that the proposed design can exceed the HTF temperature ceiling compared to existing alternatives and can hence potentially increase the efficiency of the system. Further, the cavity geometry and a hot mirror coating at the aperture enable heightened retention of thermal radiation of the receiver.

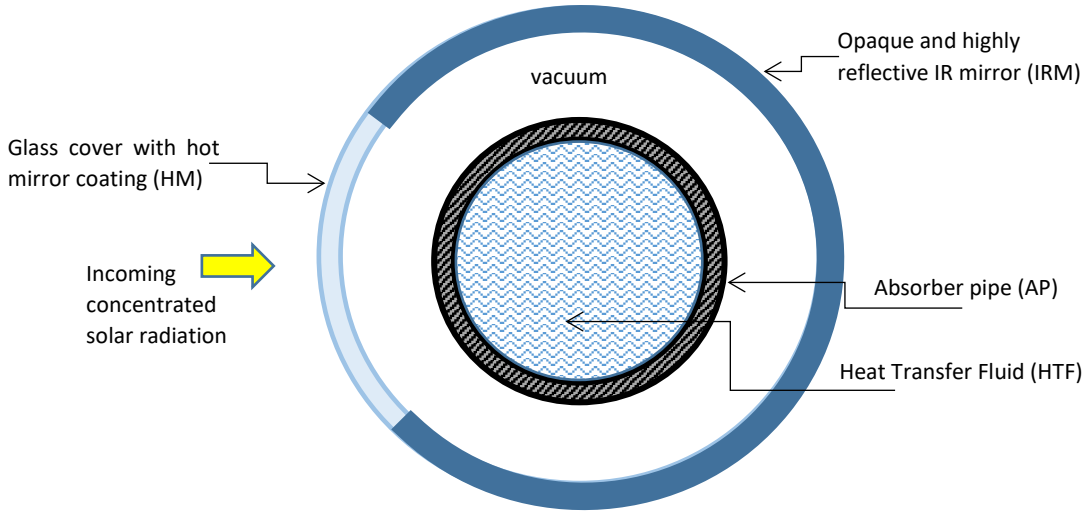



Figure 2-23: Cross-section of the cavity receiver with a hot mirror coating on the cavity aperture [52].

The simulation that is based on our model is validated by three experiment setups, which are described in Chapter 5. The cavity system was simulated and studied in many aspects using the operating conditions and design parameters for SEGS (Solar Electric Generating System) LS2, which is one of three generations of parabolic troughs installed in the nine SEGS power plants in California [32]. Different aperture sizes were simulated. Furthermore, different reflectivities for the inner surface of the cavity were studied. The effect of the hot mirror coating was investigated by comparing the system with and without the hot mirror application. In the end, the study performed a comparison of the cavity design with a conventional receiver with a selective coating and without coating (bare).

# Chapter 3 : The theoretical model of the cavity receiver with a hot mirror

## 3.1 Introduction

In this chapter, the theoretical model for the cavity receiver with a hot mirror is presented. The study considers two scenarios: the first case considers a non-uniform heat flux, which is due to the concentrated solar radiation by the parabolic mirror. The second case assumes a uniform heat flux, caused by a heating element inside the absorber pipe. The theoretical model is based on conservation of energy on the receiver unit components. The mathematical expressions of the heat transfer processes of the materials of the cavity mirror, hot mirror, and other potential materials, as well as the geometric parameters, are derived.

## 3.2 The cavity receiver design description

Fundamentally, the system consists of a highly IR reflective mirror on the inner cavity surface, such as polished aluminum and a hot mirror coating on the inside of the cavity aperture, which could be made from borosilicate glass. A vacuum in between minimizes convective losses, see Figure 3-1. The highly polished inner cavity surface reflects thermal radiation onto the absorber much more effectively than even a hot mirror coating.
The theoretical model of the solar receiver with the reflection interactions of the mirrored cavity and hot mirror will be derived in the following sections.

## 3.3 Descriptions of the heat fluxes

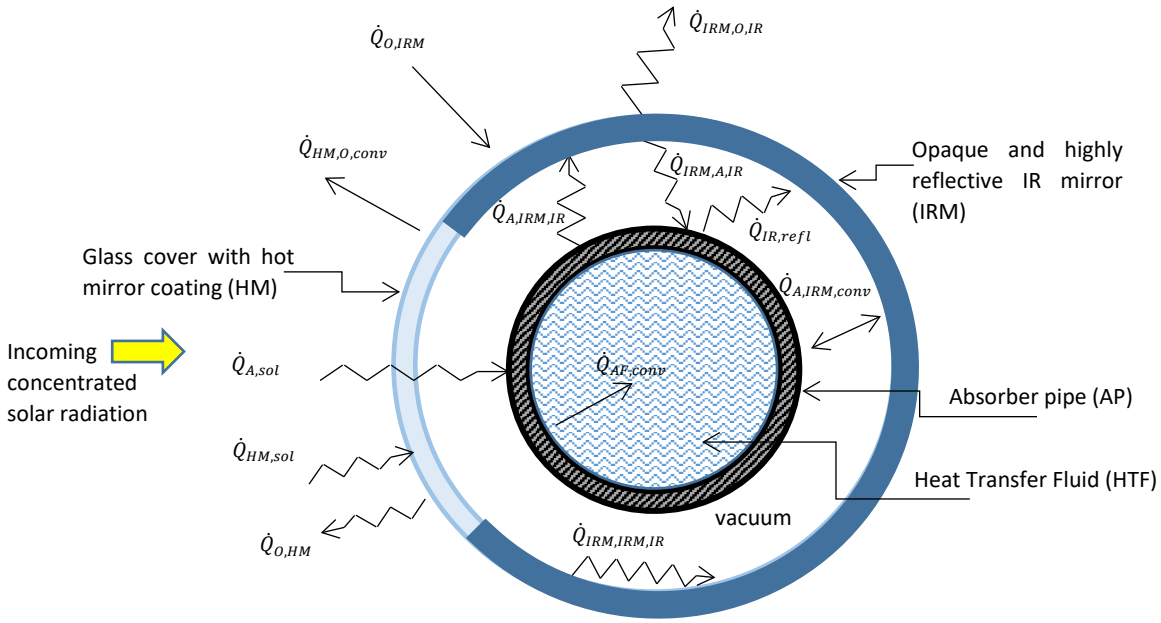



Figure 3-1: Schematic representation of the cavity design with the possible heat transfer modes (except conduction).

Under the steady-state condition, the heat flux of the receiver unit can with described by the help of Figure 3-1. The concentrated solar radiation from the parabolic trough mirror that enters the cavity aperture (HM), $\dot{Q}_{HM,sol}$, is transmitted and received by the absorber pipe (AP), $\dot{Q}_{A,sol}$, where it is mainly absorbed. The cavity

circumference, which includes the IR mirror (IRM) and the cavity aperture (HM), increases in temperature, emitting IR radiation from AP to IRM, $\dot{Q}_{A,IRM,IR}$, from IRM to AP, $\dot{Q}_{IRM,A,IR}$, and from IRM to IRM, $\dot{Q}_{IRM,IRM,IR}$, or is emitted to the outside (O), $\dot{Q}_{IRM,O,IR}$. The convective heat transfer from the AP into the HTF is represented by $\dot{Q}_{AF,conv}$, from the IRM to the outside by $\dot{Q}_{IRM,O,conv}$, and to a negligible extent, between the AP and the IRM by $\dot{Q}_{A,IRM,conv}$. Radiation impinges on IRM from the environment is represented by $\dot{Q}_{O,IRM}$. Conduction energy transfer is addressed through the thickness of the AP and HM, and between neighboring control volumes of different temperatures on the AP and HM, which is explained in more detail in section 3.5.1. However, the conduction through support fixtures (structural support members anchoring the receiver unit) was neglected.

IR radiation may also be reflected from the AP back onto itself via the mirror on the IRM or the hot mirror coating, $\dot{Q}_{IR,refl}$. Details of the back-reflected IR radiation over a cavity mirror or a hot mirror coating is given in Chapter 4, due to the importance of the reflected radiation.

## 3.4 Discretization of the receiver unit

Due to the non-uniform solar flux distribution around the circumference of the receiver unit, we discretized the receiver into finite control volumes (CV) to be able to evaluate their thermal interactions. The cavity circumference and the AP are segmented into $N_l$ CVs along the circumference (azimuthal direction), with $l$ given by $\frac{-(N_l-1)}{2} < l < \frac{(N_l-1)}{2}$ and $N_m$ segments along its axis (axial direction), where $m$ is $\frac{-(N_m-1)}{2} < m < \frac{(N_m-1)}{2}$. The HTF is only discretized along the axial direction, with segments identified by the label m, see Figure 3-2.

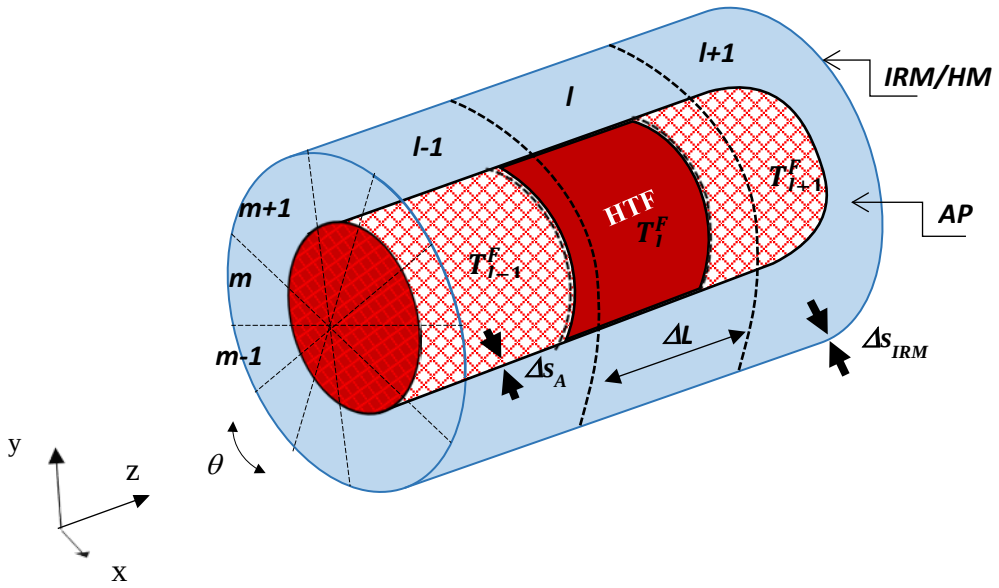



Figure 3-2: Discretization of the absorber pipe and the cavity cover into control volumes.

## 3.5 The description of the heat transfers

The description of the heat transfer on the absorber pipe (AP) control volume and cavity circumference (IRM or HM) control volume are completely defined in Figure 3-3. The terms in this figure will be explained in the subsequent sections.

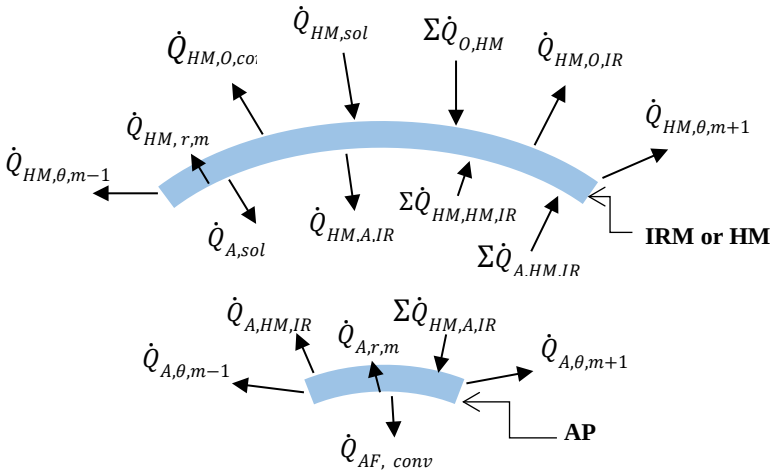



Figure 3-3: Heat exchange terms on the absorber pipe (AP) and the cavity cover (IRM or HM).

Figure 3-3 is a cross-section view of a discretized receiver unit for HM control volume and absorber pipe control volume with the same arc angle. The size of the control volume is considered to be small enough with a close approximation $< r_A$ ($r_A$ is the radius of the absorber pipe) so that the temperature varies linearly between neighboring control volumes centers. The cavity opening (HM) and the IR mirror (IRM) have the same description and heat transfer analysis processes but with different optical properties. Therefore, the physical processes are identical for HM and IR reflection region and the thesis will make use of HM only. In the simulation code, they will be identified according to their properties and their positions along the receiver circumference. We assumed that the thickness of HM and IRM are approximately the same. The remaining terms in Figure 3-3 are discussed below.

### 3.5.1 Conduction heat transfer

The conductive heat transfers occur between control volumes along the azimuthal (θ), the axial (z) direction and along the radial (r) direction. The contribution in the axial direction ($\dot{Q}_{A,z,m\pm1}$ and $\dot{Q}_{IRM,z,m\pm1}$) are ignored due to the small temperature gradient and the constant solar irradiation along the axial direction [111][112]. Therefore, conduction heat transfers are only considered along the azimuthal direction and radial direction of the absorber pipe and cavity cover. Conduction heat transfer is described by the Fourier law of conduction [113][114] as

$$\dot{Q}_{cond} = -k\,A\,\frac{dT}{dx}. \tag{3.1}$$

The rate of heat conducted is proportional to the medium's surface area A, where A is perpendicular to the direction of heat flow, and the temperature change with respect to a length *dx* in the direction of heat flow. The proportionality constant is the material thermal conductivity *k*, and the negative sign means that the heat transfer is a positive quantity in the positive direction of *x*.

The conductive heat transfer along the azimuthal direction between neighboring control volumes on the absorber pipe control volume ($A_{ml}$) is written as:

$$\dot{Q}_{A,\theta,m} = \dot{Q}_{A,\theta,m-1} + \dot{Q}_{A,\theta,m+1} = k_A \frac{T^A_{ml} - T^A_{m-1,l}}{\left(r_A + \frac{\Delta s_A}{2}\right)\theta} \Delta s_A \Delta L + k_A \frac{T^A_{ml} - T^A_{m+1,l}}{\left(r_A + \frac{\Delta s_A}{2}\right)\theta} \Delta s_A \Delta L =$$

$$k_A \frac{2T^A_{ml} - T^A_{m+1,l} - T^A_{m-1,l}}{\left(r_A + \frac{\Delta s_A}{2}\right)\theta} \Delta s_A \Delta L \,,$$

$$\dot{Q}_{A,\theta,m} = k_A \frac{2T^A_{ml} - T^A_{m+1,l} - T^A_{m-1,l}}{\left(r_A + \frac{\Delta s_A}{2}\right)\theta} \Delta s_A \Delta L, \tag{3.2}$$

and similarly, for the HM

$$\dot{Q}_{HM,\theta,m} = k_{HM} \frac{2T^{HM}_{ml} - T^{HM}_{m+1,l} - T^{HM}_{m-1,l}}{\left(r_{HM} + \frac{\Delta s_{HM}}{2}\right)\theta} \Delta s_{HM} \Delta L. \tag{3.3}$$

For the conductive heat transfer through the thickness in the radial direction on the absorber pipe control volume ($\dot{Q}_{A,r,i}$ ) is written as:

$$\dot{Q}_{A,r,m} = k_A \frac{T^A_{ml,out} - T^A_{ml,in}}{\Delta s_A} r_A \theta \Delta L, \tag{3.4}$$

and similarly, for the HM

$$\dot{Q}_{HM,r,m} = k_{HM} \frac{T^{HM}_{ml,out} - T^{HM}_{ml,in}}{\Delta s_{HM}} r_{HM} \theta \Delta L. \tag{3.5}$$

where $k_A$ and $k_{HM}$ are thermal conductivities of absorber pipe and HM respectively, $T^{A\ or\ HM}_{ml}$ is the temperature of the m$^{th}$ control volumes' center point on absorber pipe or HM, in and out subscripts in Eq. (3.4) and Eq. (3.5) are for the inside and outside surface temperatures, and the remaining symbols are defined in Figure 3-2.

### 3.5.2 Convection heat transfer

The convective heat transfer is a mechanism that occurs due to bulk movements in fluids [43]. The type of convection heat transfer depends on the origin of fluid motion. If the fluid is forced to flow by external means such as a fan or a pump, the convection heat transfer is called "forced" convection. If the fluid motion happens by natural means such as the buoyancy effect, the convection is called "natural". The rate of convective heat transfer is found to be proportional to the temperature difference, which can be expressed by Newton's law of cooling [113][114] as:

$$\dot{Q}_{Conv} = h\, A_s \left(T_s - T_f\right), \tag{3.6}$$

where *h* is the convection heat transfer coefficient, $A_s$ is the heat transfer surface area, $T_s$ is the temperature of the surface, and $T_f$ is the temperature of the fluid sufficiently far from the surface.

The contribution of the convective heat transfer in the parabolic trough solar receiver happens in three situations: firstly, the convective heat transfer between the HTF and the absorber pipe, from the HM to the environment, and from the absorber to the cavity envelope (HM +IRM). The last can be neglected due to the existence of a vacuum in the annulus.

#### 3.5.2.1 Convection heat transfer between HTF and the absorber pipe

The convection heat transfer between the absorber pipe wall to the HTF is forced convection due to the fluid motion by an external means. This transfer occurs from all absorber pipe control volumes across the circumference to the HTF segment *l*, and is expressed as:

$$\left(\dot{Q}_{AF,conv}\right)_l = \sum_{m=1}^{N_m} h_f [r_A \theta \Delta L](T_{ml}^A - T_l^F), \tag{3.7}$$

where $T_{ml}^A$ is the absorber pipe average temperature of the control volume "*ml*", $T_l^F$ is the average HTF temperature at the segment *l* and the control volume area in thermal contact with the HTF is given by the expression inside the square brackets. The HTF convective heat transfer coefficient [113][54] is defined as

$$h_f = \frac{\mathrm{Nu} \cdot k_A}{2r_A}, \tag{3.8}$$

where *Nu* is the Nusselt number. The Nusselt number is the convection heat transfer relative to the conduction heat transfer across the same fluid layer, which represents how the convective heat transfer is more effective than the conductive heat transfer through a fluid layer. The convection heat transfer depends on the type of flow through the receiver unit. The flow in a parabolic trough receiver unit is well within the turbulent flow region at typical operating conditions [36]. The following is a Nusselt correlation "*Nu*" for the convective heat transfer from the absorber pipe to the HTF for turbulent and transitional flow cases derived by Gnielinski [115]

$$Nu = \frac{f_{a,in}/8(Re-1000)Pr_{T_f}}{1+12.7\sqrt{f_{a,in}/8}\left(Pr_{T_f}{}^{2/3}-1\right)}\left(\frac{Pr_{T_f}}{Pr_{T_{a,in}}}\right)^{0.11}, \tag{3.9}$$

where

$$f_{a,in} = (1.82\log_{10}(Re) - 1.64)^{-2}, \tag{3.10}$$

$f_{a,in}$ is the inner surface of the absorber pipe friction factor, $Pr_{T_f}$, and $Pr_{T_{a,in}}$ are Prandtl numbers evaluated at the temperatures of the HTF and the inner surface of the absorber pipe respectively, and *Re* is the Reynolds number. *Re* and *Pr* are expressed as

$$Pr = \frac{\mu C_P}{k}, \qquad Re = \frac{\rho V L_c}{\mu}, \tag{3.11}$$

where $\mu$ is the dynamic viscosity, $\rho$ is the fluid density, $V$ is the upstream velocity, and $L_c$ is the characteristic length ($L_c$ for the circular tube is the tube diameter). The Prandtl number *Pr* is the molecular diffusivity of momentum relative to molecular diffusivity of heat, which is directly related to the relative thickness of the velocity and the thermal boundary layer and its value ranges from $< 0.01$ for liquid metal to $> 10^5$ for heavy oils [43]. The Reynolds number *Re* is the ratio of the inertia forces to viscous forces in the fluid. The *Nu* correlation in Eq. (3.9) is valid for $0.5 < Pr_{T_f} < 2000$ and $2300 < Re < 5 \times 10^6$ [36].

### 3.5.2.2 Convection heat transfer from the HM to the atmosphere

The convection heat transfer from the HM to the ambient is the most dominant source of heat loss, especially if there is wind [36]. Evaluating the convection heat transfer from Eq. (3.7) required the correlation for the heat convection coefficients or *Nu* for whether the convection heat transfer to the ambient with no wind case (natural convection) or with wind case (forced convection).

**In wind case**, the convective heat transfer from the HM to the environment is described by an equation similar to Eq. (3.7)

$$\left(\dot{Q}_{HM,O,conv}\right)_{ml} = \sum_{m=1}^{N_m} h_w[(r_{HM} + \Delta s_{HM})\theta\Delta L](T_{ml}^{HM} - T^O), \tag{3.12}$$

with $T_{ml}^{HM}$ is the average control volume temperature on the HM, $T^O$ is the ambient temperature and the heat transfer coefficient $h_w$ is called the wind coefficient [116]. It is expressed as

$$h_w = 4{v_w}^{0.58} \times (2(r_{HM} + \Delta s_{HM}))^{-0.42}, \tag{3.13}$$

where $v_w$ is the wind velocity. $v_w$ has to be in the range from 1.5 to 10 m/s [116]. All other quantities are defined in Figure 3-2.

**In no wind case**, the convection heat transfer from the HM cover to the ambient is natural convection. For this case, the empirical correlation for the average *Nu* over a horizontal cylinder developed by [117] will be used

$$Nu_{HM} = \left(0.6 + \frac{0.387{Ra_{HM}}^{1/6}}{\left[1+\left(0.559/Pr_{T_G}\right)^{9/16}\right]^{8/27}}\right)^2, \tag{3.14}$$

$$Ra_{HM} = \frac{g\beta(T_{ml}^{HM} - T^O)\times(r_{HM} + \Delta S_{HM})^3}{\nu^2}\, Pr_{T_G}, \tag{3.15}$$

where $Ra_{HM}$ is the Rayleigh number for air based on the HM outer diameter, $(r_{HM} + \Delta S_{HM})$ is the HM outer

diameter, see Figure 3-2, $g$ is the gravitational constant, $\beta$ is the volumetric thermal expansion coefficient, which is the inverse of average temperature between the ambient air temperature $T^O$ and the $T_{ml}^{HM}$ for HM control volume outside temperature with the assumption that the air is an ideal gas. The kinematic viscosity of air at average temperature is represented by $\nu$.

The correlation mentioned above is valid for $10^5 < Ra_{HM} < 10^{12}$. The Rayleigh number is also defined by the product of the Grashof number, which describes the relationships between viscosity and buoyancy of the fluid, and the Prandtl number [43].

### 3.5.3 Radiation heat transfers

The radiation heat transfer in an evacuated receiver unit in the annulus and from the HM to the environment contributes significantly to the heat losses, especially at a higher temperature. Some basic definitions need to be stated to proceed. For example, in order to evaluate the radiative heat exchange between two surfaces, the total radiation energy that leaves the surface and the angle in space through which the other surfaces intercept the radiation needs to be known. The total radiation energy that leaves a surface (emitted or reflected) per unit area per unit time is called Radiosity, which can be expressed as

$$J = \varepsilon\sigma A T^4 + \rho S, \tag{3.16}$$

where $\varepsilon$ is the surface emissivity, $\sigma$ is the Stefa-Boltzmann constant, and $\rho S$ is the reflected radiation by a surface with reflectivity $\rho$, and $S$ is the incident radiation energy per unit time per unit area.

The angle in space through which the radiation is intercepted by some other surface is called the solid angle Ω, see Figure 3-4. The definition of a solid angle makes it possible to introduce the concept of the "view factor". The view factor $F_{12}$ is the fraction of the radiation leaving a surface 1 which strikes a surface 2. It is a geometric quantity that depends on the relative orientation between the surfaces and is independent of the temperature and surface properties [43]. The way to determine the view factor is illustrated in Figure 3-4. Assuming that a differential area $dA_1$ emits radiation with a constant intensity $I$, the total radiation rate leaves $dA_1$ in all directions is

$$\dot{Q}_1 = \pi\, I\, dA_1 = J_1 dA_1, \tag{3.17}$$

where the radiosity $J$ can be written as $= \pi\, I$. A fraction of this radiation strikes another differential area $dA_2$. This radiation can be expressed as follows

$$\dot{Q}_{12} = I\, \cos\theta_1 dA_1\, d\Omega_{21}. \tag{3.18}$$

Eq. (3.18) describes the rate of radiation $\dot{Q}_{12}$ that leaves the surface $dA_1$ at an angle $\theta_1$ and strikes the surface $dA_2$ at an angle $\theta_2$ and with a solid angle $d\Omega_{21} = \frac{dA_2 \cos\theta_2}{d^2}$ and the distance between their centers is $d$. The view factor $F_{12}$ from the differential area $dA_1$ to $dA_2$ can be written as

$$F_{12} = \frac{\dot{Q}_{12}}{\dot{Q}_1} = \frac{\cos\theta_1 \cos\theta_2}{\pi\, d^2}\, dA_2. \tag{3.19}$$

The approach mentioned above is usually complex and difficult to calculate, even with simple geometries. In most

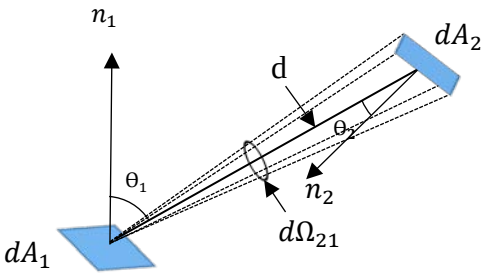



Figure 3-4: Illustration of the view factor determination between two surfaces.

of the literature, the view factor for common geometries is calculated and given in a graphical, tubular, and analytical form. In geometries that are very long in one dimension compared to the other dimension, such as ducts and pipes, an approximation of the view factor can be made using an approach called Hottel's crossed string method [118]. In this study, the PTC receiver unit was considered as "infinitely" long in the sense that edge effects were ignored.

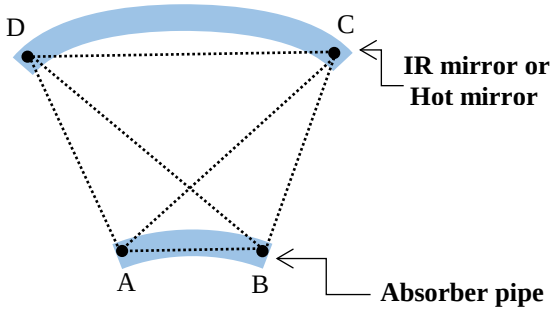



Figure 3-5: Determination of the view factor in the discretized receiver unit using the crossed string method.

Figure 3-5 illustrates the Hottel's crossed string method. The determination of the view factor from absorber pipe (AP) to IRM $F_{AP,IRM}$ as shown in Figure 3-5**Error! Reference source not found.** starts by identifying the endpoints of the surface AP (A and B) and the surface IRM (C and D) and then drawing uninterrupted lines across faces of AP and IRM and joining the endpoints with the straight lines. The view factor approximation by the Hottel's crossed strings method can be expressed as

$$F_{AP,IRM} = \frac{\sum crossed\ strings - \sum uncrossed\ strings}{2 \times the\ string\ of\ AP\ surface} = \frac{(AC+BD)-(AD+BC)}{2 \times AB}, \tag{3.20}$$

where the crossed lines are AC and BD and the uncrossed lines are AD and BC. The view factor calculations from AP control volume to HM control volumes and from HM control volume to HM control volumes are shown in detail in Appendix II. Also, the number of HM control volumes that are in thermal contact with AP control

volumes and vice versa and the number of HM control volumes that are in thermal contact with HM control volume are derived in Appendix II.

The radiation exchange between the receiver unit component surfaces includes the visible and IR radiation. In the receiver unit of the PTC, each absorber pipe (AP) control volume radiatively interacts with the HM control volumes. Further, the AP control volume exchanges the radiation with the other AP control volumes via IR reflections on the HM or IRM. The surface of the AP material is assumed to be diffuse and gray, while the HM or IRM surface is gray and a specular reflector to incoming IR radiation. The net radiation method [119] is going to be applied to each control volume to determine the effective radiation exchange, which is discussed in the following subsections. A view factor notation $F_{km}^{AP,HM}$ is going to be used afterward. It describes the view factor from control volume "*k*" in AP material to control volume "m" in the HM material.
The detailed derivation of the total radiations incident on every control volume will be discussed in Chapter 4 and Chapter 6.

# Chapter 4 : Derivation of the reflection mechanism

## 4.1 Introduction

In Chapter 3, we derived all the heat exchange modes in the receiver unit. Furthermore, the net radiation exchange for each control volume (CV) on the absorber pipe (AP) and the outer cover of the receiver unit was presented. This chapter discusses the mechanism of the reflected radiation inside the receiver unit and presents the derivation of the first and second IR reflection terms. The reflection mechanism aspect is one of our primary interests. Before proceeding with the derivation of the reflection mechanism, the following assumptions are made:

- The control volumes are small enough to be considered as a flat.
- Maximally, the IR radiation reflects twice before absorber pipe absorbs it.
- In the temperature range of interest, the optical properties of the reflective surface are approximately constant.

## 4.2 The reflected radiation terms

An essential aspect of this work is to account for reflected radiation. The reflected radiation is essential when the radiation is reflected onto the absorber pipe (AP) from the cavity mirror (IRM) and the hot mirror coating for partial reabsorption. The reflections that we consider are: the first reflection, which is denoted by $\left(\dot{\boldsymbol{Q}}_{\boldsymbol{IR,1\,refl}}\right)_{ml}$ (represents the reflection from AP to HM to AP), secondary reflection, which is denoted by $\left(\dot{\boldsymbol{Q}}_{\boldsymbol{IR,2\,refl}}\right)_{ml}$ (AP to HM to AP to HM to AP), and the secondary reflection on the inner cavity surface, which is denoted by $\left(\dot{\boldsymbol{Q}}_{\boldsymbol{IR,2\,refl,HM}}\right)_{\boldsymbol{lm}}$(AP to HM to AP to HM). The effect of the secondary reflection on AP and HM depends on the reflection coefficients of both the cavity ($\boldsymbol{\rho_{HM,IR}}$), and the AP ($\boldsymbol{\rho_{A,IR}}$). We assumed that the optical properties of HM are approximately constant within the temperature range of interest, and their average values are used. If more detailed results for different temperatures are needed, the parameters can be changed or made temperature dependent in the simulation. We further assumed that the radiation is emitted from the center of the surface of each control volume (AP and HM). Furthermore, the AP control volumes are diffuse and gray, and the IRM is a specular reflector inside the receiver and opaque from the outside, while the HM is a gray and specular reflector to incoming IR radiation. The AP, HM, and IRM optical properties are characterized in terms of visible and IR radiations of the irradiated solar radiation, and thermal radiation.

## 4.3 The first reflected radiation term $\dot{Q}_{IR,1\ ref}$

The first reflection occurs on the HM or IRM, which is a specularly reflected surface. In Figure 4-1, $A_{kl}$ control volume on the absorber pipe emits IR radiation that is received by another $A_{il}$ control volume on the absorber pipe via reflection on the $HM_{ml}$ control volume. The amount of radiation received by $A_{il}$ control volume depends on the view factor towards the $HM_{ml}$ control volume. It requires the magnitude of the emitted radiation by $A_{kl}$, reflected radiation by $HM_{ml}$ and the absorbed radiation by $A_{il}$. Determining the amount of radiation received by $A_{il}$ on the absorber pipe from $A_{kl}$, as shown in Figure 4-1, helps to sum the IR contributions from all the absorber pipe control volumes that are in radiative contact with $A_{il}$ via the first reflection.

The first reflection can be determined by the help of the simplified scheme in Figure 4-1. $A_{kl}$ emits radiation diffusely towards the HM control volumes, a fraction of this radiation strikes $HM_{ml}$ control volume with an amount of radiation equal $\dot{Q}_{IR,A_{kl}} F_{A_{kl},HM_{ml}}$ where $\dot{Q}_{IR,A_{kl}}$ is the emitted radiation from $A_{kl}$ and $F_{A_{kl},HM_{ml}}$ is the view factor from $A_{kl}$ to $HM_{ml}$. This radiation is going to be received by $A_{il}$ via specular reflection taking place by $HM_{ml}$ with an amount of radiation equal $\rho_G \dot{Q}_{IR,A_{kl}} F_{A_{kl},G_{ml}}$

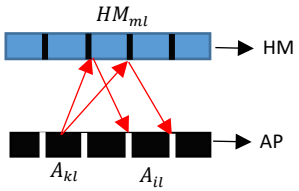



Figure 4-1: Simple schematic representation to show the mechanism of the first reflection between absorber pipe (AP) and hot mirror (HM).

As discussed in Chapter 3, the receiver unit is discretized into control volumes, as shown in Figure 3-2. The arc length of the absorber pipe and HM control volume have the same central angle "Θ". In previous discretization (Figure 3-2), the control volume "ab" and "cd" were used. Radiation emitted from the center of absorber pipe control volume "cd" in a cone is shown in Figure 4-2. We redefine the outer cover (HM or IRM) control volume such that it lies between normal 1 and normal 2 in order for all radiation from "cd" to be reflected back onto itself. Geometric optics shows that the arc length between "a" and normal 2 (as well as normal 1 and "b") is exactly half the arc length between normal 1 and normal 2. Therefore, we must increase the number of the HM control volumes to be twice that of the absorber pipe control volumes in order to capture all the reflected radiation.

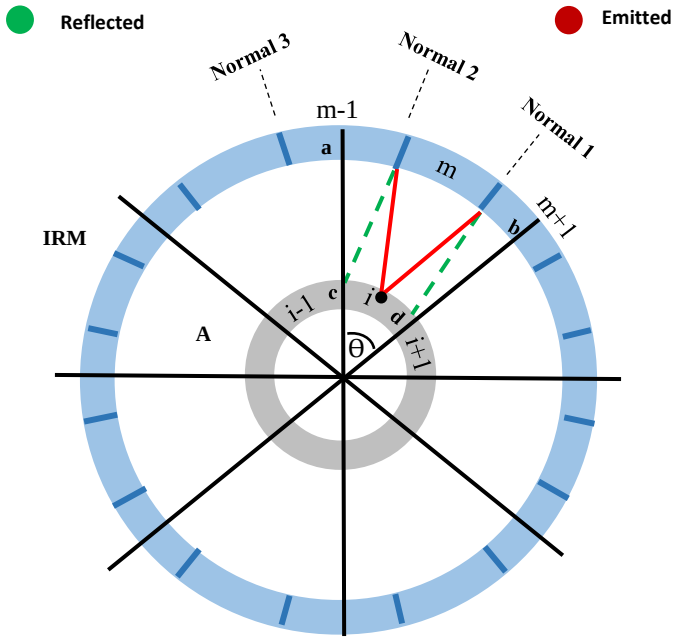



Figure 4-2: Discretize the HM into normal and offset CVs (the index in the axial direction is "l", see Figure 3-2).

### 4.3.1 Summation of all first reflection contributions to $A_{il}$

The contributions from all absorber pipe control volumes that are in radiative contact with $A_{il}$ via reflection will contribute towards the total received IR radiation by $A_{il}$. These contributions were summed. Along the circumference, the farthest HM control volume that can be viewed by $A_{il}$ constitutes the extreme reflection from the farthest absorber pipe control volume which is depicted and calculated in Appendix II.

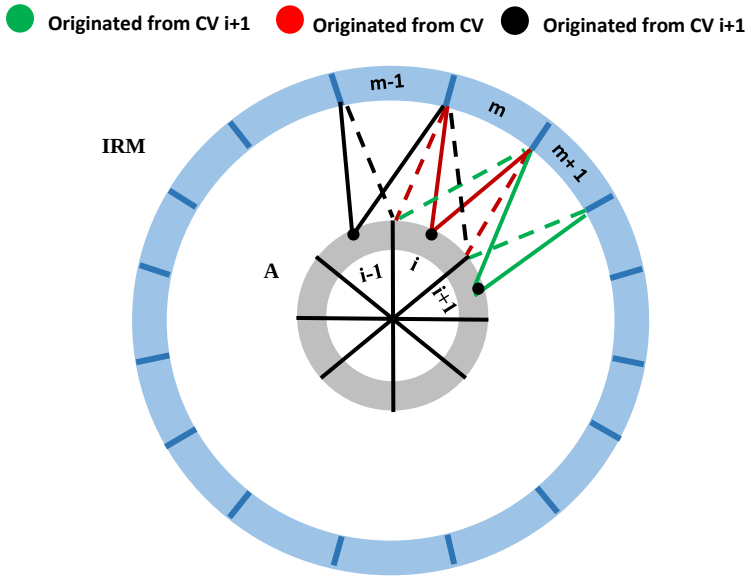



Figure 4-3: Absorber pipe control volume with index *i* receives reflected radiation from $A_i$, $A_{i+1}$ and $A_{i-1}$via reflection over $HM_m$, $HM_{m+1}$, and $HM_{m-1}$, respectively.

In Figure 4-3, the red solid and dash colors represent the emitted radiation from $A_{i,l}$ towards $HM_{m,l}$ and the reflected radiations from $HM_{m,l}$ to $A_{i,l}$, respectively. The green solid and dash colors represent the emitted

radiation from $A_{i+1,l}$ towards $HM_{m+1,l}$ and the reflected radiations from $HM_{m+1,l}$ to $A_{i,l}$, respectively. The black solid and dash colors represent the emitted radiation from $A_{i-1,l}$ towards $HM_{m-1,l}$ and the reflected radiations from $HM_{m-1,l}$ to $A_{i,l}$, respectively. The subscripts *i* and *m* stand for the index number in the azimuthal direction and *l* stands for the index in the longitudinal direction. By extending the situation of the first reflection of an emitted radiation via one HM CV and received by $A_{il}$ (previously mentioned, see Figure 4-1) to the neighboring elements, see Figure 4-3, the sum of all contributions on $A_{il}$ by first reflection can be expressed as

$$\left(\dot{Q}_{IR,1ref}\right)_{ml} = \sum_{\substack{k=i+H,\\ m=2i+H,\\ H=0}}^{H=N_R} \rho_{G_{ml}} \dot{Q}_{IR,A_{kl}} F_{A_{k,l}G_{m,l}} + \sum_{\substack{k=i-H,\\ m=2i-H,\\ H=1}}^{N_L} \rho_{G_{ml}} \dot{Q}_{IR,A_{kl}} F_{A_{k,l}G_{m,l}} \quad (4.1)$$

,

The first and the second terms in Eq. (4.1) are the sum of the reflection contributions originating from the right and the left of $A_{il}$, where $N_R$ and $N_L$ are the maximum numbers of absorber pipe control volumes that are in radiative contact with $A_{il}$ on their respective sides. $N_R$ and $N_L$ are calculated and discussed in Appendix II.

### 4.3.2 The effect of the first reflection on the hot and IR mirrors control volumes

The hot mirror or IR mirror (HM/IRM) control volumes partially absorb the emitted radiation from the absorber pipe due to the absorption coefficient of the HM/IRM material. Although the absorption coefficient is very small compared to that of the absorber pipe, this contribution was accounted for. In Figure 4-4 and Figure 4-5, the two possibilities of light cones originating from different absorber pipe control volume falling onto one HM control volume are depicted.

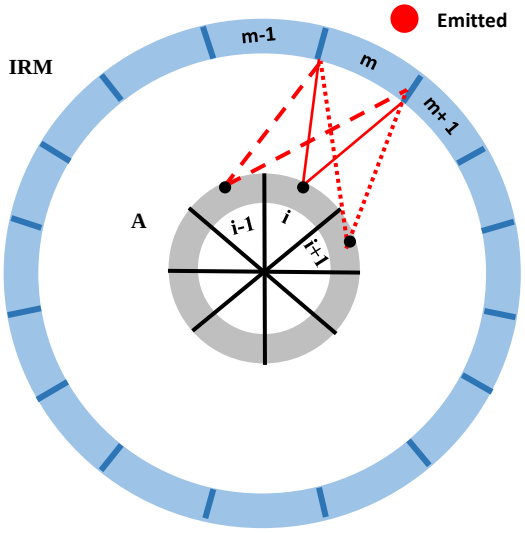



Figure 4-4: HM control volume received the emitted absorber pipe control volumes radiation (case 1).

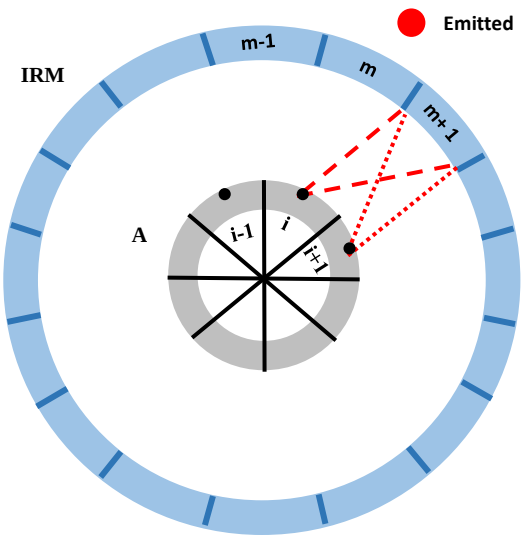



Figure 4-5: HM control volume received the emitted absorber pipe control volumes radiation (case 2).

The absorbed part of the reflected radiation from HM is represented as follows:

For the case of the HM control volume in Figure 4-4

$$\left(\dot{Q}_{IR,1ref,HM}\right)_{ml} = \left(1-\rho_{HM_{ml}}\right) \times \sum_{\substack{k=\left(\frac{m}{2}\right)+H \\ ,H=0}}^{H=N_R} \dot{Q}_{IR,A_{k,l}} F_{A_{k,l}HM_{m,l}} + \left(1-\rho_{HM_{ml}}\right) \times \sum_{\substack{k=\left(\frac{m}{2}\right)-H \\ ,H=1}}^{H=N_L} \dot{Q}_{IR,A_{k,l}} F_{A_{k,l}HM_{m,l}} \quad (4.2)$$

.

For the case of the HM control volume in Figure 4-5

$$\left(\dot{Q}_{IR,1ref,HM}\right)_{ml} = \left(1-\rho_{HM_{ml}}\right) \times \sum_{\substack{k=\left(\frac{m}{2}\right)+H \\ ,H=1}}^{H=N_R} \dot{Q}_{IR,A_{k,l}} F_{A_{k,l}HM_{m,l}} + \left(1-\rho_{HM_{ml}}\right) \times \sum_{\substack{k=\left(\frac{m}{2}\right)-H \\ ,H=1}}^{H=N_L} \dot{Q}_{IR,A_{k,l}} F_{A_{k,l}HM_{m,l}} \quad (4.3)$$

.

## 4.4 The second reflected radiation term $\dot{Q}_{IR,\,2ref}$

The second reflection is the reflection from absorber pipe (AP) to HM to AP to HM to AP. It strongly depends on the values of $\rho_{HM}$ and $\rho_A$ for the HM and the absorber pipe reflectivity coefficients, respectively. The scenario of the second reflected radiation continues from the first reflection. When absorber pipe control volume receives the reflected radiation, the absorber pipe control volume will diffusely reflect the unabsorbed part of this radiation to every direction of its view. These diffusely reflected radiations will again specular reflected by the HM control volumes towards absorber pipe control volumes.

$$\left(\dot{Q}_{IR,2ref}\right)_{il} = \rho_{ab} \sum_{\substack{k=i+H \\ m=2i+H \\ H=0}}^{H=N_R} \rho_{HM_{m.l}} F_{A_{k,l}HM_{m,l}} \left(\dot{Q}_{IR,1ref}\right)_{k,l} + \rho_{ab} \sum_{\substack{k=i-H \\ m=2i-H \\ H=1}}^{H=N_L} \rho_{HM_{m.l}} F_{A_{k,l}HM_{m,l}} \left(\dot{Q}_{IR,1ref}\right)_{k,l} \quad (4.4)$$

.

### 4.4.1 The effect of the second reflection on the hot and IR mirrors control volumes

In the same way as discussed in section 4.3.2, the HM control volumes partially absorb the diffusely reflected radiations from absorber pipe control volumes, but this effect is less than the effect of the first IR reflection on the HM control volumes. The amount of radiation that has been absorbed by the HM control volumes due to the second IR reflection is expressed as follows:

For the case of the HM control volume in Figure 4-4

$$\left(\dot{Q}_{IR,2ref,HM}\right)_{ml} = \left(1-\rho_{HM_{ml}}\right)\times\rho_{ab}\sum_{\substack{k=\left(\frac{m}{2}\right)+H \\ ,H=0}}^{H=N_R} F_{A_{k,l}HM_{m,l}}\left(\dot{Q}_{IR,1ref}\right)_{k,l} + \left(1-\rho_{HM_{ml}}\right)\times\rho_{ab}\sum_{\substack{k=\left(\frac{m}{2}\right)-H \\ ,H=1}}^{H=N_L} F_{A_{k,l}HM_{m,l}}\left(\dot{Q}_{IR,1ref}\right)_{k,l} \quad (4.5)$$

For the case of the HM control volume in Figure 4-5

$$\left(\dot{Q}_{IR,2ref,HM}\right)_{ml} = \left(1-\rho_{HM_{ml}}\right)\times\rho_{ab}\sum_{\substack{k=\left(\frac{m}{2}\right)+H \\ ,H=1}}^{H=N_R} F_{A_{k,l}HM_{m,l}}\left(\dot{Q}_{IR,1ref}\right)_{k,l} + \left(1-\rho_{HM_{ml}}\right)\times\rho_{ab}\sum_{\substack{k=\left(\frac{m}{2}\right)-H \\ ,H=1}}^{H=N_L} F_{A_{k,l}HM_{m,l}}\left(\dot{Q}_{IR,1ref}\right)_{k,l} \quad (4.6)$$

# Chapter 5 : Description of experiments and the adaptation of the theoretical model for the receiver unit operating indoor

## 5.1 Introduction

Measuring the heat losses of the receiver unit of the Parabolic Trough Collector (PTC) is an important aspect in order to measure the effectiveness and behavior at various ranges of Heat Transfer Fluid (HTF) temperatures. The output energy of the PTC depends on the HTF temperature, and the amount of HTF delivered. The heat losses lead to a decrease in the outlet temperature for constant mass flow rate. Maintaining the HTF temperature to reach the baseline value that is required by the power plant will lead to a decrease in mass flow rate, and power production [82]. The effect of reducing either the mass flow rate or the temperature of the HTF is that the plant performance deteriorates significantly. This chapter aims to study different receiver units by measuring their heat losses experimentally and validating the simulation codes based on the developed theory. The objectives of the experimental part of this chapter are to measure the heat losses of the bare design as a reference to compare the efficiency of a receiver unit with a hot mirror coating over the glass cover and our the cavity design that was discussed in the previous chapters.

## 5.2 Experiment setup description for the conventional receiver unit without coating "bare" and with hot mirror coating over the glass cover

The receiver unit was tested indoors. The length of the unit was 2.7 m at 25 ℃. It consisted of a mild steel absorber pipe of outer/inner diameter of 3.2/2.8 cm and joined pieces of Pyrex glass of cover outer/inner diameter of 5.8/5.4 cm with a length of 1.35 m each (see Figure 5-1 and Figure 5-2). Two such pieces were joined to give a total receiver unit of length 2.70 m. The Pyrex glass pieces were joined with a brass section in the center of the Absorber Pipe (AP). The central brass piece, glass cover, and the absorber pipe were vacuum insulated using flame-resistant high-temperature silicon. The annulus space was evacuated using an Alcatel vacuum pump (Dual stage rotary vacuum pump input: 208-230VAC, 60/50HZ). The high-temperature silicone also provided some degree of thermal contact insulation.



Figure 5-1: The receiver unit set up in the laboratory, behind a PERSPEX safety shield, on the left. On right, top: the heating element. Right center: vacuum pump (left) and variac, and temperature logging unit below.

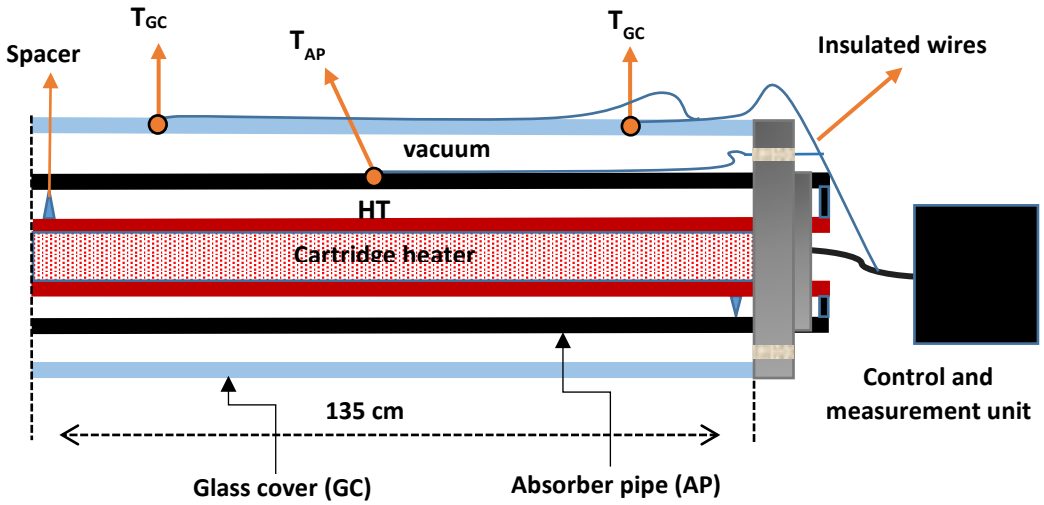



Figure 5-2: The right one-half of receiver unit. T represents the thermocouple position.

Two heating elements (1.5k W tubular element, outer diameter 8 mm and length 1172 mm, see Figure 5-1) inside the absorber pipe of the receiver unit brought the HTF temperature to the desired value. The heating element power was adjusted using a variac (Single phase variable transformer, input: 220 VAC 50 Hz Output: 0-5 kVAC and 20 A, see Figure 5-1) and was determined by logging the current and voltage output, with an error of ±7 W. The heating elements were both 1.2 m in length, with 8 mm (± 0.1 mm) outer diameter, cold resistance of 16 Ohm (±0.1 Ohm), and joined electrically inside the absorber pipe. In order to prevent the heating element from touching the absorber pipe, spacers were introduced to center the heating elements. The absorber pipe itself was filled with sand to mimic the presence of a heat transfer fluid and to distribute the heat evenly to the absorber pipe surface.

Five thermocouples (K-type thermocouples with a glass fiber twisted insulation, Nickel-Chromium alloy temperature range -200 ℃ to 1350 ℃) were mounted, two on the absorber pipe and three on the glass cover, to determine the average temperatures (±1K) and heating behavior of the receiver unit along its length. From the temperature information, the heat loss to the environment could be determined.

As indicated in Figure 5-2, the thermocouples wires were connected to the logging unit, which allowed regulation and adjustment of the heater power in accordance with temperature requirements, see temperature measurements in Appendix V.

The experimental procedure was initiated by evacuating the space between the absorber pipe and the glass cover, down to a pressure of < 0.1 mbar (measured with a KJL 275i series vacuum gauge), which is sufficient to greatly reduce convective heat transfer in that region [54]. The ambient temperature was noted. Next, a power setting on the variac was chosen, initially around 50 W. A more accurate estimate for the electrical power to the heating elements was determined subsequently using the voltage measurements with a Brymen TBM815 voltmeter (errors on V(AC) = 0.5% & Resistance = 0.1%) from the variac and the temperature-dependent resistance of the heating elements. The temperature measured by the thermocouples was noted using a dedicated microcontroller (Arduino Mega with thermocouple shield (MAX6675)) and displayed on a logging computer. The system was allowed to reach a thermal equilibrium, indicated by a stable reading of absorber pipe temperature. The time to reach

equilibrium could vary up to about three hours between measurements. Once equilibrium was reached, the temperatures were noted, and the variac setting was increased to the next higher power setting (typically 50 W higher). The experiment was terminated when the power input reached approximately 2kW, due to concerns of overheating of the vacuum system.

Table 5-1: List of different equipment/instrument used with error involved.

| **Equipment/Instrument** | | **Description** | **Error** |
|---|---|---|---|
| Temperature measurements | Microcontroller (Arduino) [120] | Board microcontroller with digital and analog input/output | Resolution 0.25 ℃ |
| | Thermocouple shield(MAX6675) [121] | Cold junction compensated K-thermocouple to digital converter chip | |
| | K-type thermocouples with a glass fiber twisted insulation | Nickel-Chromium alloy has a wide temperature range -200 ℃ to 1350 ℃ [122] | ± 1 ℃ |
| Multimeter for voltage and resistance measurements | | Brymen TBM815 | VAC (0.5%) & R (0.1%) |
| Tubular heating element | | 1.5kW tubular element, outer diameter 8mm and length 1172mm, | 2.5 W |
| Single-phase variable transformer | | Voltage regulator, input: 220VAC 50Hz Output: 0-5kVAC and 20A, | - |
| Alcatel vacuum pump | | Dual-stage rotary vacuum pump input:208-230VAC, 60/50HZ | - |
| Vacuum gauge | | KJL 275i series vacuum gauge | 10% accuracy within the measured region |

At equilibrium, the electrical power required to maintain the absorber pipe temperature equaled the heat loss of the receiver unit through the glass cover. The temperatures along the receiver unit elements were approximately similar to within a few degrees. Heat losses were reported as Power density (Watts per meter) of the receiver unit.

## 5.3 Experiment setup description for the proposed cavity design

The experiment setup for the proposed cavity design is similar to that mentioned in section 5.2, except some dimensions and materials were different. The length of the tested receiver unit was 3.9 m at 25 ℃. It consisted of three sections of mild steel pipes for the outer cover of the cavity receiver, each 1.3 m long with outer/inner diameter of 7.7/6.7 cm. Each section has an opening window along the length with a width of 1.8 cm. Borosilicate glass plates with 3.5 cm width and 0.38 cm thick were affixed on the outer cover aperture window using flame resistance high-temperature silicon. Inside the receiver unit is an absorber pipe with outer/inner diameter of 3.2/2.8 cm, see Figure 5-3. The connections between the various components were sealed using a heat resistant silicon sealant, which also provided some thermal contact insulation.



Figure 5-3: The receiver unit set up in the laboratory. The vacuum pipe can be seen connected to the center.

Three heating elements inside the absorber pipe of the receiver unit brought the fine sand inside of the absorber pipe to the desired test temperature. The heating element power was controlled by logging the current and voltage using a variac (see previous section). The heating elements were 1.2 m in length, with 8 mm outer diameter and total cold resistance of 11 Ohm.

Nine thermocouples were mounted (three on the AP, three on the outer cover, and three on the aperture window) to determine the average temperatures and heating behavior of the receiver along its' length, see Figure 5-4. The temperatures were measured using K-type thermocouples (Nickel-Chromium alloy temperature range -200 ℃ to 1350 ℃) with a glass fiber twisted insulation.

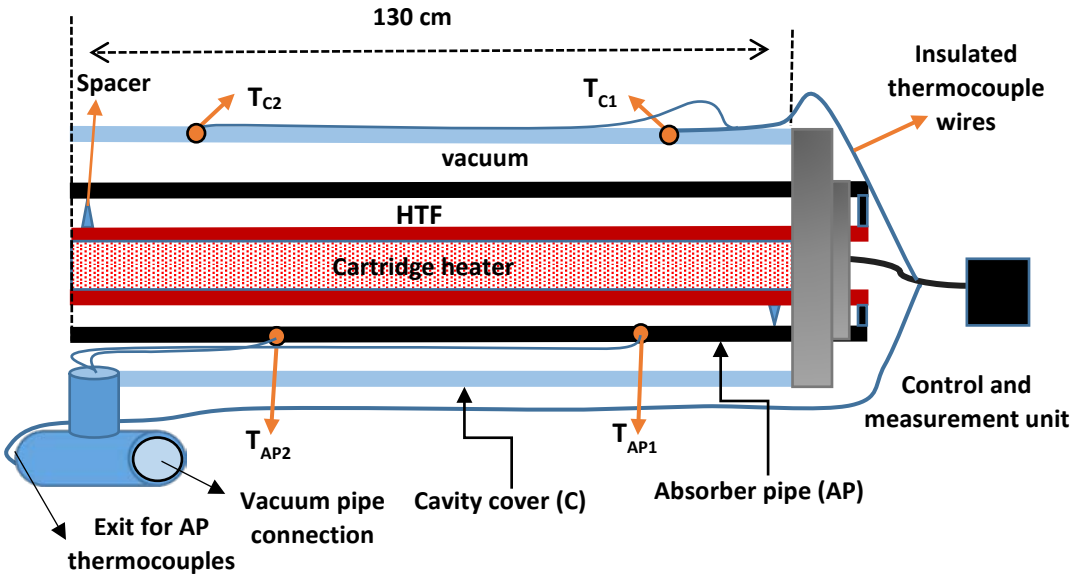



Figure 5-4: A section of the receiver unit. Cavity cover, absorber pipe (AP), spacers, heaters, wiring, and thermocouples are shown. "T" represents the thermocouple position.

The experimental procedure was similar to the one described in section 5.2. Once the receiver unit reached a steady-state temperature, the electrical power required to maintain the HTF temperature equaled the heat loss of the receiver unit at that temperature. The heat loss of the receiver unit was tested at different temperatures corresponding to different heating power settings from 50 W to 2 kW in roughly 50W increments. Heat losses were reported as Power density (Watts per meter) of receiver unit. For more details about the temperature measurements, see Appendix V.

## 5.4 Theory adaption for the indoor experiment

The source of the thermal energy used during the experiments was an electrical resistance heater wire with a rate of heat generation which was controlled by a variac. Figure 5-5 displays a quarter of the cross-sectional view displaying thermal interactions, which show slight differences when compared to Figure 3-1. The theoretical and the numerical model of the thermal interactions is the same as discussed in Chapter 3, 4 and 6 except for the following differences: the heat originates from the absorber pipe outer surface via the heating element inside. Consequently, there is no reason to consider the HTF in the calculations. Therefore, the convection heat transfer term $\left(\dot{Q}_{AF,conv}\right)$ and the incident solar radiation term $\left(\dot{Q}_{HM,sol}\right)_{ml}$. are removed from the previously derived energy balance equations. The term $\left(\dot{Q}_{AP,sol}\right)_{ml}$ becomes the heat-generating power of the heating element.

Under steady operating conditions, the absorber pipe and the outer cover (glass, HM or IRM) reach different stagnation temperatures. Moreover, the heat loss and the heat gain of each element in the receiver must equal the total rate of heat generation of the heating elements $\dot{E}_{gen}$

$$\dot{q}_{HM,amb} = \dot{q}_{HM,cond} = \dot{q}_{AP,HM} = \dot{q}_{HM,AP} = \dot{E}_{gen}, \tag{5.1}$$

where $\dot{q}_{HM,amb}$ is the rate of the heat transfer from the HM cover to the surroundings, $\dot{q}_{HM,cond}$ is the conduction through the HM layer, $\dot{q}_{AP,HM}$ is the heat transfer from AP to HM.

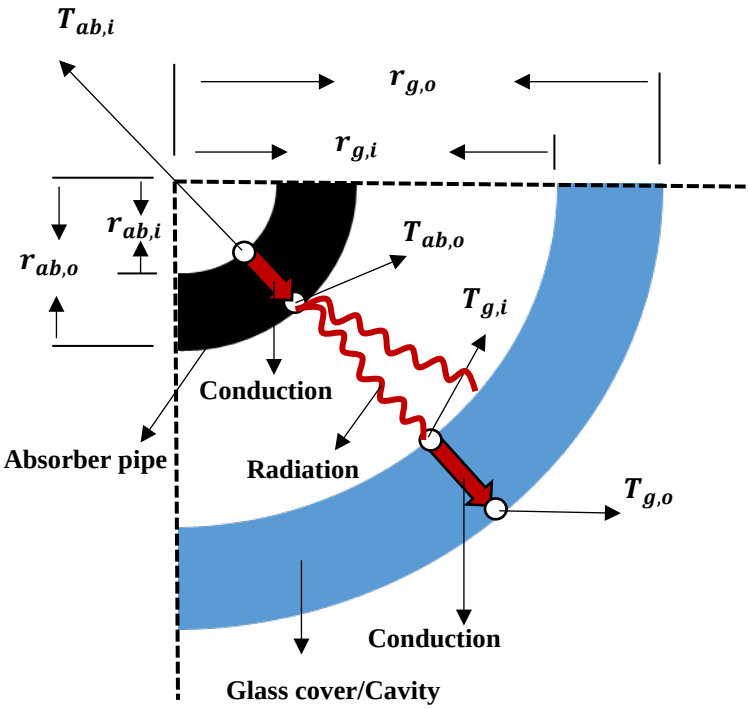



Figure 5-5: Receiver unit cross-section.

The calculations start from the heat loss to the ambient because the ambient temperature is known. We guess the unknown outer HM or glass cover surface temperature $T_{g,o}$ iteratively, until the steady operating condition at

which $\dot{q}_{HM,amb} = \dot{E}_{gen}$ is fulfilled. The heat rate $\dot{q}_{HM,amb}$ consists of natural convection and radiation heat transfer from the glass or HM cover to the ambient, as discussed in section 3.5. The air properties during the calculation were selected at $T_{avg} = \frac{T_{g,o}+T_{amb}}{2}$.

We can then evaluate $T_{g,i}$ at which the rate of heat loss due to the conduction through HM equals $\dot{E}_{gen}$. In the same way, $T_{ab,o}$ is evaluated through iteration until fulfilling $\dot{q}_{AP,HM} = \dot{E}_{gen}$, where $\dot{q}_{AP,HM}$ consists of the rate of the heat transfer between the AP and HM by convection and radiation. The convection heat transfer inside the evacuated annulus was ignored. The algorithm of solving the above mentioned is discussed in detail in Chapter 6.

# Chapter 6 : Numerical model and simulation implementation

## 6.1 Introduction

In this chapter, the numerical models and simulation algorithms of the parabolic trough collector receiver unit that operates with non-uniform (using solar radiation) and uniform (using heating element) heat fluxes are described. The simulations are implemented using Python code, see Appendix IV. The thermal processes were applied on control volumes as described in Chapter 3, including the reflection effects that were discussed in Chapter 4.

## 6.2 The numerical models of the parabolic trough receiver unit

### 6.2.1 The numerical model of the receiver unit that operates with non-uniform solar flux

Starting with the non-uniform concentrated solar irradiation distribution around the receiver unit, we used the predetermined profile of solar flux around the Absorber Pipe (AP) and the outer cavity surface by using Sheldon's formulation [123]. As we discussed in Chapter 3, the receiver unit was discretized into control volumes in the azimuthal and axial direction, and the HTF along the axial direction only. The Finite Volume Method (FVM) was used with the temperatures of each control volume. Energy conservation is applied on every control volume as follows

$$\left(\sum \dot{Q}_{Cond} + \sum \dot{Q}_{Rad} + \sum \dot{Q}_{Conv} + \sum \dot{Q}_{Sol}\right)_{ml} = 0. \tag{6.1}$$

According to Eq. (6.1), under steady-state conditions, the net heat flux due to convection $\dot{Q}_{Conv}$, radiation $\dot{Q}_{Rad}$, and conduction $\dot{Q}_{Cond}$, and the incident solar radiation $\dot{Q}_{Sol}$ sums to zero at any control volume in the receiver unit. The energy balance equation across AP control volume can be written with the use of the heat transfer equations ((3.2), (3.4) and (3.7), which were mentioned in Chapter 3, as follow

$$\dot{Q}_{A,\theta,m} + \dot{Q}_{A,r,m} + \dot{Q}_{AF,conv} + \Sigma\dot{Q}_{HM,A,IR} + \dot{Q}_{A,HM,IR} + \dot{Q}_{A,sol} = 0. \tag{6.2}$$

For the cavity, we call it Hot Mirror (HM) for simplicity. (Refer to the heat transfer equations and Figure 3-3 in Chapter 3) the energy balance equation at each HM CV is

$$\dot{Q}_{HM,\theta,m} + \dot{Q}_{HM,r,m} + \dot{Q}_{HM,O,conv} + \dot{Q}_{HM,O,IR} + \Sigma\dot{Q}_{HM,HM,IR} + \Sigma\dot{Q}_{A,HM,IR} + \dot{Q}_{HM,A,IR} + \Sigma\dot{Q}_{O,HM} + \dot{Q}_{HM,sol} = 0. \tag{6.3}$$

Eq. (6.2) and Eq. (6.3) resulted in a set of algebraic equations of fourth order where the heat fluxes and temperatures were coupled. According to Chapter 4, the number of HM control volumes is twice that of the AP control volumes. We chose HM control volumes number to be 200 and 100 for AP control volumes. This means that there are 200 equations for HM and 100 equation for the AP of the following form.

For the AP control volumes:

$$k_A \frac{-2T_{ml}^A + T_{m+1,l}^A + T_{m-1,l}^A}{\left(r_A + \frac{\Delta S_A}{2}\right)\theta_A} \Delta S_A \Delta L - h_f[r_A \theta_A \Delta L](T_{ml}^A - T_l^F) - R_{ml}^A$$
$$+ (1 - \rho_{A,sol})\tau_{HM_{ml}}(\dot{Q}_{A,sol})_{ml} + (1 - \rho_{A,IR}) \times \varepsilon\sigma \, dA_{HM} \sum_k F_{km}^{HM,A} \, T_{kl}^{HM^4} \quad (6.4)$$
$$+ (1 - \rho_{A,IR})\left((\dot{Q}_{IR,1ref})_{ml} + (\dot{Q}_{IR,2ref})_{ml}\right) = 0$$

For the HM control volumes:

$$k_{HM} \frac{-2T_{ml}^{HM} + T_{m+1,l}^{HM} + T_{m-1,l}^{HM}}{\left(r_{HM} + \frac{\Delta S_{HM}}{2}\right)\theta_{HM}} \Delta S_{HM} \Delta L - h_w[r_{HM} \theta_{HM} \Delta L](T_{ml}^{HM} - T^O) - R_{ml}^{HM}$$
$$+ (1 - \rho_{HM,sol} - \tau_{HM_{ml}})(\dot{Q}_{HM,sol})_{ml} - \varepsilon_{HM,out}\sigma \, dA_{HM}\left(T_{ml}^{HM^4} - T_{sky}^4\right)$$
$$+ (1 - \rho_{HM,IR})\left[(\Sigma \, F_{Km}^{HM,HM} \dot{Q}_{HM,HM,IR})_{ml} + (\Sigma \, F_{km}^{A,HM} \dot{Q}_{A,HM,IR})_{ml}\right. \quad (6.5)$$
$$\left. + (\Sigma \, F_{km}^{O,HM} \dot{Q}_{O,HM})_{ml}\right] + (1 - \rho_{HM,IR})\left((\dot{Q}_{IR,1ref,HM})_{ml} + (\dot{Q}_{IR,2ref,HM})_{ml}\right) = 0$$

Eq. (6.4) and Eq. (6.5) are a set of nonlinear equations which can be linearized via Taylor expansion. The linearized equations become [124]

$$a_m T_m = a_{m+1} T_{m+1} + a_{m-1} T_{m-1} + b_m, \quad (6.6)$$

where $T_m$, $a_m$, and $b_m$ are the temperature, the discretization coefficient, and the discretization source term of the control volume of interest, respectively. The remaining terms with index $m+1$ and $m-1$ describe neighboring control volumes. The coefficients in Eq. (6.6) are defined as follows:

For absorber pipe (AP):

$$a_m = k_A \frac{2 \times \Delta S_A \Delta L}{\left(r_A + \frac{\Delta S_A}{2}\right)\theta_A} + h_f[r_A \theta_A \Delta L] + 4\varepsilon_A \sigma dA_A \times \left(1 + \rho_A \rho_{HM_{2m}} F_{2m,m}^{HM,A}\left(\sum_k F_{mk}^{A,HM} - F_{m,2m}^{A,HM}\right)\right) \times$$
$$T_{ml}^{A\,3} - (1 - \rho_A) \times (4\varepsilon_A \sigma dA_A) \times \left(\rho_{HM_{2m}} F_{2m,m}^{HM,A} + \rho_A \rho_{HM_{2m}}{}^2 F_{2m,m}^{HM,A^2}\right) T_{ml}^{A\,3}, \quad (6.7)$$

$$b_m = \alpha_{viis,A} \, \tau_{vis,HM} \, dA_A \left(\dot{Q}_{A,sol}\right)_m + h_f dA_A \, T_l^f + 3\varepsilon_A \sigma dA_A \times \left(1 + \rho_A \rho_{HM_{2m}} F_{2m,m}^{HM,A}\left(\sum_k F_{mk}^{A,HM} -\right.\right.$$
$$\left.\left. F_{m,2m}^{A,HM}\right)\right) \times T_{ml}^{A\,4} - (1 - \rho_A) \times (3\varepsilon_A \sigma dA_A) \times \left(\rho_{HM_{2m}} F_{2m,m}^{HM,A} + \rho_A \rho_{HM_{2m}}{}^2 F_{2m,m}^{HM,A^2}\right) T_{ml}^{A\,4} + \quad (6.8)$$
$$(1 - \rho_A) \times \left((\dot{Q}_{IR,1ref})_{ml} + (\dot{Q}_{IR,2ref})_m\right) + (1 - \rho_A) \times \varepsilon_{HM} \sigma dA_{HM} \sum_k F_{km}^{HM,A} \, T_{kl}^{HM^4},$$

$$a_{m+1} = a_{m-1} = \frac{\Delta S_A \Delta L}{\left(r_A + \frac{\Delta S_A}{2}\right)\theta_A}. \quad (6.9)$$

For hot or IR reflecting mirror (HM/IRM):

$$a_m = k_{HM}\frac{2\times\Delta S_{HM}\Delta L}{\left(r_{HM}+\frac{\Delta S_{HM}}{2}\right)\theta_{HM}} + h_w dA_{HM,out} + 4\sigma \times \left(\varepsilon_{HM,in} dA_{HM,in} + \varepsilon_{HM,out} dA_{HM,out}\right) T_{ml}^{HM\,3}, \tag{6.10}$$

$$\begin{aligned} b_m = {} & \alpha_{viis,HM}\, dA_{HM,out}\left(\dot{Q}_{HM,sol}\right)_m + h_w dA_{HM,out}\, T^O + 3\sigma \times \left(\varepsilon_{HM,in} dA_{HM,in} + \right. \\ & \left. \varepsilon_{HM,out} dA_{HM,out}\right) T_{ml}^{HM\,4} + \varepsilon_{HM,out}\sigma dA_{HM,out}\, T_{sky}^4 + \left(1-\rho_{HM_m}\right) \times \left(\left(\dot{Q}_{IR,1ref,HM}\right)_{ml} + \right. \\ & \left. \left(\dot{Q}_{IR,2ref,HM}\right)_{ml}\right) + \left(1-\rho_{HM_m}\right) \times \varepsilon_{HM}\sigma dA_{HM,out} \sum_k F_{km}^{HM,HM}\; T_{kl}^{HM\,4}, \end{aligned} \tag{6.11}$$

$$a_{m+1} = a_{m-1} = \frac{\Delta S_{HM}\Delta L}{\left(r_{HM}+\frac{\Delta S_{HM}}{2}\right)\theta_{HM}}. \tag{6.12}$$

Eq. (6.6) is a set of discretized equations (Eq. (6.7) to Eq. (6.12)), which are solved through an iterative process. In this process, the heat transfer fluid (HTF) temperature along the length is coupled with Eq. (6.6) and computed using energy conservation, where HTF control volume "*l*" undergoes a temperature change described by

$$\left(\dot{Q}_{AF,conv}\right)_l = \sum_{m=1}^{N_m} h_f dA_A (T_{ml}^A - T_l^F) = \dot{m} C_P (T_{l+1}^F - T_l^F). \tag{6.13}$$

where $\dot{m}$ and $C_P$ are the mass flow rate and the specific heat capacity of the HTF respectively. Eq. (6.13) is used after solving the Eq. (6.6), iteratively, which is required to find the value of the temperature of the next HTF control volume $T_{l+1}^F$. The algorithm and the solution process are described in section 6.3.

### 6.2.2 The numerical model of the receiver unit that operates with uniform heat flux

The source of the thermal energy is an electrical resistance heater with a rate of heat generation that can be modified by a variac, where the total rate of heat generation $\dot{E}_{gen} = V_{rms}^2/R$, where *R* and *V* are the resistance, in ohm, and root-mean-square voltage, in voltage, across the heating element terminals, respectively. The heating element is inserted inside the absorber pipe (AP). Under steady operating conditions, this setup has the following characteristics:

- The AP and the outer cover are isothermal.
- The HTF is not considered in our description.
- The heat loss and gain of each element in the receiver must equal the total rate of heat generation of the heating elements.

The theoretical model that was discussed in Chapter 3, Chapter 4 and section 5.4 can be used for this case, except for the following:

- There is no convection from AP to the HTF $\left(\dot{Q}_{AF,conv}\right)_l$ and the interception of solar radiation on outer cover control volume $\left(\dot{Q}_{HM,sol}\right)_{ml}$.
- The solar radiation on AP control volume $\left(\dot{Q}_{AP,sol}\right)_{ml}$ becomes the heat generating power of the heating element on the AP control volume.
- The simulation algorithm and outputs are different. It is discussed in section 6.3.2.

## 6.3 Simulation algorithm description

### 6.3.1 Simulation algorithm of the receiver unit that operates with non-uniform heat flux

The simulation algorithm of the receiver unit that operates with non-uniform heat flux proceeds as follows: the HTF enters the absorber pipe (AP) with a specified initial temperature $T_l^F$. For all AP and the outer cover control volumes (CVs), the initial temperature $T^*$ (HTF inlet temperature) is guessed. The program iterates $T^*$ by solving Eq. (6.6) for all the control volumes on AP and the outer cover ring and we obtain a new temperature $T$, which serves as the next guess for next $T^*$ until the convergence criterion, $\frac{T^{n+1}-T^n}{T^n} < 10^{-6}$ ($n$ denotes the n$^{th}$ iteration) is achieved. By knowing $T$ for each control volume, we can determine the heat transferred into the HTF using Eq. (6.13), and the obtained outlet temperature will serve as the entry temperature for the next "ring" section of control volume in the azimuthal direction. This process repeats itself for the entire length of the receiver, see Figure 6-1.

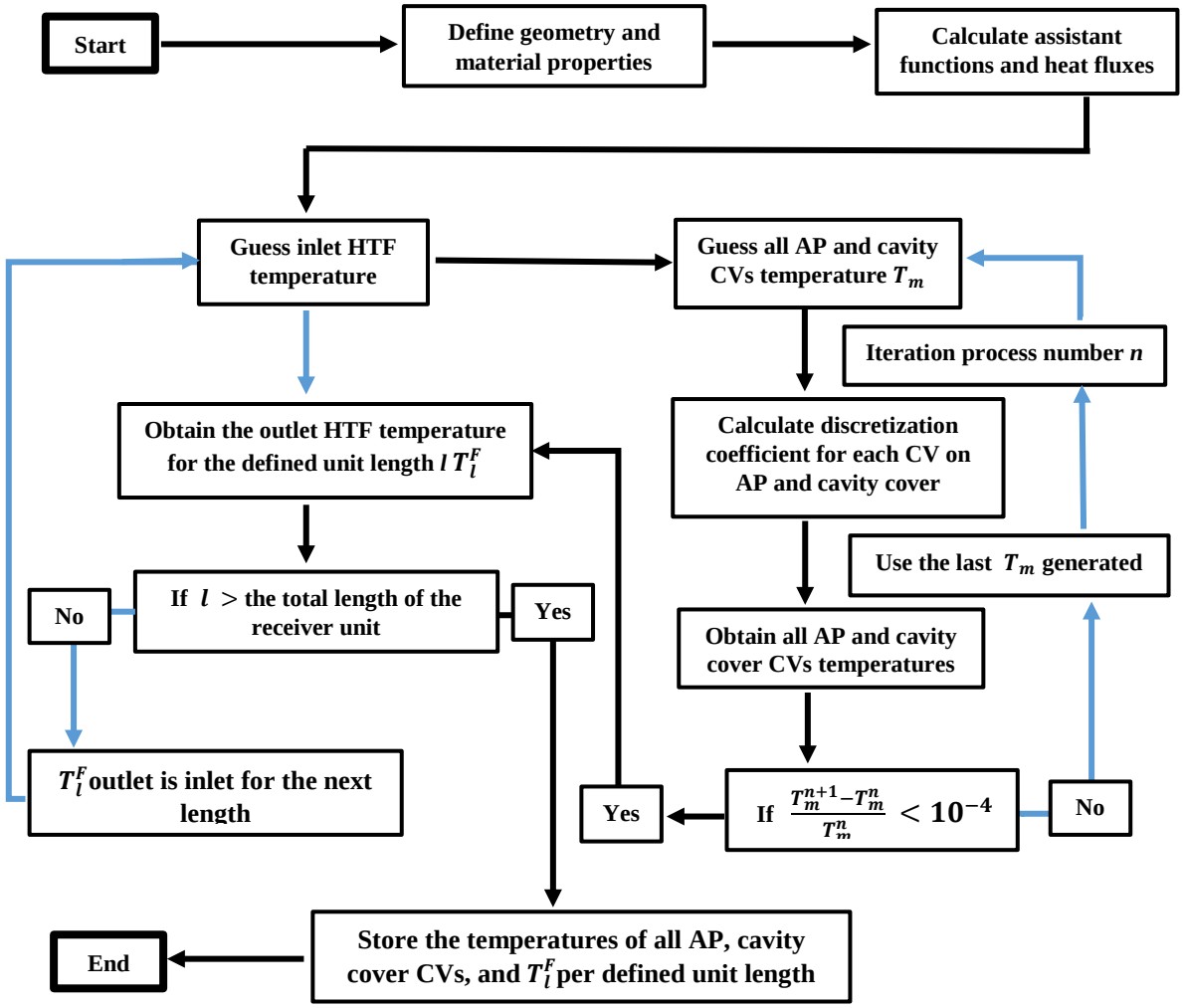



Figure 6-1: Illustration of the algorithm of the simulation code in case of the receiver that operates with non-uniform heat flux. Black arrows are for the primary processes execution and true conditions and the blue arrows, for the false and iterative conditions.

### 6.3.2 The simulation algorithm for the receiver unit that operates with uniform heat flux

This simulation differs from the previous case. The algorithm schematic is shown in Figure 6-2, and is summarized as follows: It starts by guessing the temperature of the outer cover control volumes (glass or HM + IRM) with a specified initial temperature $T_m^n$. It is an iterative solution until the heat loss of the outer cover to the ambient is equal to the heat power generation of the heating elements. By knowing the outer cover temperature, the inner temperature of the outer cover control volumes (CVs) can be calculated through the conduction heat transfer between outer cover widths. At this point, all control volumes of the same surface are in thermal equilibrium, while the temperatures of different surfaces are different. Next, all AP control volumes obtain a guessed initial temperature $T^*$. The program iterates $T^*$ by solving Eq. (6.6) for all the control volumes on AP and we obtain a new temperature $T$, which serves as the next guess for next $T^*$ until the convergence criterion, $\frac{T^{n+1}-T^n}{T^n} < 10^{-4}$ ($n$ denotes the n$^{th}$ iteration) is achieved. This process repeats itself for the entire length of the receiver.

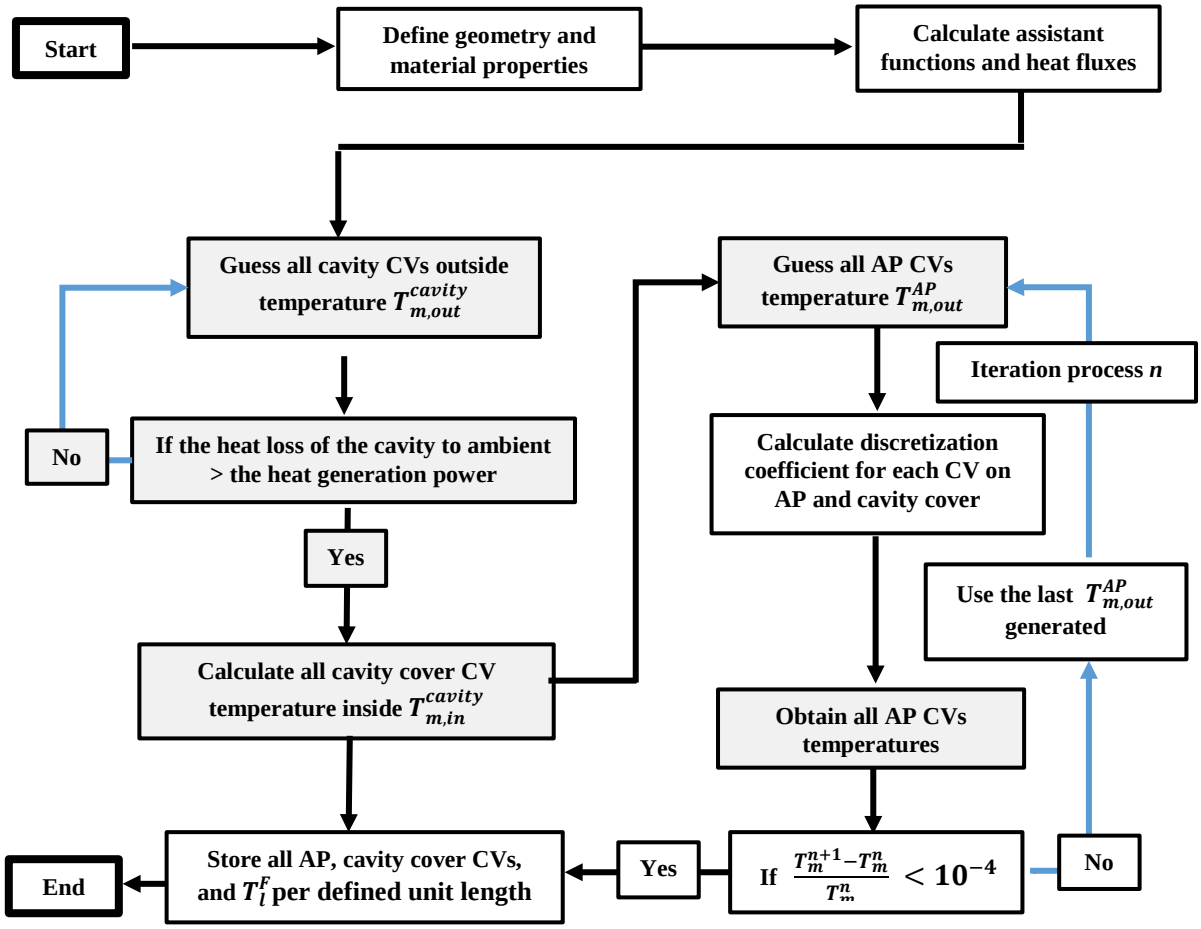



Figure 6-2: Illustration of the algorithm of the simulation code in case of the receiver unit that operates with uniform heat flux. Black arrows are for the primary processes execution and the true conditions and the blue arrows, for the false and iterative conditions. The colored blocks indicate a difference to the previous algorithm.

## 6.4 Simulation outputs and efficiency calculations

The simulations have the ability to provide numerical values of the thermal distribution of the HTF length and the circumference of both the absorber and the cover. It further details the heat losses resulting from the various mechanisms along the length. This information can be used to deduce the thermal efficiency of the system, i.e., efficiency to convert incoming solar radiation into the internal energy of the HTF.

Efficiency is calculated using the ratio of heat gain in the fluid to the total incident solar energy, which takes all the possible losses into account [125]. The efficiency for any control volume element is

$$\eta_{CV} = \frac{(\dot{q}_{AF,conv})_j}{(q_{sol})_j}, \tag{6.14}$$

where $q_{sol}$ the incident solar flux, and $(\dot{q}_{AF,conv})_j$ is defined by Eq. (6.13). The "integrated" receiver efficiency for some number *n* of control volumes along the system's length is

$$\eta = \frac{\sum_{j=1}^{n}(\dot{q}_{AF,conv})_j}{\sum_{j=1}^{n}(q_{sol})_j}. \quad (6.15)$$

In many applications, conversion to electricity is desired. The maximum "overall" efficiency $\eta_{max}$ of the solar plant and conversion to turbine work for electricity generation can be obtained using a theoretical Carnot Cycle for simplicity and comparison, which is given by

$$\eta_{max} = \frac{\sum_{j=1}^{n}(\dot{q}_{AF,conv})_j}{\sum_{j=1}^{n}(q_{sol})_j} \times \left(1 - \frac{T_{res}}{T_{HTF}}\right), \quad (6.16)$$

with $T_{res}$ as ambient used as the cold reservoir and $T_{HTF}$ as HTF temperatures, respectively.

# Chapter 7 : Results and discussion

## 7.1 Introduction

This chapter starts with convergence tests of the simulation codes to estimate the adequate numbers of control volumes and values for the convergence criterions. The simulation is then compared to experimental data. The simulation results of the proposed cavity design and the effects of changing the main cavity design parameters on the performance are illustrated. Lastly, the comparison between the proposed cavity design and the other alternatives is discussed.

Before we proceed with the simulation results, below is a list of assumptions used in the simulation:

- The flow is incompressible.
- The absorber pipe surface emits and reflects diffusely.
- Hot mirror (HM) and IR reflective mirror (IRM) are secularly reflective in the IR.
- Radiative fluxes are a surface phenomenon. The surfaces are so thin that absorption can be considered to occur on the surface.
- There is a linear temperature profile across the boundary surfaces of the consecutive control volume. A piecewise linear profile approximation enables linear interpolation functions to be used for surface temperatures.

## 7.2 Convergence tests

### 7.2.1 Grid dependency

As discussed in Chapter 3, the receiver unit is discretized into control volumes (CVs). The number of control volumes is directly related to the size of the control volume, which could influence the results for the surface temperatures. The size of the control volume along the circumference can be determined from the arc angle $\theta = \frac{2\times\pi}{N}$ and the radius of either absorber pipe or the outer cover. The study of the effect of the number of control volumes, "*N* ", on the results is illustrated in Figure 7-1.

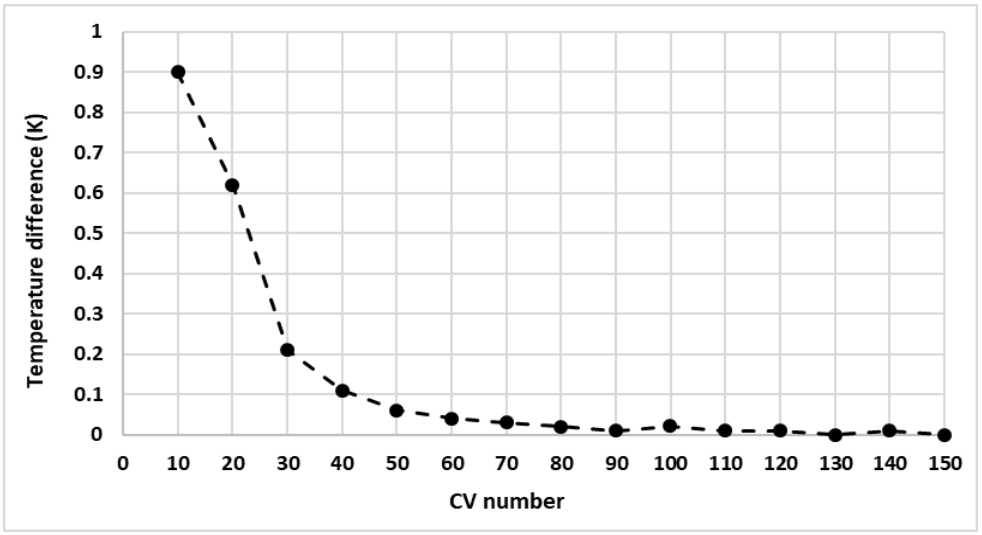



Figure 7-1: Convergence test of the control volumes (CVs) number to select the minimum number of CVs along the circumference.

The temperature difference in Figure 7-1 is between two successive total control volume (CVs) numbers. We chose 100 CVs along the circumference.

### 7.2.2 Convergence criterion

The iterative solutions that were discussed in chapter 6 and their summarized algorithms in Figure 6-1 and Figure 6-2 required Convergence Criterion (CC) values. The convergence test of the CC is to select the adequate value that gives the highest accuracy and the lowest computational efforts of the simulation results. In all test cases, the convergence test took place with different values of CCs, which ranged from 0.1 and decreased by the power of 10. There are two CCs for the two simulation codes (receiver unit operates with using uniform and non-uniform heat fluxes). For the uniform heat flux simulation code, we evaluated the CC twice for two different functions. In Figure 7-2 and Figure 7-3, the convergence tests of the CC values for the outer cover and the AP function at constant CC values for the AP and outer cover functions are respectively shown. It was found that the highest accuracy of the solution that is combined with the lowest computational efforts is at $10^{-3}$ (equivalent to the value 3 in X-axis) for both functions, where the X-axis values equal to $\log\frac{1}{CC}$.

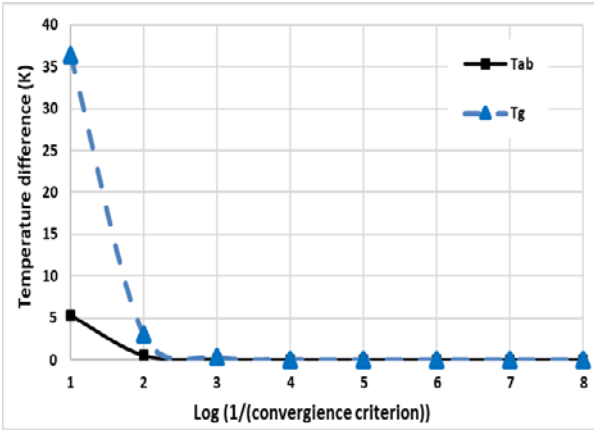



Figure 7-2: Convergence test at different convergence criterion values for the outer cover function.

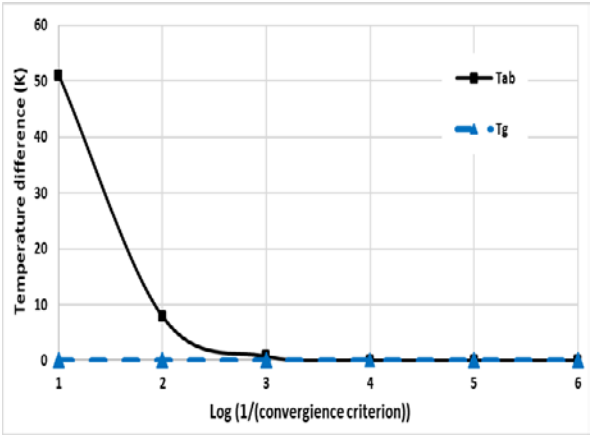



Figure 7-3: Convergence test at different convergence criterion values for the AP function.

Similarly, for the non-uniform heat flux simulation, the convergence tests of CC values for the AP and the outer cover functions were also performed. These tests are similar to the simulation code of uniform heat flux case, but because of the non-uniformity of the temperature distribution across the circumference, the tests were situated at different points on the circumference of the receiver unit, namely; at $0^{\circ}$, $90^{\circ}$, $180^{\circ}$, and $270^{\circ}$. The tests started with the CCs of the AP function because the simulation algorithm begins with the AP function, where the AP function results serve as the solutions to the outer cover function. Figure 7-4 shows the convergence test of the CC of the AP function at a constant CC value of the outer cover function and Figure 7-5 shows the inverse. The suitable amount value of the CC was found to be $10^{-5}$ (equivalent to the value 5 in X-axis) for both functions.

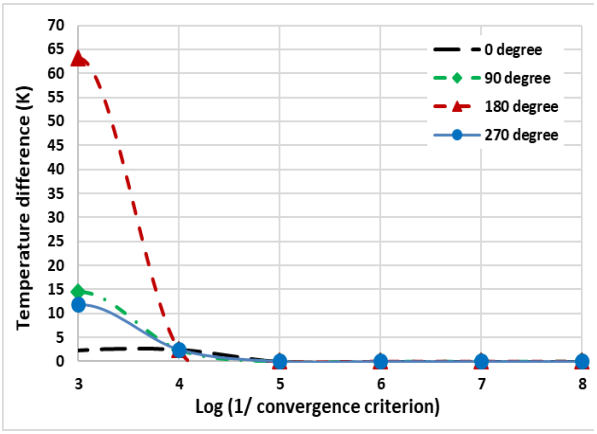



Figure 7-4: Convergence test at different values of the AP function CC for the simulation code of non-uniform solar flux case.

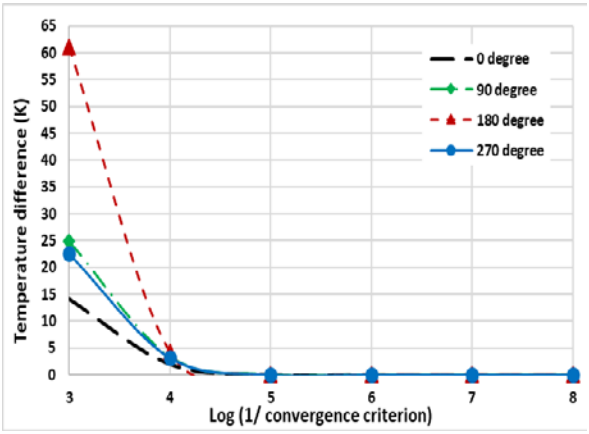



Figure 7-5: Convergence test at different values of the outer cover function CC the simulation code of non-uniform solar flux case.

## 7.3 Code validation

A simulation validation was undertaken using two approaches. Firstly, with a theoretical expectation method by setting some parameters of the PTC to known values, expecting known results. Secondly, by comparing both the simulation codes with the experiment results.

In the theoretical expectation method, we selected “special “ simulation parameters for physical scenarios where the outcomes could be derived by other means, such as: zero solar irradiation (the result was for the receiver unit

to approach ambient temperature regardless of its initial temperature); zero absorber material conductivity (no heat was transferred between adjacent control volume elements, and the thermal spectrum was identical to the solar spectral input) and zero HTF convective heat transfer (no HTF temperature variation was seen). The results that conformed to theoretical and intuitive expectations are shown in Figure 7-6 and Figure 7-7.

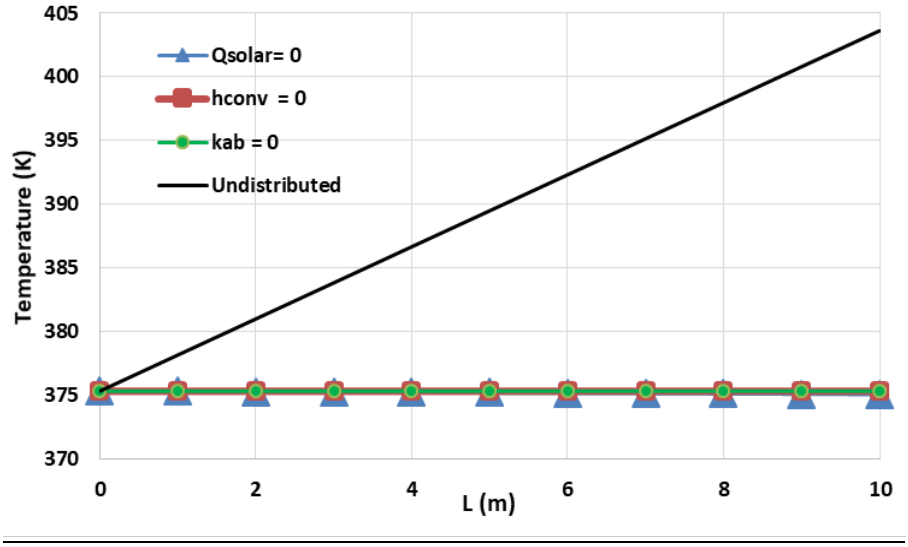



Figure 7-6: Heat transefer fluid (HTF) temperature at zero value of solar irradiation, absorber material conductivity, and HTF convective heat transfer coefficient.

In Figure 7-6, *Qsolar* is the solar irradiation, *hconv* is the Heat Transfer Fluid (HTF) convective heat transfer, *kab* is the absorber pipe thermal conductivity and "*Undistributed*" is the receiver unit that operates with the physical parameters in Table 7-1. The HTF temperature is not expected to rise in temperature for any of the scenarios. In Figure 7-7, the effect of cutting off the emissivity of the absorber pipe on the absorber pipe surface temperature at different angular positions (the angle 180° points directly away from the sun and towards the center of the parabolic mirror) at different receiver lengths is notably high.

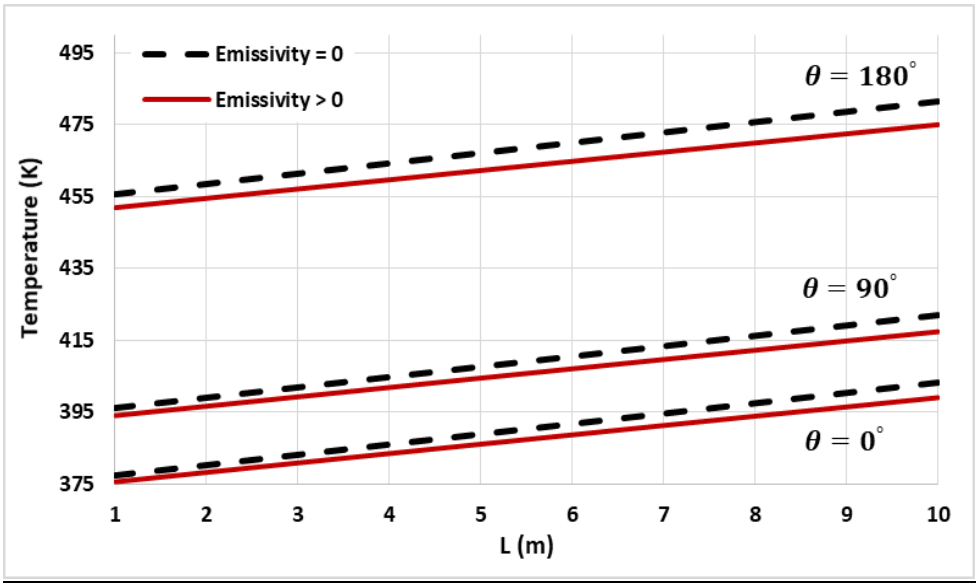



Figure 7-7: The absorber pipe surface temperatures at zero emissivity of the absorber pipe.

### 7.3.1 Experimental validation of the simulation code with non-uniform heat flux

Our simulation was compared with existing experimental data for a selective coating. The model was used to reproduce results for the PTC operating condition and parameters, which was modeled by Hachich [111] and related experimental data collected by Dudley et al. [32]. The operating conditions and design parameters that were used were chosen to simulate the SEGS (Solar Electric Generating System) LS2, which is one of parabolic troughs installed in the nine SEGS power plants in California [32]. The simulation parameters are shown in Table 7-1.

Table 7-1: Design parameters of the SEGS LS2 used in our simulation.

| ***Parameter*** | ***Value*** |
|---|---|
| *Collector aperture (W)* | 5 m |
| *Focal distance (f)* | 1.84 m |
| *Absorber internal diameter* | 0.066 m |
| *Absorber external diameter* | 0.07 m |
| *Absorber emissivity (IR)* | 0.15 |
| *Glass internal diameter* | 0.109 m |
| *Glass external diameter* | 0.115 m |
| *Glass emissivity (IR)* | 0.86 |
| *Receiver absorptance (visible)* | 0.96 |
| *Glass transmittance (visible)* | 0.93 |
| *Parabola specular reflectance* | 0.93 |
| *Incident angle* | 0.0 |
| *Solar irradiance* | 933.7 $W/m^2$ |
| *HTF* | Molten salt |

| | |
|---|---|
| *Mass flow rate* | 0.68 kg/s |
| *Temperature HTF (inlet)* | 375.35 K |
| *Temperature ambient* | 294.35 K |
| *Wind speed* | 2.6 m/ s |

The results in Figure 7-8 show the temperature variation along the axial direction for a receiver length of 8 meters at three different angular positions, for the present work and the work in [111]. The results have similar trends with a maximum difference of less than 1%. The temperature positions are at $0^{\circ}$, which points directly towards the sun, and at $180^{\circ}$, which points directly to the centerline of the parabolic mirror.

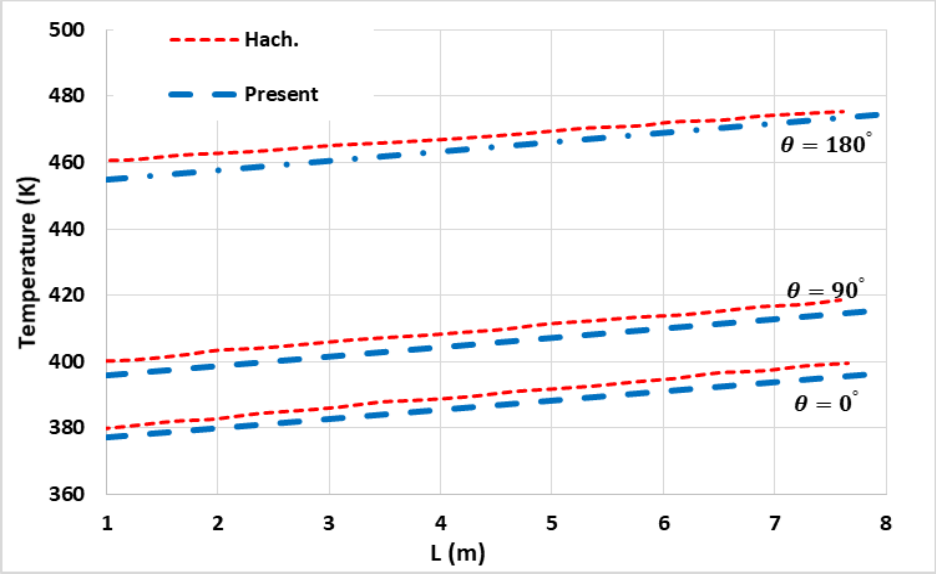



Figure 7-8: Temperature variation along the axial direction at different positions across the circumference of the AP.

In Figure 7-9 and Figure 7-10, the temperature profile of the AP circumference is obtained and compared with the work conducted by Hachicha et al. [111] at 6 m and 8 m of the receiver section. Both figures show that the maximum temperature difference is approximately around 80 K, as well as the maximum discrepancy between the present work and the work by Hachicha et al. [111] was less than 0.9%.

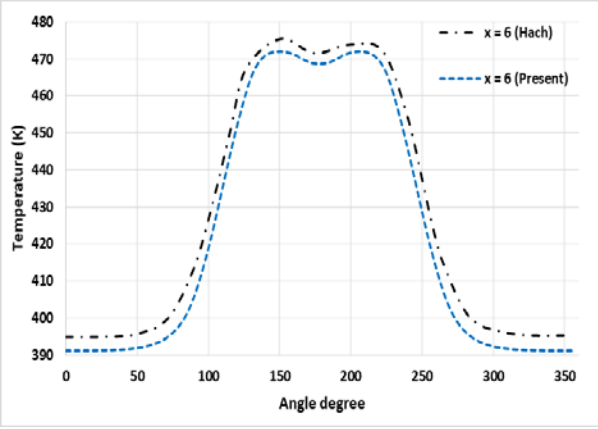



Figure 7-9: Temperature profile around the AP circumference at 6 m length.

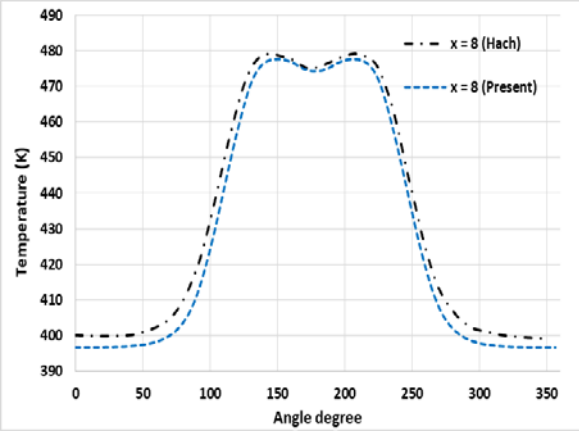



Figure 7-10: Temperature profile around the AP circumference at 8 m length.

Figure 7-11 presents the glass cover (GC) temperature profile around the circumference at a distance of 4 m, comparing our simulated results with the work in [111]. The maximum variation of the temperature across the circumference between the region that faces the parabolic mirror and the other region that faces the sky varies by approximately 40 ℃. It is lower than the corresponding AP temperature. The discrepancy between the present work and Hachicha et al. [111] was found to be about 0.7 % (maximum discrepancy at $0^{\circ}$and $145^{\circ}$).

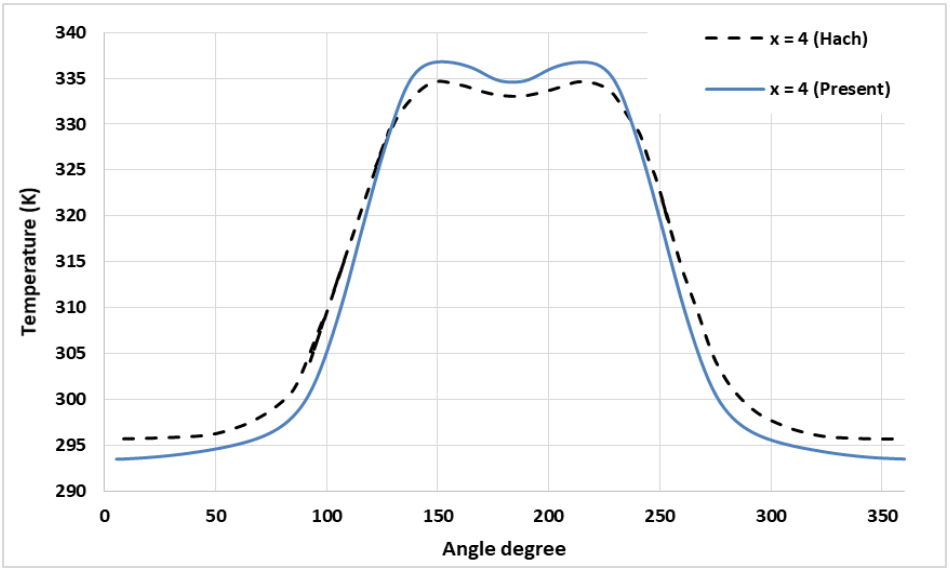



Figure 7-11: Temperature profile around the GC circumference at 4 m length.

### 7.3.2 Experimental validation of the simulation code with uniform heat flux

Three experiments were performed and the data was compared to the simulation. The first was to use the system in section 5.2, Chapter 5 and contained no coating on either the glass cover or the absorber pipe, and is designated the name "Bare". This system was investigated because it is the simplest scenario, so any applied coating should perform better in order to be considered. It provided an additional check on our simulation and allowed us to make fine adjustments to the experimental procedure.

The second experiment used a “hot mirror” coating on the glass cover. In the first attempt, a plastic-based, transparent material coated with ITO was used, similar to the material utilized as a hot mirror for house windows

for interior climate control management. It was not rated for the temperatures experienced inside the receiver unit, hence deformed and partially melted. Subsequently, a thin, aluminum-based metal sheet with an IR reflectivity of approximately 0.92 was used (obtained from the MIRO SUN Alanod Solar Company datasheet). The sheet is not transparent to solar radiation. However, this was immaterial, since, in the experiment, the effects of IR reflectivity were tested, not of solar transparency (which was, in any case, absent in our simulation). The sheet served to mimic the effects of a hot mirror system.

The third experiment used a cavity receiver design that was mention in section 5.3. The optical properties of the receiver unit components for the three experimental set ups are presented in Table 7-2.

The main point of the experiments was to validate the theory and the simulation, with particular emphasis on the IR reflection component that was derived in Chapter 4, and the validation must hold for any simulations values.

Table 7-2: Optical properties of the absorber pipe and outer cover of the receiver unit at different scenarios [64][32][29].

| | | **Absorber pipe** | **Glass cover** | **Hot mirror (ITO)** | **IR mirror cavity** |
|---|---|---|---|---|---|
| **Visible** | **Transmissivity** | 0 | 0.935 | 0.875 | 0 |
| | **Reflectivity** | 0.14 | 0.04 | 0.1 | 0.92 |
| **IR** | **Transmissivity** | 0 | 0 | 0 | 0 |
| | **Reflectivity** | 0.14 | 0.14 | 0.85 | 0.92 |

#### 7.3.2.1 The “bare” receiver unit

The experimental procedure and the dimensions of the “bare” receiver unit were mentioned in section 5.2, and the optical parameters are shown in Table 7-2. The results of the “bare” pipe experiment are displayed in Figure 7-12. The power density is displayed on the vertical axis, in units of watts per meter, and the measured and simulated temperatures are displayed on the horizontal axis, in units of degrees Celsius. Both the experimental results (EXP) and the results from the simulation (SIM) are displayed.

Chi-squared goodness of fit gives p-values of > 0.99 for the glass cover and > 0.995 for the absorber pipe.

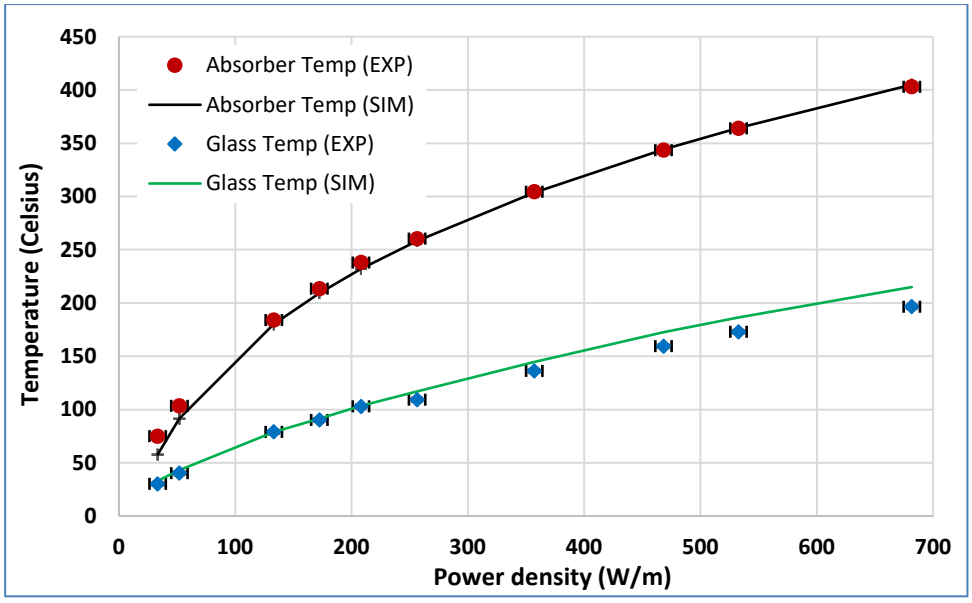



Figure 7-12: Experimental and simulated results for the temperature profile at different heating powers for the receiver unit without any coating, designated "bare".

### 7.3.2.2 The receiver unit with “hot mirror” coating

The dimensions of the receiver unit with “hot mirror” coating and the experimental procedure were indicated in section 5.2, and the optical parameters are shown in Table 7-2. The results of the experiment and the simulation are displayed in Figure 7-13.The axes display the same units as for the "bare" case. It is seen that the experimental (EXP) and simulated (SIM) results for the glass cover diverge at most by 3%, while those of the absorber pipe by at most 6% at around 500 ℃, where the simulation underestimates the temperature.

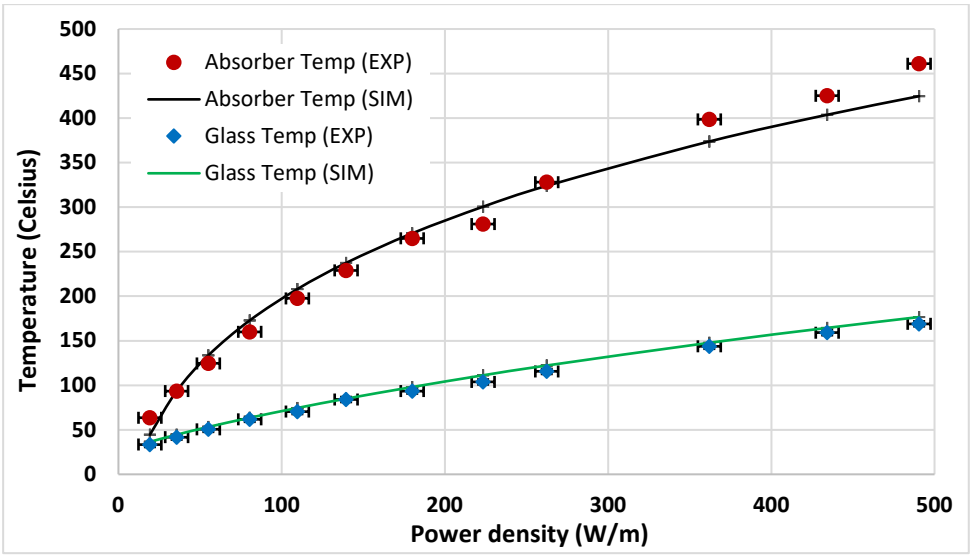



Figure 7-13: Simulated and experimental results of the receiver unit coated with a hot mirror at various temperatures

A Chi-squared gives p-values of >0.995 for the glass cover. For the absorber pipe, a p-value of >0.80 was obtained, and the point at 44ºC was considered an outlier, so only 10 degrees of freedom were included. The main contribution for the divergence comes from high-temperature points, but the simulation underestimates

experimental performance. This divergence is likely due to temperature-dependent simulation parameters and can be addressed in a more accurate model.

The effect of the coating can be seen in Figure 7-14, where the experimental data from the bare pipe and the hot mirror coated pipe are displayed.

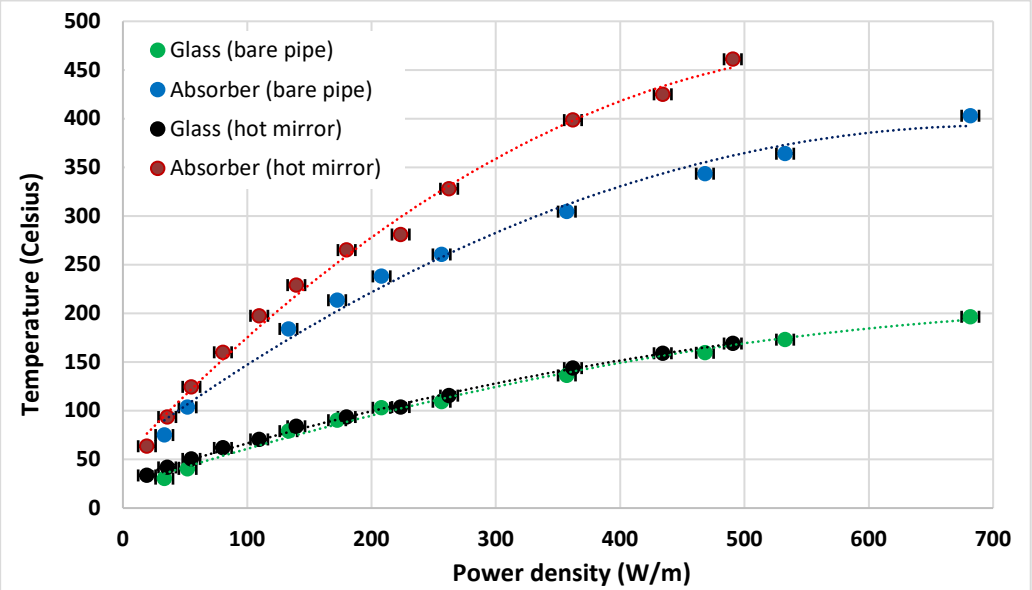



Figure 7-14: Comparison between experimental results from the bare and hot mirror receiver. The hot mirror absorber pipe is capable of reaching much higher temperatures at the same power input.

The absorber pipe in the IR reflected mirror (hot mirror) case is significantly hotter, indicating better thermal retention, and would, therefore, have a better capability of heating the heat transfer fluid inside to high temperatures. The glass temperature in both cases is similar, as expected.

#### 7.3.2.3 The receiver unit with a cavity design

We conducted our proposed design experimentally (indoors) to collect more evidence to validate our theoretical description, and simulation based on it, for different receiver designs, especially for the IR reflecting model that was discussed in Chapter 4. The experiment setup description for the cavity receiver and the cavity dimensions were mentioned in section 5.3 and the optical parameters of this receiver are shown in Table 7-2. In Figure 7-15, the axes display the same units as for the “bare” and “hot mirror” cases. Both the experimental results (EXP) and the results from the simulation (SIM) are displayed. It is seen from Figure 7-15 that the EXP and SIM results for the cavity cover diverge at most 0.9%, while those of the absorber pipe diverge at most 6% at around 500 Celsius. A Chi-squared goodness of fit gives p-values of > 0.95 for the cavity cover and p-value of >0.8 for the absorber pipe.

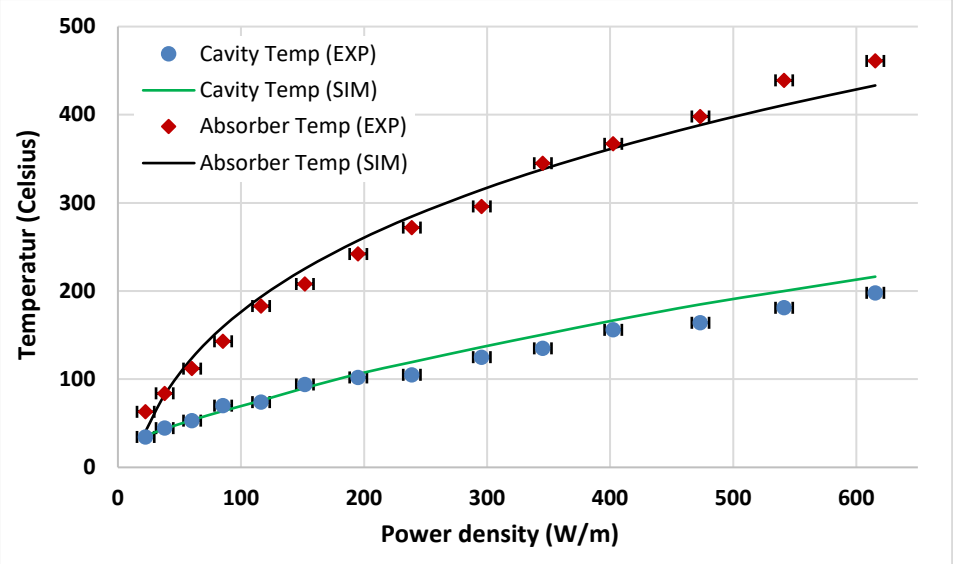



Figure 7-15: Experimental and simulated results of the temperature profile at different heating powers for the cavity receiver unit

## 7.4 The proposed Cavity design results

In section 7.3, the simulation codes were validated with experimental results. The simulation codes can now be utilized to study the proposed cavity receiver design with a hot mirror application, as well as alternative receiver designs with different active layer applications. The operating conditions and design parameters used in the simulation are similar to the condition at the SEGS power plants, see Table 7-1. However, the optical parameters were modified to fit the cavity requirements. The modifications are mentioned in Table 7-2.

### 7.4.1 The effect of the different cavity opening sizes on the HTF temperature and the system efficiency

The cavity opening, or aperture, is the only radiation entry point of the receiver for concentrated solar radiation. Its dimensions have a strong effect on the system. The focal line has a minimum width relative to the mirror size, which is dictated by the angular sun size [126], and the minimum aperture size must be larger than the focal line width if all the concentrated radiation is to be captured by the receiver. On this basis, the minimum arc length of the aperture was chosen as 48 mm (Appendix III) for the design parameters of Table 7-1.

Subsequently, our simulation is used to study the effect of aperture size on efficiency and the HTF temperature using four different cavity opening sizes, see Figure 7-16. Their arc lengths are 180 mm, 126 mm, 90 mm, and 54 mm which are respectively equivalent to the lengths of 100, 70, 50 and 30 control volumes. The calculations that relate the sizes of different aperture widths and their corresponding control volumes number are mentioned in Appendix III.

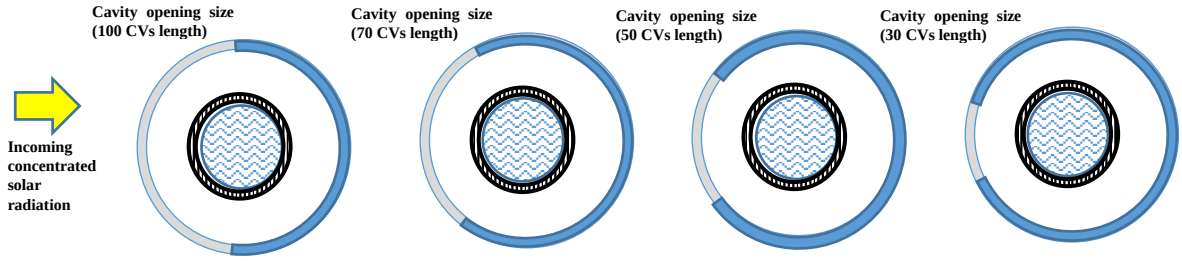



Figure 7-16: Cross-section of the cavity design with different cavity opening sizes

In Figure 7-17, the axial temperature variation for the HTF is plotted along the receiver length, for HTF inlet temperatures of 375 K. Temperature increases roughly linearly and then flattens out to approach the stagnation temperature, where solar energy input equals IR losses. The smallest cavity opening reaches the highest temperature since the solar input is similar for each cavity, but IR losses are related to aperture size. The maximum HTF temperature for this design rises close to 1300 K at 100 control volume (CVs) and 1490 K at 30 CVs.

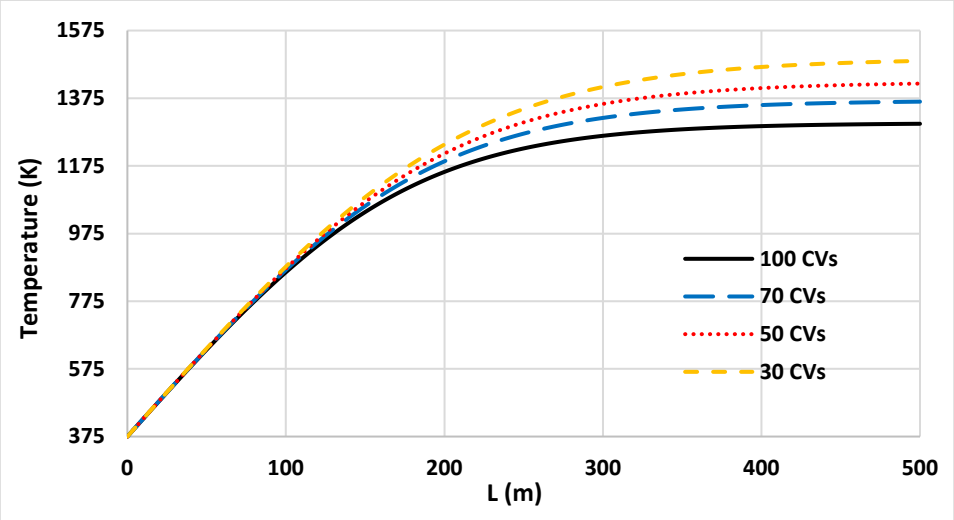



Figure 7-17: HTF temperature as a function of the length of the receiver unit with different cavity opening sizes

In Figure 7-18, the integrated efficiency (section 6.4, Eq. (6.15)) is displayed, which is the ratio between the aggregate concentrated solar radiation incident on the receiver up to length L and the total heat transferred into the HTF at length L. It represents the fraction of solar energy converted into thermal energy at length L.

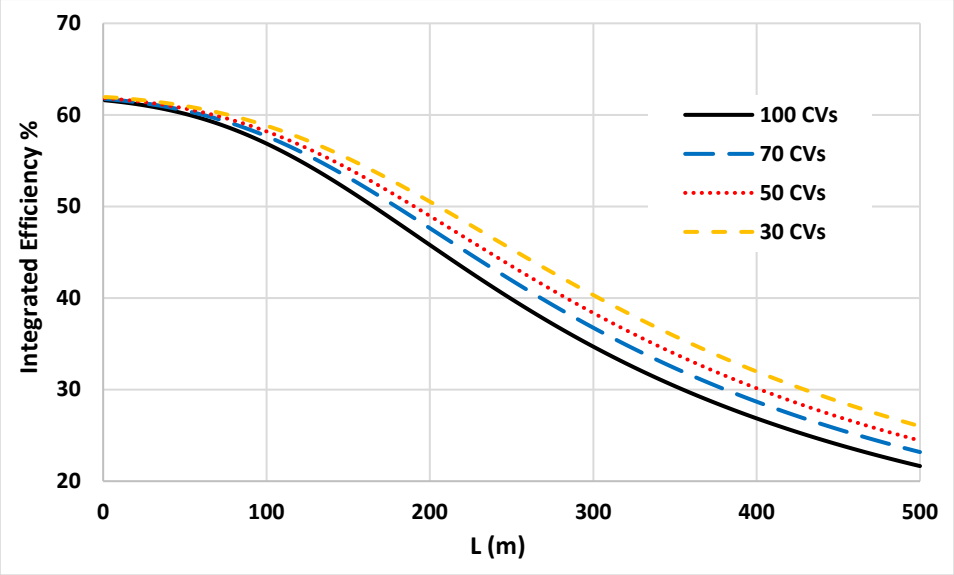



Figure 7-18: Efficiency of the parabolic trough collector with the cavity design of the receiver unit.

The cavity design reduces radiation losses, but some fraction of radiation still escapes. This escaping, "lost" energy grows rapidly at higher temperatures, since radiation losses are proportional to the fourth power of temperature. Eventually, the "lost" energy will become equal to the solar input energy, and both the temperature of all aspects of the receiver unit, as well as the efficiency, will no longer vary.

The integrated efficiency of the parabolic trough collector with the cavity design improves with smaller aperture sizes, as shown in Figure 7-18.

### 7.4.2 Effect of the reflectivity of the cavity mirror on the HTF temperature and the system efficiency

The cavity design aims to reflect the thermal IR radiation onto the absorber without much loss. This identifies the reflectivity of the cavity inner surface (mirror) as a significant parameter in the design. Its effects on system efficiency and HTF temperature are discussed next using three different IR reflectivities, 92%, 95%, and 98%, at cavity opening size = 54 mm (30 CVs).

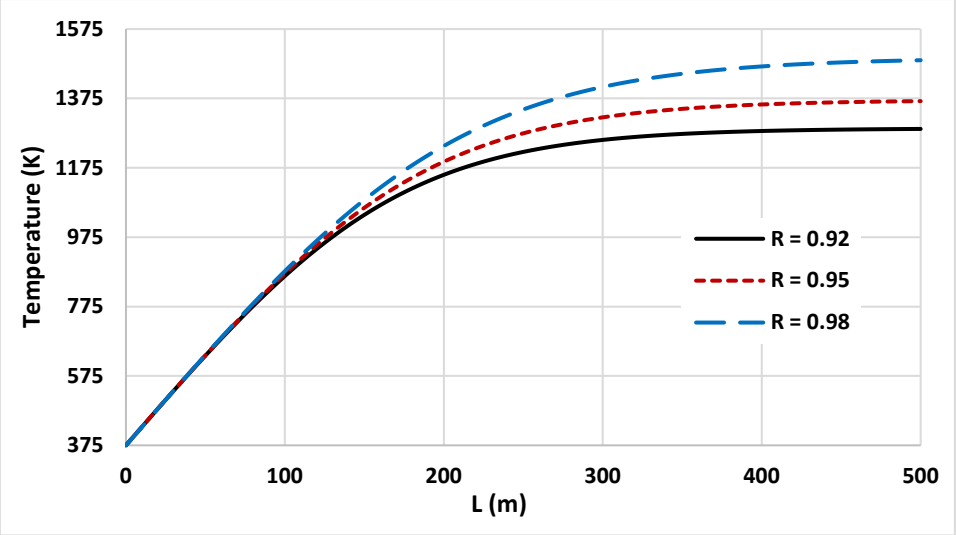



Figure 7-19: HTF temperature as a function of the length of the receiver with different cavity mirror reflectivity.

Figure 7-19 shows the effect of the reflectivity (R) of the cavity mirror. Although the difference is small at temperatures below ~800K, it is seen that even a 3% increase in reflectivity can have a ~100K increase in stagnation temperature. The maximum HTF temperature for this design reaches approximately 1293 K at R=92%, 1384 K at R=95%, and 1525 K at R=98%.

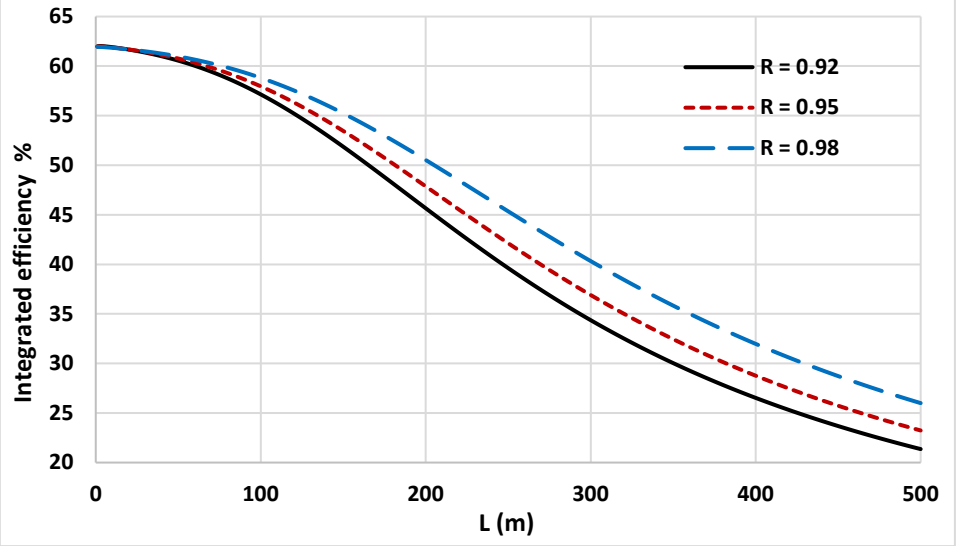



Figure 7-20: Efficiency of the parabolic trough collector with different cavity mirror reflectivity.

The reflectivity of the cavity mirror has a definite impact on efficiency as is shown in Figure 7-20. Intuitively, a very reflective inner cavity surface does not absorb radiation much, and therefore will not heat itself very much and impart heat to the outside via convection and radiation.

### 7.4.3 The role of the hot mirror coating over the cavity opening

The cavity opening is the only place where large amounts of thermal radiation can escape the cavity. One way of reducing this loss is to coat the inside of the aperture glass cover with a hot mirror coating. A further effect is a temperature reduction of the glass, which minimizes thermal stresses. The receiver was simulated with (W) and

without (WO) hot mirror coating over the cavity opening at the cavity mirror reflectivity equals R= 98%, and the cavity opening size equals 54 mm.

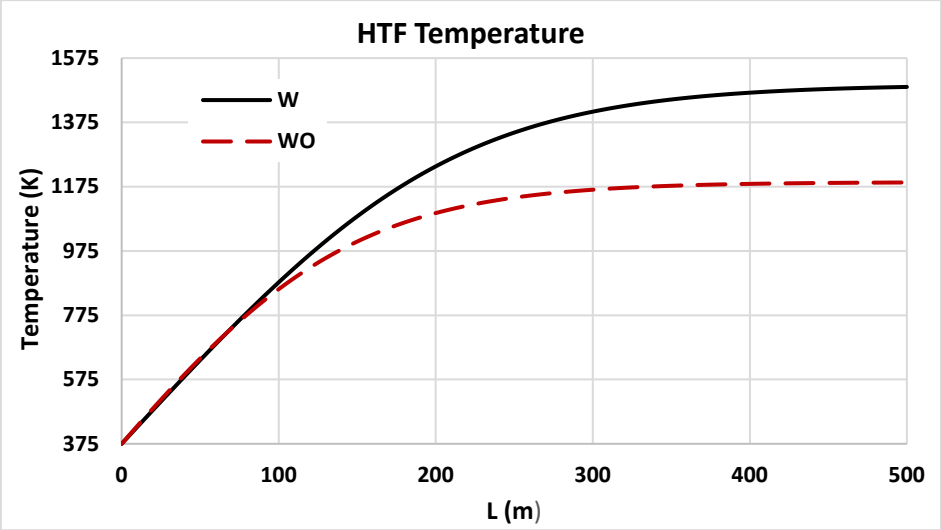



Figure 7-21: HTF temperature as a function of the length of the receiver with a hot mirror coating and without over the cavity opening.

Figure 7-21 shows that the aperture hot mirror coating has a strong influence on the HTF temperature at higher temperatures. Stagnation temperature varies between ~ 1271 K without a hot mirror and ~1525 K with hot mirror coating. Figure 7-22 indicates lower efficiency for a coated aperture up to some temperature (~650K) but an improved efficiency after that. This can be explained as follows: the hot mirror coating reflects a small IR portion of the solar spectrum, and therefore, less solar radiation is incident on the receiver. At higher temperatures, this negative effect is compensated for by the reduced heat losses due to the hot mirror coating reflecting IR back into the cavity.

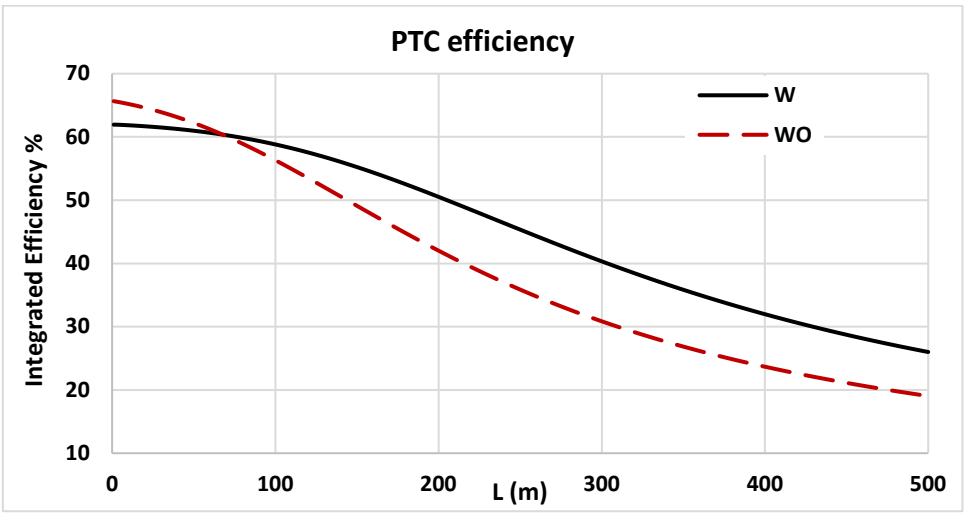



Figure 7-22: Efficiency of the parabolic trough collector with and without hot mirror coating over the cavity opening.

In addition, the glass cover on the cavity opening is exposed to thermal stresses at higher temperatures, which can be mitigated with a hot mirror coating.

The temperature distribution around the circumference of the cavity at two lengths (100m and 200m) indicates how the hot mirror behaves at different temperatures.

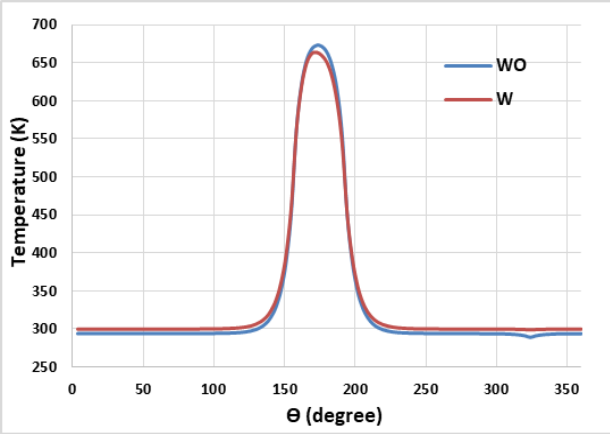



Figure 7-23: The surface temperature of the outer surface of the cavity receiver at length 100 m.

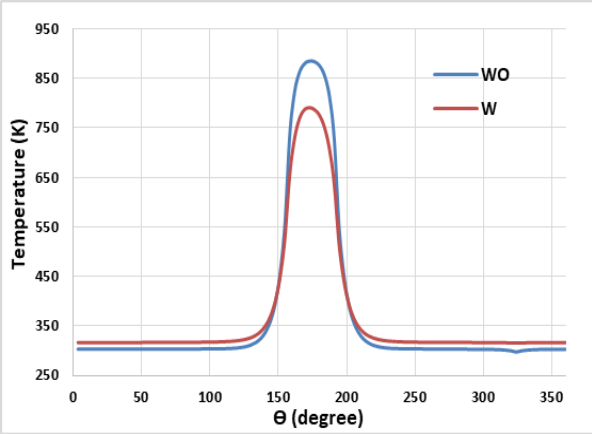



Figure 7-24: The surface temperature of the outer surface of the cavity receiver at length 200 m.

Figure 7-23 and Figure 7-24 show the temperature profile around the outer surface of the cavity circumference with (W) and without (WO) a hot mirror coating. The angle $180^{\circ}$ points directly away from the sun (and towards the center of the parabolic mirror). The temperature difference between W and WO at the aperture is approx. 15 K and 150 K at the length of the receiver unit of 100 m and 200 m, respectively. It is clear that most thermal losses will occur from the aperture window (located between ~153° to 205°), whose temperature is significantly higher that the metallic cavity wall. A hot mirror coating over the cavity opening helps in decreasing the thermal losses, which can be seen by the ~100K lower window temperature at 200m. Around the remaining circumference, the temperature is relatively close to ambient, indicating that the cavity wall is not being heated significantly by the thermal radiation.

### 7.4.4 The performance of the cavity design with a different mass flow rate

The rate of heat transfer into the HTF is directly related to the mass flow rate ($F$), see Eq.(6.13). Controlling the value of this parameter can affect the HTF temperature and the system efficiency as a function of the receiver length. Figure 7-25 shows the HTF temperature as a function of the receiver length with a different value of the mass flow rate (kg/s). This relation gives us the ability to choose the right value of the mass flow rate, which is required not only for estimating how long the receiver length should be but also for the value of the HTF temperature. From Figure 7-26, we can estimate a relation that connects the maximum total efficiency (section 6.4, Eq. (6.16)) and the corresponding length of the parabolic trough (optimal length ($L_{Opt}$)) at different $F$. Furthermore, the length of the parabolic trough that has a particular value of the total efficiency at different $F$ can be obtained. These relations are briefly summarized with the aid of Table 7-3.

At a fixed cavity opening size, the graph broadening distance (ΔL) and $L_{Opt}$ have a direct proportional relation with $F$, i.e., if $F$ increases by twice of its value, the broadening distance, and $L_{Opt}$ will be twice of their distance.

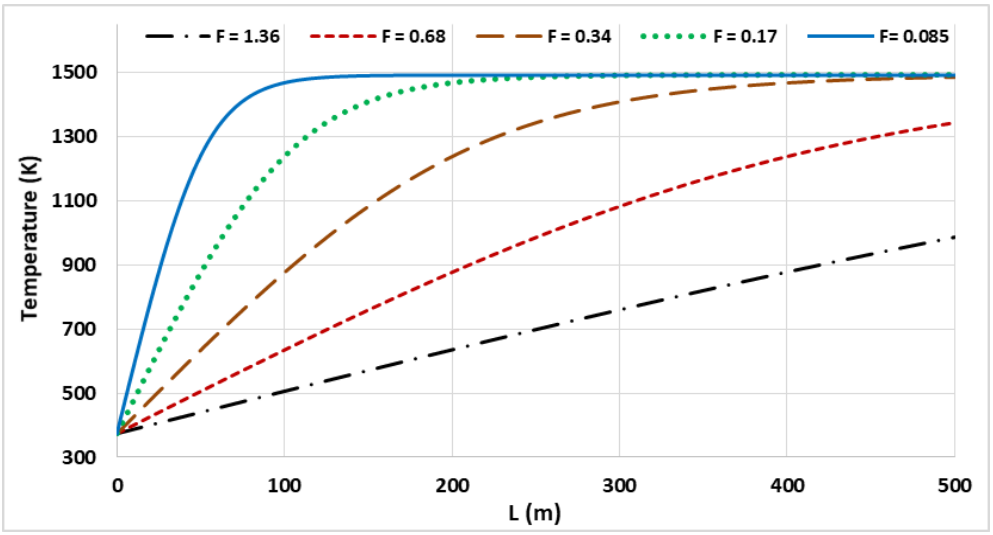



Figure 7-25: HTF temperature as a function of the length of the receiver with different values of the mass flow rate of the HTF.

At any value of the cavity opening size, the ratio of the optimal length ($L_{Opt}$) to $F$ is constant. Therefore, we can identify the value of $L_{Opt}$ at a different value of F. $L_{Opt}$ = c $F$, where c is a constant of proportionality, its value depends on the cavity opening size and the design parameter in Table 7-1 of the parabolic trough collector.

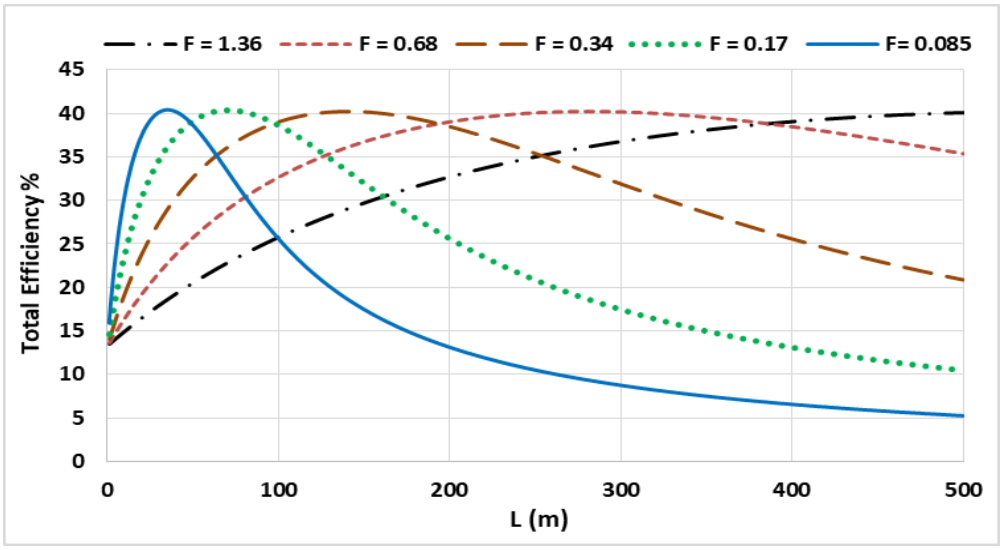
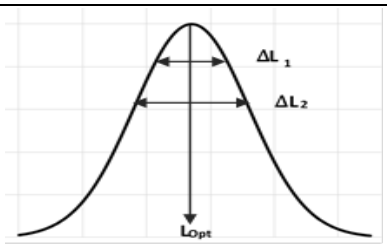



Figure 7-26: The total efficiency of the system as a function of the length of the receiver with different values of the mass flow rate of the HTF (cavity with 30 CVs).

Table 7-3: Results and relations that are related to Figure 7-25.

| Mass flow rate $F$ (kg/s) | | $F$= 0.68 | $F$= 0.34 | $F$= 0.17 | $F$=0.085 |
|---|---|---|---|---|---|
| Max. Tot. eff % | | ~40 % | ~40 % | ~40 % | ~40 % |
| $L_{Opt}$ | | 280 m | 140 m | 70 m | 35 m. |
| ΔL at efficiency | 40% | ~80 m | ~41 m | ~22 m | ~11 m |
| | 35% | ~388 m | ~194 m | ~96 m | ~48 m |
| | 30% | ~ 576m | ~288 m | ~144 m | ~72 m |



The above discussion including Figure 7-25, Figure 7-26 and Table 7-3 illustrates how a flow-rate relates to the optimal length and the broadening distance with almost constant efficiency. It should be noted that the lower the flow rate, the less the total energy the power plant will produce since the plant is shorter and therefore has a smaller mirror area. Sometimes the power production is more important than efficiency.

### 7.4.5 Evaluating the performance of the cavity design compared to selective coating and bare receiver

Next, the cavity design (opening 30 CVs, reflectivity 98%, with hot mirror coating) is compared with existing alternatives, such as a receiver unit with a selective coating, and a bare receiver unit without coating. The simulations parameters that were used are mentioned in Table 7-1 and Table 7-2.

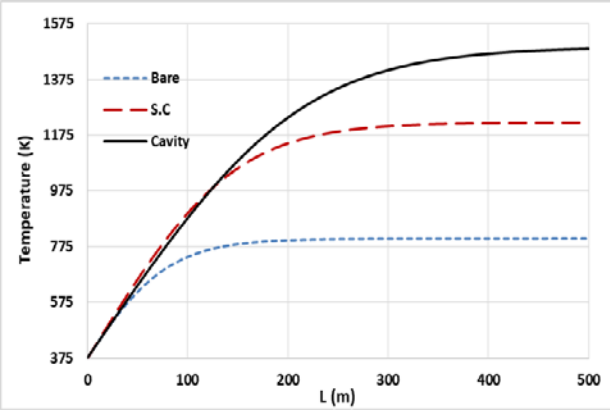



Figure 7-27: HTF outlet temperature for 375 K inlet temperature of different designs.

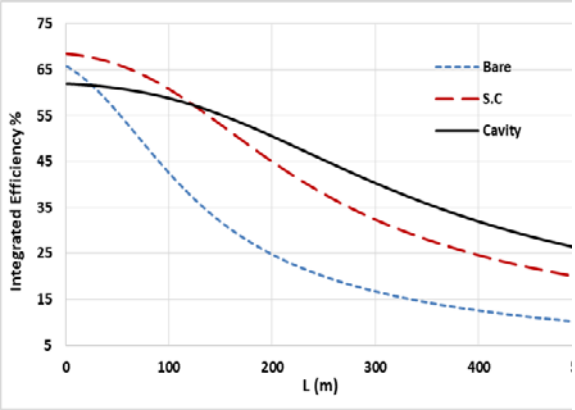



Figure 7-28: Integrated efficiency of the parabolic trough collector with different designs.

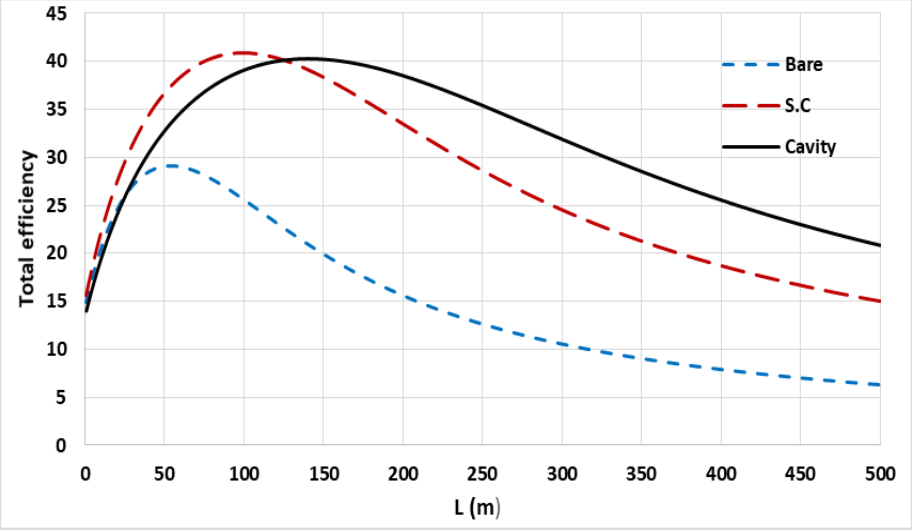



Figure 7-29: The total efficiency of the system as a function of the length of the receiver with different designs.

Figure 7-27 shows the HTF temperature along the length of the receiver unit. It must be remembered that the selective coating on the AP will chemically decompose around 780 K, limiting its length to < 80 m. The cavity design has the capability of exceeding the selective coating temperature ceiling. Figure 7-28 and Figure 7-29 display integrated and total efficiency. The efficiency of the selective coating is better at lower temperatures, but is dominated by the cavity design.

# Chapter 8 : Conclusion and recommendations

## 8.1 Introduction

In this study, a novel design for the Parabolic Trough Collector (PTC) receiver unit is presented. The design aims to challenge the design of conventional systems, offers a decrease in radiant energy losses while raising the temperature of the working fluid. The design incorporates different optically active layers in conjunction with a cavity absorber. The cavity geometry and a hot mirror coating at the aperture enable heightened retention of thermal radiation in the receiver. In addition, novel aspects of the background theory for the design are presented and implemented in a simulation code. We presented experimental results of the cavity receiver unit and compared the results to our model and simulation results. It was seen that the correspondence was encouragingly close, and we proceeded to investigate simulations of the performance regarding different design options. The simulation results for the receiver temperature profiles, the heat transfer fluid temperature, and efficiencies are shown. It is seen that our proposed design has advantages in terms of thermal behavior over conventional designs as it can exceed the heat transfer fluid temperature and the efficiency of existing alternatives.

## 8.2 The mathematical model

The mathematical model of the cavity design with a hot mirror coating over the cavity opening was numerically analyzed using the finite volume method. The cavity opening is coated with Hot Mirror (HM) material, and the rest of the cavity are made from a highly reflective IR mirror (IRM) from inside. HM and IRM have the same mathematical description and heat transfer analysis processes, but they have different optical properties. The model started with describing all the possible heat transfer mode interactions with the parabolic trough collector receiver unit. The receiver unit was then discretized into control volumes to evaluate non-uniform thermal interactions as discussed in Chapter 3. The size of the control volume was considered to be small enough with a close approximation ($< r_A$ , where $r_A$ is the radius of the absorb pipe) so that the temperature varies linearly between neighboring control volumes centers. The conduction heat transfer process occurred between control volumes along the azimuthal direction, and through the thickness in the radial direction. The contribution of the conduction heat transfer in the axial direction was ignored due to the small temperature gradient and the constant solar irradiation along the axial direction [111][112]. The contribution of the convective heat transfer in the parabolic trough solar receiver happens only in two situations; the convective heat transfer between the Heat Transfer Fluid (HTF) and the absorber pipe, and from the HM to the environment. The convective heat transfer from the absorber to the cavity envelope (HM and IRM) was considered to be negligible due to the existence of a vacuum in the annulus. The radiation heat transfer that involves the radiation exchange between the receiver unit component surfaces is in the range of the visible and IR of the electromagnetic radiation. In the receiver unit, the surface of the absorber pipe material was assumed to be diffused and gray, while the HM or IRM surface was a gray and a specular reflector to incoming IR radiation. The radiation exchange via reflections between absorber and HM or IRM is one of our novel and primary aspect. The theory of the reflection mechanism inside the receiver unit with the derivation of the first and second IR reflections terms were mentioned in Chapter 4. Lastly, the net radiation method [119] was applied on each control volume to determine the effective radiation exchange.

The net heat flux of all possible interactions was computed under steady-state conditions using the energy balance relationship, Eq. (6.1), which holds for every control volume.

## 8.3 The simulations

Both control volumes of the absorber pipe and the outer cover of the receiver were incorporated with the energy balance equations. The energy equation balance across the control volume was written with the use of the heat transfer equations that were mentioned in Chapter 3 and Chapter 4. For the computational purposes, the energy balance equation for each control volume was linearized using Taylor expansion Eq. (6.6).

The simulation algorithm is a complex process. The simulations output results are the temperature profiles of the receiver unit components, the temperatures of the inlet and outlet Heat Transfer Fluid (HTF) at different receiver unit lengths and the energy gain in the HTF. The algorithms were summarized in Figure 6-1 and Figure 6-2.

## 8.4 The experiments and simulation validation

Three experiments of different PTC receiver unit designs were performed indoor for thermal performance study and simulation validation, see Chapter 5 for experiment setup descriptions. The first was a conventional receiver without any coating application on either the absorber pipe or glass cover, which is designated the name "Bare". The second experiment was for the receiver using a hot mirror coating on the inner glass cover. The third experiment was for our proposed design of the cavity receiver.

A simulation validation took place in two steps. The first step was setting some physical parameters of the PTC to zero and theoretically expecting the outcomes, such as zero solar irradiation, zero absorber material conductivity, and zero HTF convective heat transfer. The results conformed to theoretical and intuitive expectations. The second step was validating outdoor and indoor simulation codes with existing experimental data. For outdoor simulation code, the experimental data was selected from SEGS (Solar Electric Generating System) LS2, which is one of three generations of parabolic troughs installed in the nine SEGS power plants in California [32]. The discrepancy between the outdoor simulation and the experimental data was studied at different outcome aspects. These aspects hold the discrepancy of the temperature variation along the axial direction at different positions in the circumference of the absorber, which was less than 1% and 0.9% at 6 and 8 m length, respectively. Furthermore, the discrepancy of the glass cover temperature profile around the circumference at a distance of 4 m length was about 0.7%.

In the indoor system, the operation of the experiment was based on heating the absorber pipe using heating elements, from the inside. This process provided a uniform heating distribution, along the length and the circumference. Furthermore, the adjustable number of power generation values of the heating element was used as the input for the indoor simulation code. Therefore, a Chi-squared goodness fit between the simulation and experiment results were used. Chi-squared goodness of fit gave p-values of $> 0.99$ for the glass cover of both bare and hot mirror experiments, whilst it gave p- values of $> 0.99$ and $> 0.8$ for the absorber pipe of the bare and hot mirror receiver. Chi-squared goodness of fit of the cavity design experiment gave p-values of $> 0.95$ for the cavity cover and p-value of $> 0.8$ for the absorber pipe. The main contribution for the divergence comes from

high-temperature points, but the simulation underestimates experimental performance. This divergence is likely due to temperature-dependent simulation parameters and can be included in a more accurate model.

## 8.5 The results discussions

We introduced a cavity concept to reduce thermal radiation losses for receivers of the parabolic trough solar plants and compared it to existing systems. The cavity design performs very well at higher temperatures and is theoretically capable of exceeding 1400 K, thus outperforming current technologies due to its thermal stability. This, in turn, can increase the overall (Carnot) efficiency of the entire plant.

There are further important parameters that affect the temperature profile and the efficiency, such as the cavity opening size and the reflectivity of the cavity mirror. The smallest cavity opening reached the highest temperature. The maximum HTF temperature for this design rises close to 1300 K at 100 control volume (180 mm) and 1490 K at 30 control volume (54 mm). The efficiency of the smallest cavity opening was at 33% compared to 27% for the largest cavity opening, at 400 m. The reflectivity of the inner surface of the cavity has a significant effect on both temperature and efficiency. Different reflectivities were studied (92%, 95%, 98%). It was seen that the highest reflectivity reached the highest temperature (about 200 K higher than the lowest) and had the best efficiency (33% compared to 27% for the lowest, at 400 m).

The cavity system was studied with and without hot mirror coating on the cavity aperture window for a 30 control volume, 98% reflectivity cavity, and the stagnation temperature was found to be ~ 250 K higher with coating. The efficiency was initially dominated by the cavity system without coating, but around 775 K, the hot mirror coated system dominated at higher temperatures. The temperature difference between coating and no coating of the cavity aperture window is approximately 15 K and 150 K at the length of the receiver unit of 100 m and 200 m, respectively. The existence of the hot mirror coating over the cavity opening plays an essential role in decreasing the thermal radiation loss at higher temperature and could reduce the thermal stress in this region. This, in turn, helps increase efficiency.

Also, the mass flow rate value of the heat transfer fluid was found to be a function of the optimal length of the receiver unit at which the total efficiency was maximum, and the range of the receiver unit length at which the system had the minimum losses.

Comparison of the cavity design, a system with selective coating and a bare system indicated that the selective coating performed slightly better in terms of efficiency and temperature, but the cavity system dominated at higher temperatures.

Although the cavity system seems capable of reaching very high temperatures, it is unlikely that it will be used as such. A very high reflectivity (>99%) inside the cavity walls, which is well within the realm of possibility, will make the system very efficient. Higher efficiency will likely allow the HTF to achieve optimum plant temperature within a shorter length, thus reducing the needed receiver unit length. The details of the length reduction depend

on numerous engineering issues related to sizing, and materials used. In addition, this cavity design is more robust and could be produced more cheaply than existing designs, with less maintenance.

## 8.6 Recommendations

In the view of the observations made in this study, future work is required to investigate the following:

- Adding flat plate reflectors at the cavity aperture (the optical funnel)[126]. It is considered as a secondary reflector for increasing the upper limit of the possible concentration ratio of PTC and increasing the optical efficiency. Generally, the PTC focal length, cavity opening, and the tracking error angle have a significant effect on the cavity performance. Therefore, using an optical funnel will reflect back the sheltered light and finally reach the absorber.
- The optimum annulus distance for an efficient reflection mechanism inside the cavity receiver.
- The possibility of adding an insulation layer on the top of the outer cavity surface, especially for the case of lower cavity reflectivity at a higher temperature.
- The research of hot mirror materials that have high visible transmissivity and IR reflectivity.
- Addressing the temperature-dependent parameters in the simulation codes.

# References


[1] Mohamad K, Ferrer P. [Patent] Thermal radiation loss reduction in a parabolic trough receiver by the application of a cavity mirror and a hot mirror coating. PCT/IB2019/053531, South Africa, Johannesburg.

[2] Mohamad K, Ferrer P. Parabolic trough efficiency gain through use of a cavity absorber with a hot mirror. Appl Energy 2019; 238: 1250–1257.

[3] Mohamad K, Ferrer P. Computational comparison of a novel cavity absorber for parabolic trough solar concentrators. Proc 62th Annu Conf South Afr Inst Phys SAIP2017 ArXiv190713066 Physicsapp-Ph.

[4] Mohamad K, Ferrer P. Experimental and numerical measurement of the thermal performance for parabolic trough solar concentrators. Proc 63th Annu Conf South Afr Inst Phys SAIP2018 ArXiv190800515 Physicsapp-Ph.

[5] Kaluba VS, Mohamad K, Ferrer P. Experimental and simulated Performance of Heat Mirror Coatings in a Parabolic Trough Receiver. Submitt Appl Energy J ArXiv190800866 Physicsapp-Ph.

[6] Mohamad K, Ferrer P. Cavity receiver designs for parabolic trough collector. ArXiv190911053 Phys, http://arxiv.org/abs/1909.11053 (2019, accessed 26 September 2019).

[7] Mohamad K, Ferrer P. IR Reflection mechanism inside the annulus between two concentric cylindrical tubes. ArXiv191002311 Phys, http://arxiv.org/abs/1910.02311 (2019, accessed 8 October 2019).

[8] Pavlović TM, Radonjić IS, Milosavljević DD, et al. A review of concentrating solar power plants in the world and their potential use in Serbia. Renew Sustain Energy Rev 2012; 16: 3891–3902.

[9] International Energy Agency iea. CO2 Emissions Statistics from fuel combustion 2018 overview: An essential tool for analysts and policy makers, https://www.iea.org/statistics/co2emissions/ (accessed 23 May 2019).

[10] United Nations Framework Convention on Climate Change. The Paris Agreement | UNFCCC, https://unfccc.int/process-and-meetings/the-paris-agreement/the-paris-agreement (accessed 23 May 2019).

[11] International Energy Agency (iea). World Energy Outlook - WEO-2012. Paris: OECD, http://www.worldenergyoutlook.org/weo2012/ (accessed 13 August 2017).

[12] International Energy Agency (ed). World energy outlook 2011. Paris: OECD, 2011.

[13] Behar O, Khellaf A, Mohammedi K. A review of studies on central receiver solar thermal power plants. Renew Sustain Energy Rev 2013; 23: 12–39.

[14] Gunther M, Joemann M, Csambor S. Advanced CSP Teaching Materials, Chapter 5: Parabolic Trough Technology. EnerMena, 2011.

[15] Chaanaoui M, Vaudreuil S, Bounahmidi T. Benchmark of Concentrating Solar Power Plants: Historical, Current and Future Technical and Economic Development. Procedia Comput Sci 2016; 83: 782–789.

[16] Africa TW. Archimedes through the looking-glass. Class World 1975; 68: 305–308.

[17] Europäische Kommission (ed). European research on concentrated solar thermal energy. Luxembourg: Office for Official Publications of the European Communities, 2004.

[18] Duffie JA, Beckman WA, Worek WM. Solar engineering of thermal processes. Wiley Online Library, 2013.

[19] Winter C-J, Sizmann RL, Vant-Hull LL. Solar power plants: fundamentals, technology, systems, economics. Springer Science & Business Media, 2012.

[20] Garg A, Saini RP. Study on Design of Cavity Receiver of Concentrating Solar Power Plants—A Review. In: Chandra L, Dixit A (eds) Concentrated Solar Thermal Energy Technologies. Springer Singapore, 2018, pp. 69–77.

[21] Kreith F, Goswami DY. Handbook of energy efficiency and renewable energy. Crc Press, 2007.

[22] SolarPaces IEA (iea). Potential for Solar Thermal Energy By Country. SolarPACES, https://www.solarpaces.org/csp-technologies/csp-potential-solar-thermal-energy-by-member-nation/ (accessed 22 October 2019).

[23] Solar Power and Chemical Energy Systems, National Renewable Energy Laboratory (NREL). Concentrating Solar Power Projects | Concentrating Solar Power Projects, https://solarpaces.nrel.gov/ (accessed 4 August 2019).

[24] Islam MT, Huda N, Abdullah AB, et al. A comprehensive review of state-of-the-art concentrating solar power (CSP) technologies: Current status and research trends. Renew Sustain Energy Rev 2018; 91: 987–1018.

[25] Qazi S. Chapter 7 - Solar Thermal Electricity and Solar Insolation. In: Qazi S (ed) Standalone Photovoltaic (PV) Systems for Disaster Relief and Remote Areas. Elsevier, pp. 203–237.

[26] Stine WB, Geyer M. Power from the Sun. Power from the sun. net, 2001.

[27] Flabeg company. Flabeg Mirror. Solar mirror, http://www.flabeg-fe.com/ (accessed 8 July 2019).

[28] DiGrazia M. ReflecTech Mirror Film: Design Flexibility and Durability in Reflecting Solar Applications. 2010; 7.

[29] MIRO SUN. Alanod Solar Company, https://impactsolar.com.au/wp-content/uploads/2018/06/Alanod-Solar-Benefits.pdf (accessed 16 August 2017).

[30] Günther M, Joemann M, Csambor S, et al. Parabolic trough technology. In: Advanced CST teaching materials, enerMENA, http://edge.rit.edu/content/P15484/public/Detailed%20Design%20Documents/Solar%20Trough%20Preliminary%20analysis%20references/Parabolic%20Trough%20Technology.pdf (2011, accessed 13 August 2017).

[31] Burkholder F, Kutscher C. Heat-loss testing of Solel's UVAC3 parabolic trough receiver. United States: National Renewable Energy Laboratory (NREL), Golden, CO., http://www.nrel.gov/docs/fy08osti/42394.pdf (2008, accessed 5 August 2017).

[32] Dudley VE, Kolb GJ, Mahoney AR, et al. Test results: SEGS LS-2 solar collector. Nasa Stirecon Tech Rep N; 96.

[33] Price H, Lupfert E, Kearney D, et al. Advances in parabolic trough solar power technology. J Sol Energy Eng 2002; 124: 109–125.

[34] Price H, Forristall R, Wendelin T, et al. Field Survey of Parabolic Trough Receiver Thermal Performance. In: Solar Energy. Denver, Colorado, USA: ASME, pp. 109–116.

[35] Moya EZ. 7 - Parabolic-trough concentrating solar power (CSP) systems. In: Lovegrove K, Stein W (eds) Concentrating Solar Power Technology. Woodhead Publishing, pp. 197–239.

[36] Forristall R. Heat transfer analysis and modeling of a parabolic trough solar receiver implemented in engineering equation solver. National Renewable Energy Lab., Golden, CO.(US),

http://large.stanford.edu/publications/coal/references/troughnet/solarfield/docs/34169.pdf (2003, accessed 13 August 2017).

[37] Ramchandra G. P, Sudhir V. P, Jyeshtharaj B. J, et al. Alternative designs of evacuated receiver for parabolic trough collector. Energy; 155: 66–76.

[38] Fuqiang W, Ziming C. Progress in concentrated solar power technology with parabolic trough collector system: A comprehensive review. Renew Sustain Energy Rev 2017; 79: 1314–1328.

[39] Wang P, Liu DY, Xu C. Numerical study of heat transfer enhancement in the receiver tube of direct steam generation with parabolic trough by inserting metal foams. Appl Energy 2013; 102: 449–460.

[40] Sargent, Lundy LLC Consulting Group. Assessment of Parabolic Trough and Power Tower Solar Technology Cost and Performance Forecasts. Chicago, Illinois: DIANE Publishing, https://scholar.google.co.za/scholar?hl=en&as_sdt=0%2C5&q=Assessment+of+Parabolic+Trough+and+Power+Tower+Solar+Technology+Cost+and+Performance+Forecasts&btnG= (2003).

[41] International Renewable Energy Agency. Renewable energy technologies: cost analysis series: concentrating solar power; 2012., https://www.irena.org/DocumentDownloads/Publications/RE_Technologies_Cost_Analysis-CSP.pdf (accessed 13 August 2017).

[42] Kaluba VS. Simulation of a hot mirror parabolic troughsolar collector receiver. PhD Thesis, 2018.

[43] Yunus CA, Afshin JG. Heat and mass transfer: fundamentals and applications. 5 Ed. 2015.

[44] Eschrich H. Grundlagen der photovoltaischen Energiewandlung: Solarstrahlung, Halbleitereigenschaften und Solarzellenkonzepte. Vieweg+Teubner Verlag, https://www.springer.com/de/book/9783519032182 (1994, accessed 27 June 2019).

[45] Matthias G. Advanced CSP Teaching Materials, Chapter 2: Solar Radiation. In: Advanced CSP Teaching Materials. Germany: EnerMena, 2011.

[46] Pitz-Paal R, Hoyer-Klick C. Introduction to Solar Resource Assessments. 2010; 149.

[47] Kalogirou SA. Solar thermal collectors and applications. Prog Energy Combust Sci 2004; 30: 231–295.

[48] Spencer JW. Fourier series representation of the position of the sun. Search 1971; 2: 172–172.

[49] Cooper PI. The absorption of radiation in solar stills. Sol Energy 1969; 12: 333–346.

[50] Abengoa company. Abengoa Solar, Soluciones innovadoras para el desarrollo sostenible, http://www.abengoasolar.com/ (accessed 8 November 2018).

[51] Kalogirou SA. Solar energy engineering: processes and systems. Academic Press, 2013.

[52] Cyulinyana MC, Ferrer P. Heat efficiency of a solar trough receiver with a hot mirror compared to a selective coating. South Afr J Sci 2011; 107: 01–07.

[53] Antonaia A, Castaldo A, Addonizio ML, et al. Stability of W-Al 2 O 3 cermet based solar coating for receiver tube operating at high temperature. Sol Energy Mater Sol Cells 2010; 94: 1604–1611.

[54] Forristall R. EES heat transfer model for solar receiver performance. Proc ISEC Sol 2004; 11–14.

[55] Kennedy CE. Review of mid-to high-temperature solar selective absorber materials. National Renewable Energy Lab., Golden, CO.(US), http://large.stanford.edu/publications/power/references/troughnet/solarfield/docs/31267.pdf (2002, accessed 8 August 2017).

[56] Kennedy CE, Price H. Progress in Development of High-Temperature Solar-Selective Coating. ASME Int Sol Energy Conf Sol Energy 2005; 749–755.

[57] ASE. Archimede Solar Energy, http://www.archimedesolarenergy.it/ (accessed 8 December 2017).

[58] SCHOTT. SCHOTT PTR 70, https://www.schott.com/d/csp/370a8801-3271-4b2a-a3e6-c0b5c78b01ae/1.0/schott_ptr70_4th_generation_brocure.pdf (accessed 27 February 2019).

[59] Murr L. Solar Materials Science. Elsevier, 2012.

[60] Granqvist CG. Spectrally Selective Coatings for Energy Efficiency and Solar Applications. Phys Scr 1985; 32: 401.

[61] Canan K. Performance analysis of a novel concentrating photovoltaic combined system. Energy Convers Manag 2013; 67: 186–196.

[62] Miller DC, Khonkar HI, Herrero R, et al. An end of service life assessment of PMMA lenses from veteran concentrator photovoltaic systems. Sol Energy Mater Sol Cells 2017; 167: 7–21.

[63] Lampert CM. Coatings for enhanced photothermal energy collection II. Non-selective and energy control films. Sol Energy Mater 1979; 2: 1–17.

[64] Grena R. Efficiency Gain of a Solar Trough Collector Due to an IR-Reflective Film on the Non-Irradiated Part of the Receiver. Int J Green Energy 2011; 8: 715–733.

[65] Reddy KS, Ravi Kumar K, Ajay CS. Experimental investigation of porous disc enhanced receiver for solar parabolic trough collector. Renew Energy 2015; 77: 308–319.

[66] Ghasemi S, Ranjbar A. Numerical thermal study on effect of porous rings on performance of solar parabolic trough collector. Appl Therm Eng 2017; 118: 807–816.

[67] Mwesigye A, Bello-Ochende T, Meyer JP. Heat transfer and thermodynamic performance of a parabolic trough receiver with centrally placed perforated plate inserts. Appl Energy 2014; 136: 989–1003.

[68] Sahin H, Baysal E. Investigation of heat transfer enhancement in a new type heat exchanger using solar parabolic trough systems. Int J Hydrog Energy 2015; 40: 15254–15266.

[69] Huang Z, LI Z. Numerical investigations on fully-developed mixed turbulent convection in dimpled parabolic trough receiver tubes. Appl Therm Eng 2017; 114: 1287–1299.

[70] Cheng Z, He YL. Numerical study of heat transfer enhancement by unilateral longitudinal vortex generators inside parabolic trough solar receivers. Int J Heat Mass Transf 2012; 55: 5631–5641.

[71] Fuqiang W, Qingzhi L, Huaizhi H. Parabolic trough receiver with corrugated tube for improving heat transfer and thermal deformation characteristics. Appl Energy 2016; 164: 411–424.

[72] Fuqiang W, Zhexiang T, Xiangtao G. Heat transfer performance enhancement and thermal strain restrain of tube receiver for parabolic trough solar collector by using asymmetric outward convex corrugated tube. Energy 2016; 114: 275–292.

[73] Bellos E, Tzivanidis C, Antonopoulos KA. Thermal enhancement of solar parabolic trough collectors by using nanofluids and converging-diverging absorber tube. Renew Energy 2016; 94: 213–222.

[74] Hassani S, Saidur R, Mekhilef S, et al. A new correlation for predicting the thermal conductivity of nanofluids; using dimensional analysis. Int J Heat Mass Transf 2015; 90: 121–130.

[75] Wenslawski H. The global CSP market-its industry structure and decision mechanisms. Hambg Diplomarb Univ.

[76] Patil RG, Panse SV, Joshi JB. Optimization of non-evacuated receiver of solar collector having non-uniform temperature distribution for minimum heat loss. Energy Convers Manag 2014; 85: 70–84.

[77] Stettenheim J, McBride TO, Brambles OJ. Cavity Receivers for Parabolic Solar Troughs. 2013.

[78] Bader R, Pedretti A, Barbato M, et al. An air-based corrugated cavity-receiver for solar parabolic trough concentrators. Appl Energy 2015; 138: 337–345.

[79] Bader R, Pedretti A, Steinfeld A. Experimental and numerical heat transfer analysis of an air-based cavity-receiver for solar trough concentrators. J Sol Energy Eng 2012; 134: 021002.

[80] Hänchen M, Brückner S, Steinfeld A. High-temperature thermal storage using a packed bed of rocks – Heat transfer analysis and experimental validation. Appl Therm Eng 2011; 31: 1798–1806.

[81] G. Z, A. P, A. H, et al. Design of packed bed thermal energy storage systems for high-temperature industrial process heat. Appl Energy; 137: 812–822.

[82] Burkholder F, Kutscher C. Heat Loss Testing of Schott's 2008 PTR70 Parabolic Trough Receiver. NREL/TP--550-45633, 1369635. Epub ahead of print 1 May 2009. DOI: 10.2172/1369635.

[83] Barra OA, Franceschi L. The parabolic trough plants using black body receivers: experimental and theoretical analyses. Sol Energy 1982; 28: 163–171.

[84] Boyd DA, Gajewski R, Swift R. A cylindrical blackbody solar energy receiver. Sol Energy 1976; 18: 395–401.

[85] Li X, Chang H, Duan C, et al. Thermal performance analysis of a novel linear cavity receiver for parabolic trough solar collectors. Appl Energy 2019; 237: 431–439.

[86] Cao F, Li Y, Wang L, et al. Thermal performance and stress analyses of the cavity receiver tube in the parabolic trough solar collector. In: IOP Conference Series: Earth and Environmental Science. IOP Publishing, 2016, p. 012067.

[87] Fei C, Lei W, Tianyu Z. Design and Optimization of Elliptical Cavity Tube Receivers in the Parabolic Trough Solar Collector. Int J Photoenergy; 2017: 7.

[88] Chen F, Li M, Xu C, et al. Study on heat loss performance of triangle cavity absorber for parabolic trough concentrators. In: Materials for Renewable Energy and Environment (ICMREE), 2013 International Conference on. IEEE, 2014, pp. 683–689.

[89] Xiong Y, Wu Y, Ma C, et al. Numerical investigation of thermal performance of heat loss of parabolic trough receiver. Sci China Technol Sci 2010; 53: 444–452.

[90] Xiao X, Zhang P, Shao DD, et al. Experimental and numerical heat transfer analysis of a V-cavity absorber for linear parabolic trough solar collector. Energy Convers Manag 2014; 86: 49–59.

[91] Chen F, Li M, Zhang P, et al. Thermal performance of a novel linear cavity absorber for parabolic trough solar concentrator. Energy Convers Manag 2015; 90: 292–299.

[92] Chen F, Li M, Hassanien Emam Hassanien R, et al. Study on the optical properties of triangular cavity absorber for parabolic trough solar concentrator. Int J Photoenergy; 2015.

[93] Hongbo L, Chunguang Z, Man F. Study on the thermal performance of a novel cavity receiver for parabolic trough solar collectors. Appl Energy 2018; 222: 790–798.

[94] Liang H, Fan M, You S, et al. An analysis of the heat loss and overheating protection of a cavity receiver with a novel movable cover for parabolic trough solar collectors. Energy 2018; 158: 719–729.

[95] Zhai H, Dai Y, Wu J, et al. Study on trough receiver for linear concentrating solar collector. In: Proceedings of ISES World Congress 2007 (Vol. I–Vol. V). Springer, 2008, pp. 711–715.

[96] Singh PL, Sarviya RM, Bhagoria JL. Heat loss study of trapezoidal cavity absorbers for linear solar concentrating collector. Energy Convers Manag 2010; 51: 329–337.

[97] Singh PL, Sarviya RM, Bhagoria JL. Thermal performance of linear Fresnel reflecting solar concentrator with trapezoidal cavity absorbers. Appl Energy 2010; 87: 541–550.

[98] Manikumar R, Palanichamy R, Arasu AV. Heat transfer analysis of an elevated linear absorber with trapezoidal cavity in the linear Fresnel reflector solar concentrator system. J Therm Sci 2015; 24: 90–98.

[99] Facão J, Oliveira AC. Numerical simulation of a trapezoidal cavity receiver for a linear Fresnel solar collector concentrator. Renew Energy 2011; 36: 90–96.

[100] Reynolds DJ, Jance MJ, Behnia M, et al. An experimental and computational study of the heat loss characteristics of a trapezoidal cavity absorber. Sol Energy 2004; 76: 229–234.

[101] Natarajan E, Basak T, Roy S. Natural convection flows in a trapezoidal enclosure with uniform and non-uniform heating of bottom wall. Int J Heat Mass Transf 2008; 51: 747–756.

[102] Liang H, Fan M, You S, et al. A Monte Carlo method and finite volume method coupled optical simulation method for parabolic trough solar collectors. Appl Energy 2017; 201: 60–68.

[103] Natarajan SK, Reddy KS, Mallick TK. Heat loss characteristics of trapezoidal cavity receiver for solar linear concentrating system. Appl Energy 2012; 93: 523–531.

[104] Lampert CM. Heat mirror coatings for energy conserving windows. Sol Energy Mater 1981; 6: 1–41.

[105] Lampert CM. Advanced optical materials for energy efficiency and solar conversion. Sol Wind Technol 1987; 4: 347–379.

[106] Valkonen E, Karlsson B, Ribbing CG. Solar optical properties of thin films of Cu, Ag, Au, Cr, Fe, Co, Ni and Al. Sol Energy 1984; 32: 211–222.

[107] Hamberg I, Granqvist CG. Optical properties of transparent and heat-reflecting indium-tin-oxide films: Experimental data and theoretical analysis. Sol Energy Mater 1984; 11: 239–248.

[108] Yaghoubi M, Ahmadi F, Bandehee M. Analysis of Heat Losses of Absorber Tubes of Parabolic through Collector of Shiraz (Iran) Solar Power Plant. J Clean Energy Technol 2013; 33–37.

[109] Kaluba VS, Ferrer P. A model for hot mirror coating on solar parabolic trough receivers. J Renew Sustain Energy 2016; 8: 053703.

[110] Mohamad K, Philippe F. Parabolic trough efficiency gain through use of a cavity absorber with a hot mirror - ScienceDirect. Applied Energy; 238: 1250–1257.

[111] Hachicha AA, Rodríguez I, Capdevila R, et al. Heat transfer analysis and numerical simulation of a parabolic trough solar collector. Appl Energy 2013; 111: 581–592.

[112] Wirz M, Roesle M, Steinfeld A. Three-dimensional optical and thermal numerical model of solar tubular receivers in parabolic trough concentrators. J Sol Energy Eng 2012; 134: 041012.

[113] William SJ. Engineering heat transfer. CRC press, 2000.

[114] Lienhard IV JH, Lienhard JH. V, 2008, A Heat Transfer Textbook. Phlogiston Press, Cambridge, MA, 2009.

[115] Gnielinski V. New equations for heat and mass transfer in the turbulent flow in pipes and channels. NASA STIrecon Tech Rep A 1975; 75: 8–16.

[116] Bhowmik NC, Mullick SC. Calculation of tubular absorber heat loss factor. Sol Energy 1985; 35: 219–225.

[117] Incropera FP, Dewitt DP. Fundamentals of mass and heat transfer. Third Edition. New York: John Wiley and Sons, 1990.

[118] Hottel HC. Radiant heat transmission. Third edition., W.H. McAdams, (Ed.). New York: McGraw-Hill, 1954.

[119] Modest MF. Radiative heat transfer. Academic press, https://books.google.co.za/books?hl=en&lr=&id=J2KZq0e4lCIC&oi=fnd&pg=PP1&dq=M.+F.+Modest,+Radiative+heat+transfer+(Academic+press,+2013).&ots=_A8Zz8NZeY&sig=-dvb6CsMq0xJTKBzXYcFHscLUQs (2013, accessed 14 August 2017).

[120] Arduino. Arduino Mega 2560 Rev3, https://www.arduino.cc/ (accessed 21 July 2019).

[121] Maxim Integrated Compay. MAX6675 Cold-Junction-Compensated K-Thermocouple-to-Digital Converter (0°C to +1024°C) - Maxim, https://www.maximintegrated.com/en/products/sensors/MAX6675.html (accessed 21 July 2019).

[122] Park R, Carroll R, Burns G, et al. Manual on the Use of Thermocouples in Temperature Measurement, Fourth Edition, Sponsored by ASTM Committee E20 on Temperature Measurement. 4TH ed. ASTM International. Epub ahead of print 1 January 1993. DOI: 10.1520/MNL12-4TH-EB.

[123] Jeter SM. Calculation of the concentrated flux density distribution in parabolic trough collectors by a semifinite formulation. Sol Energy 1986; 37: 335–345.

[124] Patankar S. Numerical heat transfer and fluid flow. CRC press, 1980.

[125] Pech AJ, Soberanis ME. Efficiency curves analysis of a parabolic trough solar collector in the Yucatan Peninsula. J Renew Sustain Energy 2012; 4: 021203.

[126] Ferrer P. Enhanced efficiency of a parabolic solar trough system through use of a secondary radiation concentrator. South Afr J Sci 2008; 104: 383–388.

[127] CAPGO D acquisition for industry ad research professionals based on measurements. Capgo - Temperature Measurement, http://www.capgo.com/Resources/Temperature/TempHome/TempMeasurement.html (accessed 21 July 2019).

[128] MAX6675 supplier. MAX6675 Thermocouple Temperature Module. ProtoSupplies, https://protosupplies.com/product/max6675-thermocouple-temperature-module/ (accessed 21 July 2019).

# Appendix I

# Current PTC power plants worldwide

Table 0-1: List of all PTC in the world at the time of writing [23]. OP, U.D, U.C, and N.OP mean operating, under development, under construction, and currently non-operation.

| Country | Location | Name | Status | Turbine Capacity (MW) | Thermal storage |
|---|---|---|---|---|---|
| **Algeria** | Hassi R'mel | ISCC Hassi R'mel | OP (2011) | 20 | None |
| **Canada** | Medicine Hat Alberta | City of medicine Hat ISCC | OP (2014) | 1.1 | None |
| **China** | Chabei | Chabei | UD | 64 | 2-tank direct/16hrs |
| | Delingha | Deligha | OP (2018) | 50 | 2-tank indirect /9hrs |
| | Akesai | Gansu Akesai | U.C | 50 | 2-tank direct /15hrs |
| | Wuwei | Gulang | U.D | 100 | 2-tank indirect /7hrs |
| | Yumen | Rayspower | U.C | 50 | 2-tank indirect /7hrs |
| | Urat Middle Banner | Urat Middl | U.C | 100 | 2-tank indirect /4hrs |
| | Yumen | Yumen | U.D | 50 | 2-tank indirect /7hrs |
| **Denemark** | Brønderslev | Aalborg CSP-Bronderslev CSP | OP (2016) | 16.6 | None |
| **Egypt** | Kuraymat | Integrated Solar Combined Cycle (ISCC) | OP (2011) | 20 | None |
| **India** | Phalodi | Abijeet Solar | U.C | 50 | None |
| | Askandra | Diwakar | U.C | 100 | 2-tank indirect /4hrs |
| | Nokh | Godawari Solar | OP(2013) | 50 | None |
| | Kutch (Gujarat) | Gujarat Solar One | U.C | 25 | 2-tank indirect /9hrs |
| | Askandra | KVK Energy Solar | U.C | 100 | 2-tank indirect /4hrs |
| | Anantapur | Megha Solar Plant | OP (2014) | 50 | None |
| | Gurgaon | National Solar Thermal Power Facility | OP (2012) | 1 | None |
| **Israel** | Ashalim | Ashalim | U.D | 110 | 2-tank indirect /4.5hrs |

| | | | | | |
|---|---|---|---|---|---|
| **Italy** | Priolo Gargallo | Archimede | OP (2010) | 5 | 2-tank direct /8hrs |
| | Massa Martana | ASE Demo Plant | OP (2013) | 0.35 | 2-tank direct /--- |
| **Kuwait** | Kuwait City | Shagaya CSP | OP (2019) | 50 | 2-tank indirect /9hrs |
| **Mexico** | Agua Prieta, | Agua Prieta II | U.C | 14 | None |
| **Morocco** | Ait Baha | Airlight Energy Ait-Baha Plant | OP (2014) | 3 | ---/5hrs |
| | Ain Beni Mathar | ISCC Ain Beni Mathar | OP (2010) | 20 | None |
| | Ouarzazate | Noor I | OP (2015) | 160 | 2-tank indirect /3hrs |
| | Ouarzazate | Noor II | OP (2018) | 200 | 2-tank indirect /7hrs |
| | Ouarzazate | Noor III | U.C | 150 | 2-tank direct /7hrs |
| **Saudi Arabia** | Duba | ISCC Duba 1 | U.C | 43 | --- |
| | Waad Al Shamal | Waad Al Shamal ISCC Plant | U.C | 50 | --- |
| **South Africa** | Groblershoop | Bokpoort | OP (2016) | 55 | 2-tank indirect /9.3hrs |
| | Upington | Ilanga I | OP (2018) | 100 | 2-tank indirect /5hrs |
| | Kathu | Kathu Solar Park | OP (2019) | 100 | 2-tank indirect /4.5hrs |
| | Poffader | KaXu Solar One | OP (2015) | 100 | 2-tank indirect /2.5hrs |
| | Pofadder | Xina Solar One | OP (2018) | 100 | 2-tank indirect /5hrs |
| **Spain** | Aldeire Granada | Andasol-1 | OP (2008) | 50 | 2-tank indirect /7.5hrs |
| | Aldeire Granada | Andasol-2 | OP (2009) | 50 | 2-tank indirect /7.5hrs |
| | Aldeire Granada | Andasol-3 | OP (2011) | 50 | 2-tank indirect/7.5hrs |
| | San José del Valle Cádiz | Arcosol 50 (Valle 1) | OP (2011) | 49.9 | 2-tank indirect/7.5hrs |
| | Morón de la Frontera Sevilla | Arenales | OP (2013) | 50 | 2-tank indirect/7hrs |
| | Alcázar de San Juan Ciudad Real | Aste 1A | OP (2012) | 50 | 2-tank indirect/8hrs |
| | Alcázar de San Juan Ciudad Real | Aste 1B | OP (2012) | 50 | 2-tank indirect/8hrs |
| | Olivenza Badajoz | Astexol II | OP (2012) | 50 | 2-tank indirect/8hrs |
| | Les Borges Blanques Lleida | Borges Termosolar | OP (2012) | 22.5 | None |
| | Talarrubias Badajoz | Casablanca | OP (2013) | 50 | 2-tank indirect/7.5hrs |
| | Villena Alicante | Enerstar | OP (2013) | 50 | None |

| | | | | | |
|---|---|---|---|---|---|
| | Torre de Miguel Sesmero Badajoz | Extresol-1 | OP (2010) | 50 | 2-tank indirect/7.5hrs |
| | Torre de Miguel Sesmero Badajoz | Extresol-2 | OP (2010) | 49.9 | 2-tank indirect/7.5hrs |
| | Torre de Miguel Sesmero Badajoz | Extresol-3 | OP (2012) | 50 | 2-tank indirect/7.5hrs |
| | Palma del Río Córdoba | Guzman | OP (2012) | 50 | None |
| | Écija Sevilla | Helioenergy 1 | OP (2011) | 50 | None |
| | Écija Sevilla | Helioenergy 2 | OP (2012) | 50 | None |
| | Puerto Lápice Ciudad Real | Helios I | OP (2012) | 50 | None |
| | Puerto Lápice Ciudad Real | Helios II | OP (2012) | 50 | None |
| | Puertollano | Ibersol Ciudad Real | OP (2009) | 50 | None |
| | Posadas Córdoba | La Africana | OP (2012) | 50 | 2-tank indirect/7.5hrs |
| | La Garrovilla Badajoz | La Dehesa | OP (2011) | 49.9 | 2-tank indirect/7.5hrs |
| | Badajoz Badajoz | La Florida | OP (2010) | 50 | 2-tank indirect/7.5hrs |
| | Alvarado Badajoz | La Risca | OP (2009) | 50 | None |
| | Lebrija Sevilla | Lebrija 1 | OP (2011) | 50 | None |
| | Majadas de Tiétar Cáceres | Majadas 1 | OP (2010) | 50 | None |
| | Alcazar de San Juan Ciudad Real | Manchasol-1 | OP (2011) | 49.9 | 2-tank indirect/7.5hrs |
| | Alcazar de San Juan Ciudad Real | Manchasol-2 | OP (2011) | 50 | 2-tank indirect/7.5hrs |
| | Morón de la Frontera | Moron | OP (2012) | 50 | None |
| | Olivenza Badajoz | Olivenza 1 | OP (2012) | 50 | None |

| | | | | | |
|---|---|---|---|---|---|
| | Orellana Badajoz | Orellana | OP (2012) | 50 | None |
| | Palma del Río Córdoba | Palma del Rio I | OP (2011) | 50 | None |
| | Palma del Río Córdoba | Palma del Rio II | OP (2010) | 50 | None |
| | Logrosán Cáceres | Solaben 1 | OP (2013) | 50 | None |
| | Logrosán Cáceres | Solaben 2 | OP (2012) | 50 | None |
| | Logrosán Cáceres | Solaben 3 | OP (2012) | 50 | None |
| | Logrosán Cáceres | Solaben 6 | OP (2013) | 50 | None |
| | El Carpio Córdoba | Solacor 1 | OP (2012) | 50 | None |
| | El Carpio Córdoba | Solacor 2 | OP (2012) | 50 | None |
| | Sevilla | Solnova 1 | OP (2009) | 50 | None |
| | Sevilla | Solnova 3 | OP (2009) | 50 | None |
| | Sevilla | Solnova 4 | OP (2009) | 50 | None |
| | San José del Valle Cádiz | Termesol 50 | OP (2011) | 49.9 | 2-tank indirect/7.5hrs |
| | Navalvillar de Pela Badajoz | Termosol 1 | OP (2013) | 50 | 2-tank indirect/9hrs |
| | Navalvillar de Pela Badajoz | Termosol 2 | OP (2013) | 50 | 2-tank indirect/9hrs |
| **Thailand** | Huai Kachao | Thai Solar Energy 1 | OP (2012) | 5 | None |
| **United Arab Emirates** | Dubai | DEWA CSP Trough Project | U.C | 600 | 2-tank indirect/15hrs |
| | Abu Dhabi | Shams 1 | OP (2013) | 100 | None |
| **USA** | Arizona | Saguaro Power Plant | N.OP | 1.16 | None |
| | Arizona | Solana Generating Station | OP (2013) | 280 | 2-tank indirect/6hrs |
| | California | Genesis Solar Energy Project | OP (2014) | 250 | None |
| | California | Mojave Solar Project | OP (2014) | 280 | None |

| | | | | | |
|---|---|---|---|---|---|
| | California | Solar Electric Generating Station I (SEGS I) | N.OP | 13.8 | 2-tank direct/3hrs |
| | California | SEGS II | N.OP | 33 | None |
| | California | SEGS III | OP (1985) | 33 | None |
| | California | SEGS IV | OP (1989) | 33 | None |
| | California | SEGS IX | OP (1990) | 89 | None |
| | California | SEGS V | OP (1989) | 33 | None |
| | California | SEGS VI | OP (1989) | 35 | None |
| | California | SEGS VII | OP (1989) | 35 | None |
| | California | SEGS VIII | OP (1989) | 89 | None |
| | Colorado | Colorado Integrated Solar Project | N.OP | 2 | None |
| | Florida | Martin Next Generating Solar Energy Center | OP (2010) | 75 | None |
| | Hawaii | Holaniku at Keahole Point | N.OP | 2 | ---/2hrs |
| | Nevada | Nevada Solar One | OP (2007) | 75 | --- |
| | Nevada | Stillwater GeoSolar Hybrid Plant | OP (2015) | 2 | None |

# Appendix II

# Thermal radiation between the receiver components and the View factor calculations

The view factor calculations using the Hottel's crossed string method is explained in section 3.5.3. Here, we are going to calculate the view factor that has been utilized in this work and their implementation in the simulation code. To demonstrate this method, see the geometry shown in Figure. I.1

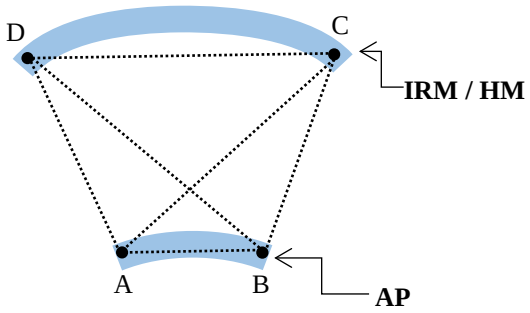



Figure I.1: Determination of the view factor in the receiver unit using the crossed string method.

According to this method, the view factor from Absorber Pipe (AP) to IR Mirror (IRM) or Hot Mirror (HM) equals

$$F_{AP,HM} = \frac{\sum crossed\ strings - \sum uncrossed\ strings}{2 \times the\ string\ of\ AP\ surface} = \frac{(AC+BD)-(AD+BC)}{2 \times AB}, \quad \text{(I.1)}$$

This appendix will make use of HM notation only, keeping in mind that the same physical and geometric process is applied to IRM.

### 1. The view factor from AP to HM

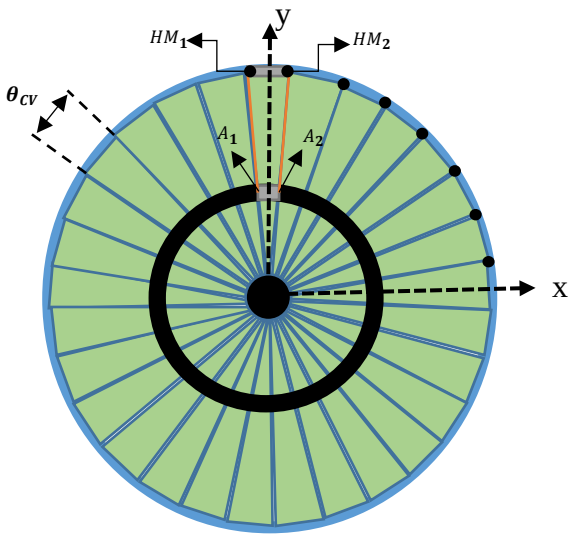



Figure I.2: Description of the view factor between the glass cover and absorber pipe control volume in a cross-section of the receiver unit.

According to Eq. I.1 and by applying it to the situation in Figure I.2, the view factor from the HM control volume to AP control volume can be written as

$$F_{A_1A_2,HM_1HM_2} = \frac{(|HM_1-A_2|+|HM_2-A_1|)-(|HM_1-A_1|+|HM_2-A_2|)}{2\times r_{ab,o}\times\theta_{CV}}, \quad \text{(I.2)}$$

where $r_{ab,o}$ is the outer radius of the AP and the rest of symbols are shown in Figure I.2. The Cartesian coordinates of the points $HM_1$, $HM_2$, $A_1$, and $A_2$ can be easily determined by first obtaining their polar coordinates then write their X and Y components for each point. For example, $HM_1 = \left(r_{g,in}, \left(90+\frac{\theta_{CV}}{2}\right)\right) = r_{g,in}\cos\left(90+\frac{\theta_{CV}}{2}\right), r_{HM,in}\sin\left(90+\frac{\theta_{CV}}{2}\right)$, where $r_{HM,in}$ is the inner radius of the outer cover and the angle $\left(90+\frac{\theta_{CV}}{2}\right)$ is measured with respect to the positive X-axis. The view factor from AP control volume ($A_1$ $A_2$) to the HM control volumes can be written as

$$\sum_{ij} F_{A_1A_2,G_iG_j} = \frac{(|G_i-A_2|+|G_j-A_1|)-(|G_i-A_1|+|G_j-A_2|)}{2\times r_{ab,o}\times\theta_{CV}}. \quad \text{(I.3)}$$

The summation in Eq.(I.3) continues until the $\overline{HM_jA_2}$ makes an angle 0˚with respect X-axis. To obtain the view factor from the HM control volume to the AP control volumes, we can apply the reciprocity relation

$$A_{AP,CV}F_{A_1A_2,HM_1HM_2} = A_{HM,CV}F_{HM_1HM_2,A_1A_2}, \quad \text{(I.4)}$$

$$F_{HM_1HM_2,A_1A_2} = \frac{A_{AP,CV}}{A_{HM,CV}}F_{A_1A_2,HM_1HM_2}, \quad \text{(I.5)}$$

where $A_{AP,CV}$ and $A_{HM,CV}$ are the surface area of the absorber control volume and the HM cover control volume. Also, the methods mentioned above will provide us with the number of the HM control volumes that are going to be in thermal contact with AP control volume and vice versa. There is also another method to confirm these number of the HM control volumes or AP control volumes that are in thermal contact with each other. It will be discussed in the following sections.

### 1.1. The number of the glass cover segments that are in thermal contact with the absorber pipe segment (AG)

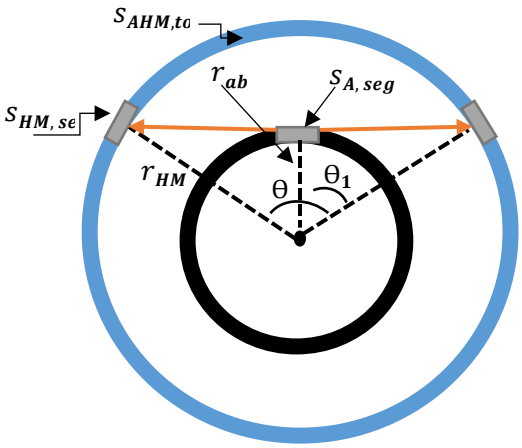



Figure I.3: Graphical representation for the maximum reflection from AP to HM

In this derivation, we need to evaluate the maximum number of control volume on the HM cover that is going to be hit by one irradiated AP control volume, as shown in Figure I.3. Starting this derivation by evaluating $\theta_1$

$$\cos\Theta_1 = \frac{r_{ab}}{r_{HM}}, \tag{I.6}$$

and

$$\Theta = 2\Theta_1 = 2\cos^{-1}\frac{r_{ab}}{r_{HM}}. \tag{I.7}$$

The arc length of the HM cover control volume is $S_{HM,seg} = \Theta_{seg}\, r_{HM}$ and the total arc length with a central angle $\theta$ is

$S_{AHM,tot} = \Theta\, r_{HM}$. Now, the number of HM cover segments (control volume's number) that can be affected due to thermal radiation of one AP segment is

$$N_{AP-HM}^{CV} = \frac{S_{AHM,tot}}{S_{HM,seg}} = \frac{\Theta\, r_{HM}}{\Theta_{seg}\, r_{HM}} = \frac{2\cos^{-1}(r_{ab}/r_{HM})}{\theta_{seg}}. \tag{I.8}$$

### 1.2. The number of the absorber pipe segments that are in thermal contact with the glass cover segment

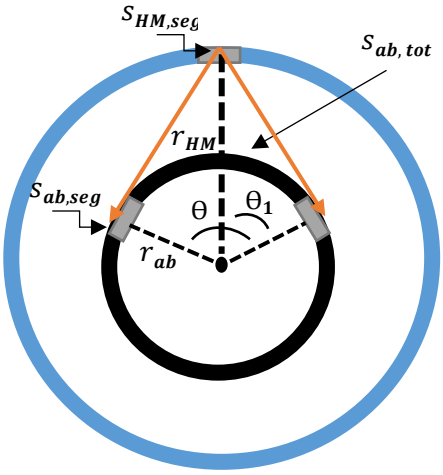



Figure I.4: Graphical representation for the maximum reflection from HM to AP

This derivation aims to find the maximum number of AP control volumes that are in radiative contact with one HM control volume. This is due to the reflection from the HM control volume, as shown in Figure I.4. The derivation starts by evaluating $\theta$, where

$$\theta = 2\theta_1 = 2\cos^{-1}\frac{r_{ab}}{r_{HM}}. \tag{I.9}$$

By knowing the total arc length of the absorber pipe $S_{ab,tot} = \theta\, r_{ab}$ and the arc length of one AP control volume, $S_{ab,seg}$, we can evaluate the number of AP control volumes with a central angle $\theta$ as

$$N_{GC-AP}^{CV} = \frac{S_{ab,tot}}{S_{ab,seg}} = \frac{\theta\, r_{ab}}{\theta_{seg}\, r_{ab}} = \frac{2\cos^{-1}(r_{ab}/r_{HM})}{\theta_{seg}}. \tag{I.10}$$

## 2. The view factor from HM to HM

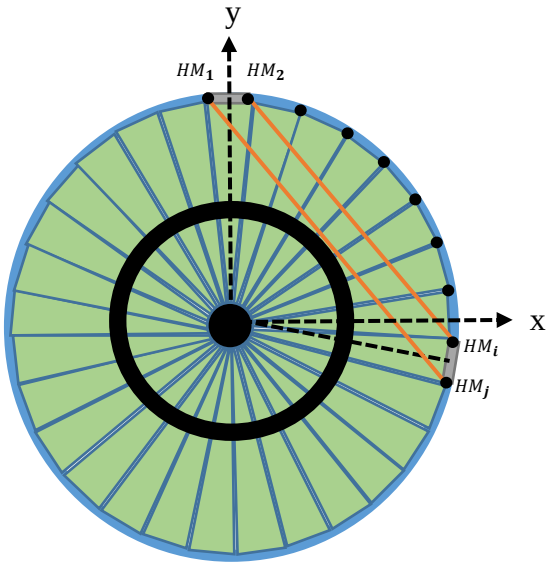


Figure I.5: Description of the view factor from the HM control volume to HM control volume in a cross-section of the receiver unit.

Similar to the above section. By using Eq. I.1 for the situation in Figure I.5, the view factor from the HM control volume to HM control volume can be written as

$$\sum_{ij} F_{A_1A_2,HM_iHM_j} = \frac{(|HM_1-HM_i|+|HM_2-HM_j|)-(|HM_1-HM_j|+|HM_2-HM_i|)}{2\times r_{HM,in}\times\theta_{CV}}, \quad \text{(I.11)}$$

where $r_{HM,in}$ is the inner radius of the HM cover, and the other symbols are shown in Fig. I.5. The summation in Eq. (I.11) continues until the $HM_i$ makes an angle $0^{\circ}$ with respect to X-axis. This method will help us to get the number of HM control volumes that are going to be in thermal contact with one HM control volume. There is also, another way to confirm these number of the HM control volumes, which is discussed in the following section.

## 2.1. The number of the HM segments or control volumes (CVs) that are in thermal contact with other HM segment

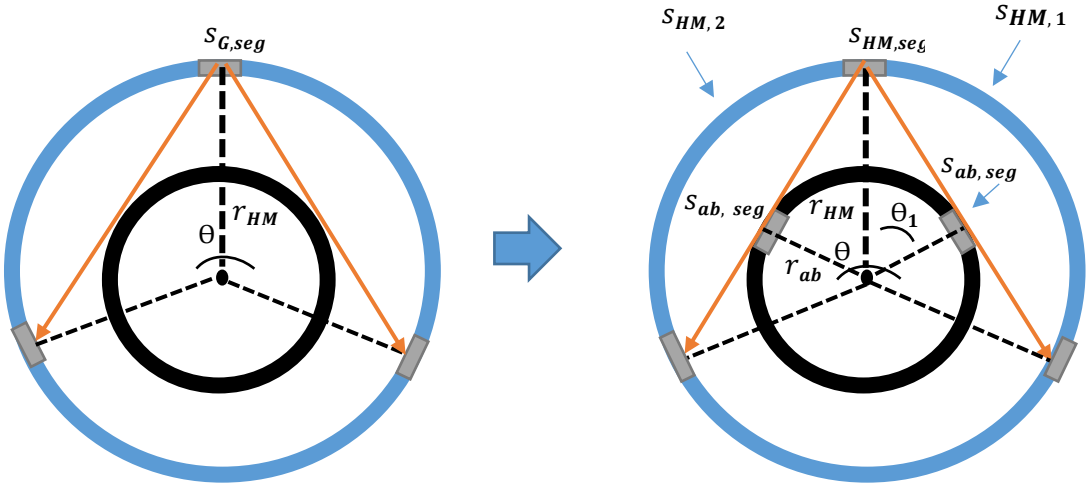



Figure I.6: Graphical representation for the maximum reflection from HM control volume to HM control volume

The real representation of the maximum radiation reflected from HM control volume to HM control volume is shown on the left of Figure I.6, the extreme rays from HM control volume to HM control volume should not touch the AP. If this reflected radiation touches the AP in its way instead of HM control volume, this reflection will count as an interaction from AP to HM or vice versa. On the right of Figure I.6, the extreme rays are allowed to touch the AP for the purpose of simplifying the calculations. The calculation starts by evaluating $\theta$, where $\theta = 4\theta_1$ and $\Theta_1 = \cos^{-1}\frac{r_{ab}}{r_{HM}}$.

The total arc length that has the central angle $\theta$ equals $s_{HM,1} + s_{HM,2}$. The number of HM control volumes segments that can be affected due to the thermal radiation from other HM control volume segment $= \frac{S_{HM,1}+S_{HM,2}}{S_{G,seg}} = \frac{4\,\Theta_1\,r_{HM}}{\Theta_{seg}\,r_{HM}} = \frac{4\,\cos^{-1}\frac{r_{ab}}{r_{HM}}}{\Theta_{seg}}$.

# Appendix III

## Calculating the cavity opening sizes

Calculating the cavity opening sizes is started by using the design parameters of SEGS LS2 (Table 7-1). The design parameters that are going to be used in these calculations are

- Collector aperture = 5 m.
- Glass external diameter ($D_{HM}$) = 0.115 m, the radius ($r_{HM}$) = 5.75 cm.

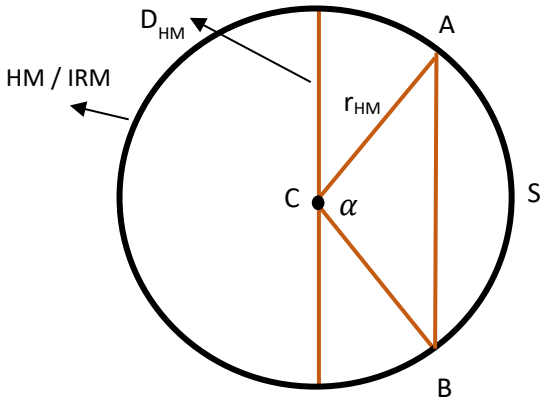



Figure II.1: chord length and arc length for the cavity opening.

From the trigonometry, the arc length *S* is defined as

$$S = \pi\, r_g \left(\frac{\alpha^{\circ}}{180^{\circ}}\right), \tag{II.1}$$

and the chord *AB* is defined as

$$AB = 2r_g \sin\left(\frac{\alpha}{2}\right). \tag{II.2}$$

The symbols in Eq.(II.1) and Eq.(II.2) are defined in Figure II.1. The minimum cavity opening is related to the maximum concentration ration of the Parabolic Mirror Trough. According to the study done by [126] and by the aid of Figure II.2, the maximum limit of the concentration ratio of the parabolic mirror by its own is calculated from $\frac{m}{CD} = 107$ for $\emptyset = 45^{\circ}$, where m is the half of the aperture width of the parabolic mirror, *CD* is the half of the line width. These parameters are defined in Figure II.2.

For the cavity case, the minimum cavity opening width can be deduced from the principle mentioned above. In Figure II.2, *CD* is the same as the cord AB/*2* in Figure II.1. The minimum length of $AB_{min}$ is associated with the

maximum concentration ratio, which can be written as $\frac{AB_{min}}{2} = \frac{m}{107} = \frac{2.5\,m}{107}$ = 2.33 cm. Therefore, the minimum focal line width for the maximum concentration ration is $AB_{min}$ = 4.66 cm. The arc length *S*, which is corresponding to this value, can be evaluated by using Eq. II.1 and Eq. II.2. as follows

$$\alpha = 2\ \sin^{-1}\left(\frac{AB_{min}}{2r_g}\right) = 47.9^{\circ}, \tag{II.3}$$

$$S_{min} = 2\pi\ r_g\left(\frac{\alpha}{360^{\circ}}\right) = 4.8\ cm. \tag{II.4}$$

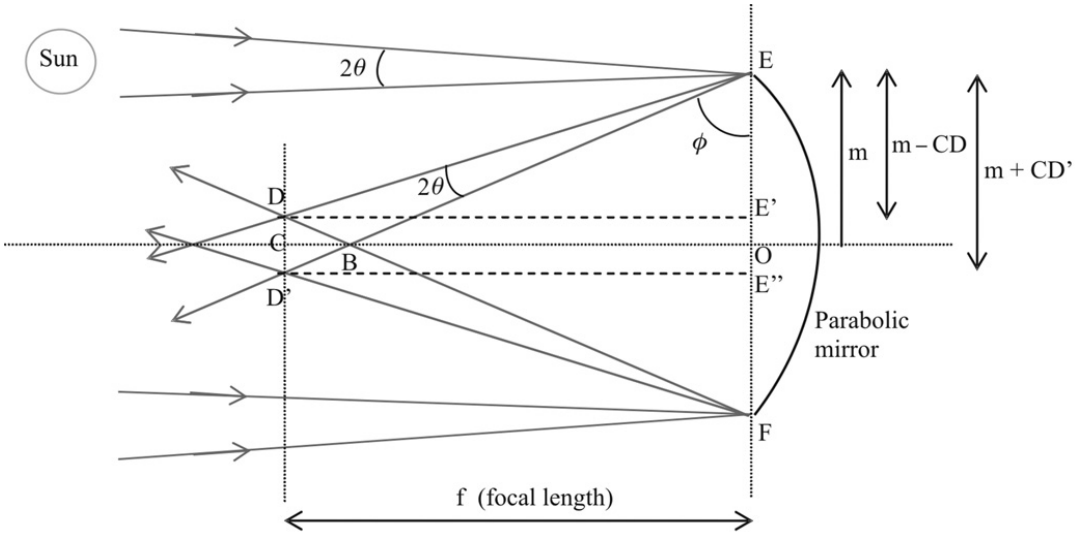



Figure II.2: Ray diagram of the light rays reflection of the parabolic trough mirror [126]

The number of control volumes (CVs) that occupied the arc length *S* equals ~ 13 CVs ($\frac{\alpha_{min}}{CV_{angle}} = \frac{47.9^{\circ}}{3.6^{\circ}} = 13.3$ CVs), where $CV_{angle}$ is the central angle of each CV since we discretized the circumference into 100 CVs.
For the study purpose (as explained in Chapter 7), four cavity opening sizes were selected to examine the effect of the cavity opening on the efficiency of the system and the HTF temperature. The four cavity opening are

1) 50 CVs with a central angle $\alpha_{50CVs} = 3.6 * 50 = 180^{\circ}$ and its arc length $S_{50CVs} = 2\pi r_g\left(\frac{180^{\circ}}{360^{\circ}}\right) \sim 18$ cm.
2) 35 CVs with a central angle $\alpha_{35CVs} = 3.6 * 35 = 126^{\circ}$ and its arc length $S_{35CVs} = 2\pi r_g\left(\frac{126^{\circ}}{360^{\circ}}\right) \sim 12.6$ cm.
3) 25 CVs with a central angle $\alpha_{25CVs} = 3.6 * 25 = 90^{\circ}$ and its arc length $S_{25CVs} = 2\pi r_g\left(\frac{90^{\circ}}{360^{\circ}}\right) \sim 9$ cm.
4) 15 CVs with a central angle $\alpha_{15CVs} = 3.6 * 15 = 54^{\circ}$ and its arc length $S_{15CVs} = 2\pi r_g\left(\frac{54^{\circ}}{360^{\circ}}\right) \sim 5.4$ cm.

In the case of discretized the circumference into 200 CVs. The four cavity opening will have the following sizes, see chapter 4 for more details:

1) 100 CVs with a central angle $\alpha_{100CVs} = 1.8 * 100 = 180^{\circ}$ and its arc length $S_{100CVs} = 2\pi r_g\left(\frac{180^{\circ}}{360^{\circ}}\right) \sim 18$ cm.

2) 70 CVs with a central angle $\alpha_{70CVs} = 1.8 * 70 = \ 126^{\circ}$ and its arc length $S_{70CVs} = 2\pi r_g \left(\frac{126^{\circ}}{360^{\circ}}\right) \sim 12.6$ cm.

3) 50 CVs with a central angle $\alpha_{50CVs} = 1.8 * 50 = \ 90^{\circ}$ and its arc length $S_{50CVs} = 2\pi r_g \left(\frac{90^{\circ}}{360^{\circ}}\right) \sim 9$ cm.

4) 30 CVs with a central angle $\alpha_{30CVs} = 1.8 * 30 = \ 54^{\circ}$ and its arc length $S_{30CVs} = 2\pi r_g \left(\frac{54^{\circ}}{360^{\circ}}\right) \sim 5.4$ cm

# Appendix IV

# Simulation codes

In this work, there are two simulation codes that are written in Python. The first code is the outdoor simulation, which simulates the normal operation of the Parabolic Trough Collector (PTC) using solar radiation. The second code is for the indoor simulation, which simulates the receiver of the PTC that operates with heating elements as discussed in Chapter 5. The simulation algorithms for outdoor and indoor systems are summarized in Figure 6-1 and Figure 6-2.

## 1. Outdoor simulation code

The code consists of a series of combined files. These files are presented in the following sections.

### 1.1. The main file for starting the simulation code program

```
################The main file for starting the simulation code program #######
#Packages
import numpy as np
import input as inp
import pandas as pd
import AP_GC_fun as fun1
import fun2
#############################################################################################
num_unit_length= 100 #Total length of the Receiver unit
Iteration = 250      # Iteration number for accuracy
#############################################################################################
''''' define the output lists for the final results '''
T_f = [inp.T_fin]
Q_conv_HTF = []     #HTF heat gain
Ts = [[] for _ in range(num_unit_length)] # inner surface temperature of the absorber pipe
#intialize the first row of Ta and Tg
Ta = [[] for _ in range(num_unit_length+1)]  # The temperature of the outer surface of the absorber pipe
Tg = [[] for _ in range(num_unit_length+1)]  # The temperature of the outer surface of the glass cover
Ta[0].append(np.full(inp.AP_seg_no, inp.T_fin, dtype=np.float64))
Tg[0].append(np.full(inp.GC_seg_no, inp.T_amb, dtype=np.float64))
#############################################################################################
'''''The head function for the simulation'''
def starter():
    print ("The calculations have been started...Proceeding...")
    for It in range(num_unit_length):           #Iteration along the RU lenght
        Alist, Glist = Iter_ab(Iteration, It)   # calling the function that is iterate the solution of Ta and Tg
        np.seterr(over='raise')
        j = Iteration - 1                       #Parameter that define the last element of the iteration
## Way to insert the Ta and Tg profile temperatures that is obtained from functions Glist and Alist at each length of RU in
        Tgs = []
        Tas = []
        for i in range(inp.AP_seg_no):
            Tas.append(Alist[j][i][0])
        Ta[It+1].append(Tas)
```

```
        for k in range(inp.GC_seg_no):
            Tgs.append(Glist[j][k][0])
        Tg[It+1].append(Tgs)
#Way to calculate the final values that can be obtained from Ta and Tg
        Ts1 = (inp.k_ab*(np.array(Ta[It+1], dtype=np.float64)) + inp.h_f*inp.dt_ab*T_f[It])/(inp.k_ab + inp.h_f*inp.dt_ab)
        Qconv_CV = inp.h_f*inp.dA_ab_i*(Ts1 - T_f[It]) #It calculates Q HTF gain for each element inside the list[Seg. number]
        Qconv = np.sum(Qconv_CV)                       #Sum the all Q HTF for each segment arounf the cicumference
        Q_conv_HTF.append(Qconv)                       #Append the Q HTF for the whole dL lenght in one list
        T_fout = (Qconv/(inp.m*inp.Cp)) + T_f[It]      #Calculating the outlet temperature at each dL
        T_f.append(T_fout)
        print ("Unit length number : "+str(It)+ " Outlet Temperature : "+str(T_f[It])+" HTF Heat Gain : "+str(Q_conv_HTF[It]))
        print()
#Wrtite the results in an excel file
    writer = pd.ExcelWriter('with_Bare_8th100m_alpab_vis86_rho_g_alphg.xlsx')
    df1 = pd.DataFrame({'HTF Temp.':T_f})
    df2 = pd.DataFrame({'Q_htf_cv':Q_conv_HTF})
    df3 = pd.DataFrame({'Tg10':Tg[10][0], 'Tg20':Tg[20][0], 'Tg30':Tg[30][0], 'Tg40':Tg[40][0], 'Tg50':Tg[50][0], 'Tg60':Tg[60][0], 'Tg70':Tg[70][0], 'Tg80':Tg[80][0], 'Tg90':Tg[90][0], 'Tg100':Tg[100][0]})
    df4 = pd.DataFrame({'Ta10':Ta[10][0], 'Ta20':Ta[20][0], 'Ta30':Ta[30][0], 'Ta40':Ta[40][0], 'Ta50':Ta[50][0], 'Ta60':Ta[60][0], 'Ta70':Ta[70][0], 'Ta80':Ta[80][0], 'Ta90':Ta[90][0], 'Ta100':Ta[100][0]})

    df1.to_excel(writer, 'HTF', index = True)
    df2.to_excel(writer, 'QHTF', index = True)
    df3.to_excel(writer, 'Tg', index = True)
    df4.to_excel(writer, 'Ta', index = True)
    writer.save()

    print("Fluid temperatures "+str(T_f))
    print()
    print("HTF heat gain "+str(Q_conv_HTF))
    print()
################################################################################################
'''''Building the Itration matrix for the calculation [ [ [0, 0, Ta], ....[CV numbers].... ]]'''
def Int_iter_Ta_matrix(Iteration, It):
    A0 = [[[] for _ in range(inp.AP_seg_no)] for _ in range(1)]           #Each list represents one iteration and include AP segments
    for i in range(inp.AP_seg_no):
        A0[0][i].append(Ta[It][0][i])
    A = [[[] for _ in range(inp.AP_seg_no)] for _ in range(Iteration - 1)]#Increase the size of the matrix in order to fit the specified number of Iteration.
    Alist = A0 + A
    return Alist
################################################################################################
def Int_iter_Tg_matrix(Iteration, It):
    G0 = [[[] for _ in range(inp.GC_seg_no)] for _ in range(1)] # Each list represents one iteration and include AP segments
    for i in range(inp.GC_seg_no):
        G0[0][i].append(Tg[It][0][i])
    G = [[[] for _ in range(inp.GC_seg_no)] for _ in range(Iteration - 1)]  # Increase the size of the matrix in order to fit the specified number of Iteration.
    Glist = G0 + G
    return Glist
################################################################################
VF_sky = fun2.VF_sky_GC()   #Calling view factor function from GC to sky
VF_AG = fun2.VF_AG()        #Calling view factor function from AP to GC
```

```
coeff_ab = (inp.k_ab*inp.dt_ab*inp.dl)/(inp.r_ab_m*inp.AP_seg_rad) #discretization coff. for AP
coeff_GC = (inp.k_g*inp.dt_g*inp.dl)/(inp.r_g_m*inp.GC_seg_rad)    #discretization coff. for GC
#################################################################
'''''The main calculation to fill the Iteration matrix  '''
def Iter_ab(Iteration, It):
    Alist = Int_iter_Ta_matrix(Iteration, It)
    Glist = Int_iter_Tg_matrix(Iteration, It)
    #count = 0
    for j in range(1, Iteration):
        for i in range (inp.AP_seg_no):
            Ref1 = fun1.Ref1(i, j, Alist)  #Calling reflection functions
            Ref2 = fun1.Ref2(i, j, Alist)
            GA_emis = fun1.GA_emis(i, j, Glist)

            a_ab = (2*inp.k_ab*inp.dt_ab*inp.dl)/(inp.r_ab_m*inp.AP_seg_rad) + inp.h_f*inp.dA_ab_i \
            + (4*inp.segma*inp.epislon_ab*inp.dA_ab_o*(1 + inp.rho_abir*inp.rho_G[2*i]*VF_AG[0]*(sum(VF_AG) - VF_AG[0])))*(Alist[j-1][i][0]**3) - (1-inp.rho_abir) \
                    *(4*inp.segma*inp.epislon_ab*inp.dA_ab_o*(inp.rho_G[2*i]*VF_AG[0] + (inp.rho_G[2*i]**2)*inp.rho_abir*(VF_AG[0]**2))*(Alist[j-1][i][0]**3)) #may be we need to include xa[i]

                    b_ab = inp.alph_abvis*inp.tau_g_up*fun2.AP_sol()[i]*inp.dA_ab_o + inp.h_f*inp.dA_ab_i*T_f[It] \
                    + (3*inp.epislon_ab*inp.segma*inp.dA_ab_o*(1 + inp.rho_abir*inp.rho_G[2*i]*VF_AG[0]*(sum(VF_AG) - VF_AG[0])))*(Alist[j-1][i][0]**4) - (1-inp.rho_abir)*(3*inp.segma*inp.epislon_ab*inp.dA_ab_o*(inp.rho_G[2*i]*VF_AG[0] + (inp.rho_G[2*i]**2)*inp.rho_abir*(VF_AG[0]**2)))*(Alist[j-1][i][0]**4) \
                    + (1-inp.rho_abir)*(inp.epislon_ab*inp.segma*inp.dA_ab_o)*(Ref1 + Ref2) \
                    + (1-inp.rho_abir)*inp.segma*inp.dA_g_i*(GA_emis)

                    if i == inp.AP_seg_no - 1:
                        T_a = (coeff_ab*Alist[j-1][0][0]+coeff_ab*Alist[j-1][i-1][0] + b_ab)/ a_ab
                    elif i == 0:
                        T_a = (coeff_ab*Alist[j-1][i+1][0]+coeff_ab*Alist[j-1][inp.AP_seg_no - 1][0] + b_ab)/ a_ab
                    else:
                        T_a = (coeff_ab*Alist[j-1][i+1][0]+coeff_ab*Alist[j-1][i-1][0] + b_ab)/ a_ab

                    Alist[j][i].append(T_a)

                for i in range (inp.GC_seg_no):
                    GC_1Ref = fun1.GC_1ref(i, j, Alist) #Calling reflection functions
                    GC_2Ref = fun1.GC_2ref(i, j, Alist)
                    GG_emis = fun1.GG_emis(i, j, Glist)

                    a_g = (2*inp.k_g*inp.dt_g*inp.dl)/(inp.r_g_m*inp.GC_seg_rad) + inp.h_g*inp.dA_g_o + 4*inp.segma*(inp.epislon_Gi[i]*inp.dA_g_i + inp.epislon_Go[i]*inp.dA_g_o)*(Glist[j-1][i][0]**3)

                    if i < 50 and i > 149:
                        b_g = 0.025*fun2.GC_sol()[i]*inp.dA_g_o + 3*inp.segma*(inp.epislon_Gi[i]*inp.dA_g_i + inp.epislon_Go[i]*inp.dA_g_o)*(Glist[j-1][i][0]**4) \
                        + inp.h_g*inp.dA_g_o*inp.T_amb + inp.epislon_Go[i]*inp.segma*inp.dA_g_o*(inp.T_sky**4) + (inp.segma*inp.epislon_ab*inp.dA_ab_o)*(GC_1Ref + GC_2Ref) + inp.epislon_Gi[i]*inp.segma*inp.dA_g_i*GG_emis
                    else:
                        b_g = 0.025*fun2.GC_sol()[i]*inp.dA_g_o + 3*inp.segma*(inp.epislon_Gi[i]*inp.dA_g_i + inp.epislon_Go[i]*inp.dA_g_o)*(Glist[j-1][i][0]**4) \
```

```
                        + inp.h_g*inp.dA_g_o*inp.T_amb + inp.epislon_Go[i]*inp.segma
    *inp.dA_g_o*(inp.T_amb**4) + (inp.segma*inp.epislon_ab*inp.dA_ab_o)*(GC_1Ref + GC_2
    Ref) + inp.epislon_Gi[i]*inp.segma*inp.dA_g_i*GG_emis

                    if i == inp.GC_seg_no - 1:
                        T_g = (coeff_GC*Glist[j-1][0][0] + coeff_GC*Glist[j-1][i-
    1][0] + b_g)/ a_g
                    elif i == 0:
                        T_g = (coeff_GC*Glist[j-1][i+1][0] + coeff_GC*Glist[j-
    1][(inp.GC_seg_no - 1)][0] + b_g)/ a_g
                    else:
                        T_g = (coeff_GC*Glist[j-1][i+1][0] + coeff_GC*Glist[j-1][i-
    1][0] + b_g)/ a_g

                    Glist[j][i].append(T_g)

            return Alist, Glist
        ##############################################################################
```

### 1.2. Input file

```
#########################################Input file#################################
#packages
import numpy as np
'''''      discretization   '''
AP_seg_no = 100
GC_seg_no = AP_seg_no*2
AP_seg_ang = 360.0/AP_seg_no
GC_seg_ang = 360.0/GC_seg_no        #segment size in angle from the center of the p
ipe
AP_seg_rad = AP_seg_ang/180*np.pi
GC_seg_rad = GC_seg_ang/180*np.pi   #segement size in radian
dl = 1       # unit length of the AP and GC

'''''           Heat Transfer Fluid   '''
T_fin = 763.459869   # HTF is molten salt
T_amb = 294.35
T_sky = T_amb - 8
m = 0.68

''''' For molten salt '''
density = 882
k_f = 0.124
Cp = 1711
h_f = 500
visco = 0.00386

'''''      Absorber pipe properties '''
#Physical properties
r_ab_i = 0.066/2
r_ab_o = 0.07/2
dt_ab = r_ab_o - r_ab_i
r_ab_m=(r_ab_o + r_ab_i)/2.0
dA_ab_o=r_ab_o*AP_seg_rad*dl
dA_ab_i=r_ab_i*AP_seg_rad*dl
k_ab = 16.2
#rho_abir = 0.85  #For S.C absorber pipe
rho_abir = 0.14  #For bare or HM absorber pipe
segma = 5.6697e-8
epislon_ab = 1 - rho_abir
#alph_abvis = 0.96  #For S.C absorber pipe
alph_abvis = 0.86   #For bare or HM absorber pipe
```

```
41. 
42. '''''                 Glass Cover   '''
43. #Physical properties
44. r_g_i= 0.109/2
45. r_g_o= 0.115/2
46. dt_g = r_g_o - r_g_i
47. r_g_m= (r_g_o + r_g_i)/2.0
48. dA_g_i= r_g_i*GC_seg_rad*dl
49. dA_g_o= r_g_o*GC_seg_rad*dl
50. k_g = 1.04
51. #### Upper half ####
52. #IR radiaiton    #glass transmissivity in IR is zero
53. rho_gir_up = [0.14]
54. epislon_gi_up = [0.86]
55. epislon_go_up = [0.86]
56. #visible radiation
57. tau_g_up = 0.935      #for bare
58. rho_gvis_up = 0.04
59. alph_gvis_up = 1 - rho_gvis_up - tau_g_up
60. ###lower half ####
61. #IR radiaiton
62. rho_gir_dow = [0.14]  #for bare
63. epislon_gi_dow = [0.86]
64. epislon_go_dow = [0.86]
65. #Visible radiaiton
66. tau_g_dow = 0.935
67. rho_gvis_dow = 0.04
68. alph_gvis_dow = 1 - rho_gvis_dow - tau_g_dow
69. ###############
70. rho_G = rho_gir_up*51 + rho_gir_dow*100 + rho_gir_up*49
71. epislon_Go = epislon_go_up*51 + epislon_go_dow*100 + epislon_go_up*49
72. epislon_Gi = epislon_gi_up*51 + epislon_gi_dow*100 + epislon_gi_up*49
73. ################
74. 
75. ''''' Air outside the glass cover '''
76. v = 2.6 #m/s the speed of wind
77. h_g = h_w = (4*v**0.58)*(2*r_g_o)**(-0.42)  #h_w = 4*v**0.58 * d**-
    0.42 , wher d is the diameter of the glass cover
78. #######Convection parameters ###################################
79. Re = m/(np.pi*visco*r_ab_i**2)
80. Pr =  visco*Cp/k_f
81. Nu = 0.3+((0.62*Re**0.5*Pr**0.3333)/(1+(0.4/Pr)**0.6667)**0.25)*(1+(Re/282000)**0.6
    25)**0.8
82. Rc = 375.3567
83. Beta = 7
84. gamma = 0.40278
```

### 1.3. View factors functions and solar distribution file

```
1.  ####################View factors functions and solar distribution#################
2.  #Packages
3.  import numpy as np
4.  import input as inp
5.  ###################################
6.  '''''Calculating the view factor from AP to GC'''
7.  def VF_AG():
8.      i = 0
9.      alpha = inp.AP_seg_rad/4
10.     VF_AG = []
11.     while (np.pi/2 +alpha + i*(inp.AP_seg_rad/2)) < np.pi:
```

```
        y1 = np.sqrt((inp.r_g_i*np.cos(np.pi/2 + alpha + i*(inp.AP_seg_rad/2)) - inp.r_ab_o*np.cos(np.pi/2 + (inp.AP_seg_rad/2)))**2 + (inp.r_g_i*np.sin(np.pi/2 +alpha + i*(inp.AP_seg_rad/2)) - inp.r_ab_o*np.sin(np.pi/2 + (inp.AP_seg_rad/2)))**2)
        y2 = np.sqrt((inp.r_g_i*np.cos(np.pi/2 - alpha + i*(inp.AP_seg_rad/2)) - inp.r_ab_o*np.cos(np.pi/2 - (inp.AP_seg_rad/2)))**2 + (inp.r_g_i*np.sin(np.pi/2 - alpha + i*(inp.AP_seg_rad/2)) - inp.r_ab_o*np.sin(np.pi/2 - (inp.AP_seg_rad/2)))**2)
        x1 = np.sqrt((inp.r_g_i*np.cos(np.pi/2 + alpha + i*(inp.AP_seg_rad/2)) - inp.r_ab_o*np.cos(np.pi/2 - (inp.AP_seg_rad/2)))**2 + (inp.r_g_i*np.sin(np.pi/2 + alpha + i*(inp.AP_seg_rad/2)) - inp.r_ab_o*np.sin(np.pi/2 - (inp.AP_seg_rad/2)))**2)
        x2 = np.sqrt((inp.r_g_i*np.cos(np.pi/2 - alpha + i*(inp.AP_seg_rad/2)) - inp.r_ab_o*np.cos(np.pi/2 + (inp.AP_seg_rad/2)))**2 + (inp.r_g_i*np.sin(np.pi/2 - alpha + i*(inp.AP_seg_rad/2)) - inp.r_ab_o*np.sin(np.pi/2 + (inp.AP_seg_rad/2)))**2)
        F = ((x1+x2)-(y1+y2))/(2*inp.r_ab_o*inp.AP_seg_rad)
        if F > 0:
            VF_AG.append(F)
            i+=1
        else:
            break
    return VF_AG
##############################################3
'''''Calculating the view factor from GC to GC'''
def VF_GG():
    i = 0
    alpha = inp.AP_seg_rad/4
    VF_GG = []
    while (- alpha + i*(inp.AP_seg_rad/2)) < np.pi/2:
        y1 = np.sqrt((inp.r_g_i*np.cos(-3*alpha + i*(inp.AP_seg_rad/2)) - inp.r_g_i*np.cos(np.pi/2 + alpha))**2 + (inp.r_g_i*np.sin( - 3*alpha + i*(inp.AP_seg_rad/2))- inp.r_g_i*np.sin(np.pi/2 + alpha))**2)

        y2 = np.sqrt((inp.r_g_i*np.cos(- alpha + i*(inp.AP_seg_rad/2)) - inp.r_g_i*np.cos(np.pi/2 - alpha))**2 + (inp.r_g_i*np.sin( - alpha + i*(inp.AP_seg_rad/2))- inp.r_g_i*np.sin(np.pi/2 - alpha))**2)
        x1 = np.sqrt((inp.r_g_i*np.cos(-3*alpha + i*(inp.AP_seg_rad/2)) - inp.r_g_i*np.cos(np.pi/2 - alpha))**2 + (inp.r_g_i*np.sin( - 3*alpha + i*(inp.AP_seg_rad/2))- inp.r_g_i*np.sin(np.pi/2 - alpha))**2)

        x2 = np.sqrt((inp.r_g_i*np.cos(- alpha + i*(inp.AP_seg_rad/2)) - inp.r_g_i*np.cos(np.pi/2 + alpha))**2 + (inp.r_g_i*np.sin( - alpha + i*(inp.AP_seg_rad/2))- inp.r_g_i*np.sin(np.pi/2 + alpha))**2)
        F = ((x1+x2)-(y1+y2))/(2*inp.r_g_i*(inp.GC_seg_rad/2))
        VF_GG.append(F)
#        print (- alpha + i*inp.seg_rad)
        i += 1
    x = VF_GG[::-1]
    return x
########################################################################
'''''Calculating the view factor from sky to GC'''
def VF_sky_GC():
   #y = inp.Rc*np.sin(inp.gamma)
   #x = inp.Rc*np.sin(inp.gamma) + (inp.r_g_o*inp.seg_rad)
   #F = (2*x - 2*y)/(inp.Rc*inp.Beta)
   #F = 0.000473
   F = 1/inp.GC_seg_no
   return F
########################################################################
''''' Concentrated solar flux distribution across the AP '''
def AP_sol():
    S = [993.7, 993.7, 993.7, 993.7, 993.7, 993.7, 993.7, 993.7, 993.7, 993.7, 990, 980, 985, 975, 970, 965, 960,
    955, 950, 948, 945, 940, 938, 936, 2600, 6000, 10000, 12000, 16000, 22000, 26000, 30000, 35000,
    37000, 42000, 48000, 49500, 48000, 47000, 45800, 45000, 44800, 44600, 44200, 44000, 42000, 40000,
    39000, 40000, 40000, 39000, 40000, 42000, 44000, 44200, 44600, 44800, 45000, 45800, 47000, 48000,
```

```
    49500, 48000, 42000, 37000, 35000, 30000, 26000, 22000, 16000, 12000, 10000, 60
00, 2600, 936,
    938, 940, 945, 948, 950, 955, 960, 965, 970, 975, 985, 980, 990, 993.7, 993.7,
993.7, 993.7, 993.7, 993.7,
    993.7, 993.7, 993.7, 993.7, 993.7, 993.7]
    return S
########################################################################
''''' Concentrated solar flux distribution across the GC '''
def GC_sol():
    S = [993.7, 93.7, 993.7, 993.7, 993.7, 993.7, 993.7, 993.7, 993.7, 993.7, 993.7
, 993.7, 993.7, 993.7, 993.7, 993.7, 993.7, 993.7,
    993.7, 993.7, 993.7, 991.85, 990, 985, 980, 982.5, 985, 977.5, 975, 972.5, 970,
 967.5, 965, 962.5, 960, 957.5, 955, 952.5, 950,
    949, 948, 946.5, 945, 942.5, 940, 939, 938, 937, 936, 1768, 2600, 4300, 6000, 8
000, 10000, 11000, 12000, 14000, 16000, 19000,
    22000, 24000, 26000, 28000, 30000, 32500, 35000, 36500, 37000, 39500, 42000, 45
000, 48000, 48750, 49500, 48750, 48000, 47500,
    47000, 46400, 45800, 45400, 45000, 44900, 44800, 44500, 44600, 44100, 44200, 44
100, 44000, 43000, 42000, 41000, 40000, 39500,
    39000, 39500, 40000, 40000, 40000, 39500, 39000, 39500, 40000, 41000, 42000, 43
000, 44000, 44100, 44200, 44400, 44600, 44500,
    44800, 44900, 45000, 45400, 45800, 46400, 47000, 47500, 48000, 48750, 49500, 48
750, 48000, 45000, 42000, 39500, 37000, 36000,
    35000, 32500, 30000, 28000, 26000, 24000, 22000, 19000, 16000, 14000, 12000, 11
000, 10000, 8000, 6000, 4300, 2600, 1768, 936,
    937, 938, 939, 940, 942.5, 945, 946.5, 948, 949, 950, 952.5, 955, 957.5, 960, 9
62.5, 965, 967.5, 970, 972.5, 975, 980, 985, 982.5,
    980, 985, 990, 992, 933.7, 933.7, 933.7, 933.7, 933.7, 933.7, 933.7, 933.7, 933
.7, 933.7, 933.7, 933.7, 933.7, 933.7, 933.7, 933.7,
    933.7, 933.7, 933.7, 933.7, 933.7, 933.7]
    return S

```

### 1.4. Internal emission and reflection functions

```
###################### Interal emission and reflections functions##############
#Packages
import numpy as np
import input as inp
import fun2
#################################################################################
VF_AG = fun2.VF_AG() #View factor from AP to GC
VF_GG = fun2.VF_GG() #View factor from GC to GC
VF_GA = ((inp.r_ab_o**2)/(inp.r_g_i**2))*np.array(fun2.VF_AG()) #View factor from G
C to AP
#################################################################################
''''' The emission from AP to GC'''
def AG_emis(i, k, Alist):
    x = []
    AG_1n, AG_2n, AG_1off, AG_2off  = 0, 0, 0, 0
    if i%2 == 0:
        AG0 = (Alist[k-1][int(i/2)][0]**4)*VF_AG[0]
        for j in range(1, int((len(VF_AG)-1)/2)):
            if (i/2 + j) > inp.AP_seg_no - 1:
                AG_1n += (Alist[k-
1][int(i/2 + j) - inp.AP_seg_no][0]**4)*VF_AG[2*j] + (Alist[k-
1][int(i/2 - j)][0]**4)*VF_AG[2*j]
            else:
                AG_2n += (Alist[k-1][int(i/2 + j)][0]**4)*VF_AG[2*j] + (Alist[k-
1][int(i/2 - j)][0]**4)*VF_AG[2*j]
        x.append(AG_1n + AG_2n + AG0)
            #print(AG_1ref_n, AG_1ref0)
    else:
        for j in range(1, int(len(VF_AG)/2)):
```

```
            if ((i+1)/2 + j) > inp.AP_seg_no - 1:
                AG_1off += (Alist[k-1][int((i+1)/2 + j) - inp.AP_seg_no][0]**4)*VF_AG[int(2*j -1)] + (Alist[k-1][int((i+1)/2 - j)][0]**4)*VF_AG[int(2*j -1)]
            else:
                AG_2off += (Alist[k-1][int((i+1)/2 + j)][0]**4)*VF_AG[int(2*j -1)] + (Alist[k-1][int((i+1)/2 - j)][0]**4)*VF_AG[int(2*j -1)]
        x.append(AG_1off + AG_2off)
    y = sum(x)
    return y
################################################################################
''''' The emission from GC to AP'''
def GA_emis(i, k, Glist): #i is the index number for AP. So that I don't care about offset or normal GC when it comes to this calculations.
    GA1, GA2 = 0, 0
    #if i%2 == 0:         #normal (without off set)
    GA0 =  inp.epislon_Gi[2*i]*VF_GA[0]*(Glist[k-1][2*i][0]**4)
    for j in range(1,len(VF_AG)):
        if 2*i+j > inp.GC_seg_no - 1:
            GA1 += inp.epislon_Gi[(2*i+j)-inp.GC_seg_no]*VF_GA[j]*(Glist[k-1][(2*i+j)-inp.GC_seg_no][0]**4) + inp.epislon_Gi[2*i-j]*VF_GA[j]*(Glist[k-1][2*i-j][0]**4)     #GA_n for normal (without offset position)
        else:
            GA2 += inp.epislon_Gi[2*i+j]*VF_GA[j]*(Glist[k-1][2*i+j][0]**4) + inp.epislon_Gi[2*i-j]*VF_GA[j]*(Glist[k-1][2*i-j][0]**4)
    x = GA0 + GA1 + GA2
    return x
################################################################################
''''' The emission from GC to GC'''
def GG_emis(i, k, Glist):
    GG1, GG2 = 0, 0
    for j in range(len(VF_GG)): #Emissison from GC to GC CV's. According to VF_GG cal. we don't need to start for loop with 1
        if i+j > inp.GC_seg_no - 1:
            GG1 += inp.epislon_Gi[(i+j) - inp.GC_seg_no]*VF_GG[j]*(Glist[k-1][(i+j) - inp.GC_seg_no][0]**4) + inp.epislon_Gi[i-j]*VF_GG[j]*(Glist[k-1][i - j][0]**4)
        else:
            GG2 += inp.epislon_Gi[i+j]*VF_GG[j]*(Glist[k-1][i+j][0]**4) + inp.epislon_Gi[i-j]*VF_GG[j]*(Glist[k-1][i - j][0]**4)
    x = GG1 + GG2
    return x
################################################################################
''''' The radiation due to the view factor from AP to GC and the diffuse reflection from AP to GC '''
''''' Calculating the first reflection via GC '''
def Ref1(i, k, Alist):
    Ref1, Ref2, Ref3, Ref4 = 0,0,0,0
    for j in range(1, len(VF_AG)):
        if (2*i + j > (inp.GC_seg_no - 1)) and (i + j > (inp.AP_seg_no - 1)):
            Ref1 += (Alist[k-1][(i+j)- inp.AP_seg_no][0]**4)*VF_AG[j]*inp.rho_G[(2*i+j)- inp.GC_seg_no] + (Alist[k-1][i - j][0]**4)*VF_AG[j]*inp.rho_G[2*i-j]
        elif i + j > (inp.AP_seg_no - 1):
            Ref2 += (Alist[k-1][(i+j)- inp.AP_seg_no][0]**4)*VF_AG[j]*inp.rho_G[2*i+j] + (Alist[k-1][i - j][0]**4)*VF_AG[j]*inp.rho_G[2*i-j]
        elif 2*i + j > (inp.GC_seg_no - 1):
            Ref3 += (Alist[k-1][i+j][0]**4)*VF_AG[j]*inp.rho_G[(2*i+j)- inp.GC_seg_no] + (Alist[k-1][i - j][0]**4)*VF_AG[j]*inp.rho_G[2*i-j]
        else:
            Ref4 += (Alist[k-1][i+j][0]**4)*VF_AG[j]*inp.rho_G[2*i+j] + (Alist[k-1][i - j][0]**4)*VF_AG[j]*inp.rho_G[2*i-j]
        #xa.append((x + Ref1+ Ref2+ Ref3 + Ref4))
    xa = (Ref1+ Ref2+ Ref3 + Ref4)
```

```
    return xa
################################################################################
''''' Calculating the second reflection via GC '''
def Ref2(i, k, Alist):
    Ref_1R, Ref_2R, Ref_3R, Ref_4R = 0, 0, 0, 0
    Ref_1L, Ref_2L, Ref_3L, Ref_4L = 0, 0, 0, 0
    Ref11, Ref2, Ref3, Ref4 = 0, 0, 0, 0
    for j in range(1, len(VF_AG)):
        if (i + j > (inp.AP_seg_no-1)) and ((2*i + j)>(inp.GC_seg_no-1)):
            Ref_1R += (Alist[k-
1][(i+j)- inp.AP_seg_no][0]**4)*VF_AG[j]*inp.rho_G[(2*i+j)-
inp.GC_seg_no]*inp.rho_abir*inp.rho_G[2*((i+j) - inp.GC_seg_no)]*VF_AG[0] + VF_AG[j
]*inp.rho_G[(2*i+j)-
inp.GC_seg_no]*inp.rho_abir*Ref1(((i+j) - inp.AP_seg_no), k, Alist)
            Ref_1L += (Alist[k-1][i-j][0]**4)*VF_AG[j]*inp.rho_G[2*i-
j]*inp.rho_abir*inp.rho_G[2*(i-j)]*VF_AG[0] + VF_AG[j]*inp.rho_G[2*i-
j]*inp.rho_abir*Ref1((i - j), k, Alist)
            Ref11 = Ref_1R + Ref_1L
        elif i + j > inp.AP_seg_no-1:
            Ref_2R += (Alist[k-
1][(i+j)- inp.AP_seg_no][0]**4)*VF_AG[j]*inp.rho_G[2*i+j]*inp.rho_abir*inp.rho_G[2*
((i+j) - inp.GC_seg_no)]*VF_AG[0] + VF_AG[j]*inp.rho_G[2*i+j]*inp.rho_abir*Ref1(((i
+j) - inp.AP_seg_no), k, Alist)
            Ref_2L += (Alist[k-1][i-j][0]**4)*VF_AG[j]*inp.rho_G[2*i-
j]*inp.rho_abir*inp.rho_G[2*(i-j)]*VF_AG[0] + VF_AG[j]*inp.rho_G[2*i-
j]*inp.rho_abir*Ref1((i - j), k, Alist)
            Ref2 = Ref_2R + Ref_2L
        elif (2*i + j)>inp.GC_seg_no-1:
            Ref_3R += (Alist[k-1][i+j][0]**4)*VF_AG[j]*inp.rho_G[(2*i+j)-
inp.GC_seg_no]*inp.rho_abir*inp.rho_G[2*(i+j)]*VF_AG[0] + VF_AG[j]*inp.rho_G[(2*i+j
)-inp.GC_seg_no]*inp.rho_abir*Ref1((i + j), k, Alist)
            Ref_3L += (Alist[k-1][i-j][0]**4)*VF_AG[j]*inp.rho_G[2*i-
j]*inp.rho_abir*inp.rho_G[2*(i-j)]*VF_AG[0] + VF_AG[j]*inp.rho_G[2*i-
j]*inp.rho_abir*Ref1((i - j), k, Alist)
            Ref3 = Ref_3R + Ref_3L

        else:
            Ref_4R += (Alist[k-
1][i+j][0]**4)*VF_AG[j]*inp.rho_G[2*i+j]*inp.rho_abir*inp.rho_G[2*(i+j)]*VF_AG[0] +
 VF_AG[j]*inp.rho_G[2*i+j]*inp.rho_abir*Ref1((i + j), k, Alist)
            Ref_4L += (Alist[k-1][i-j][0]**4)*VF_AG[j]*inp.rho_G[2*i-
j]*inp.rho_abir*inp.rho_G[2*(i-j)]*VF_AG[0] + VF_AG[j]*inp.rho_G[2*i-
j]*inp.rho_abir*Ref1((i - j), k, Alist)
            Ref4 = Ref_4R + Ref_4L
    y = Ref11 + Ref2 + Ref3 + Ref4
    return y
        ################################################################################
        ''''' Calculating the first reflection via AP '''
        def GC_1ref(i, k, Alist):
            GC_1ref = []
            AG_1ref_1n, AG_1ref_2n, AG_1ref_1off, AG_1ref_2off  = 0, 0, 0, 0
            if i%2 == 0:
                AG_1ref0 = (1-inp.rho_G[i])*(Alist[k-1][int(i/2)][0]**4)*VF_AG[0]
                for j in range(1, int((len(VF_AG)-1)/2)):
                    if (i/2 + j) > inp.AP_seg_no - 1:
                        AG_1ref_1n += (1-inp.rho_G[i])*((Alist[k-
1][int(i/2 + j) - inp.AP_seg_no][0]**4)*VF_AG[2*j] + (Alist[k-
1][int(i/2 - j)][0]**4)*VF_AG[2*j])
                    else:
                        AG_1ref_2n += (1-inp.rho_G[i])*((Alist[k-
1][int(i/2 + j)][0]**4)*VF_AG[2*j] + (Alist[k-1][int(i/2 - j)][0]**4)*VF_AG[2*j])
                GC_1ref.append(AG_1ref_1n + AG_1ref_2n + AG_1ref0)
            else:
                for j in range(1, int(len(VF_AG)/2)):
                    if ((i+1)/2 + j) > inp.AP_seg_no - 1:
```

```
                        AG_1ref_1off += (1-inp.rho_G[i])*((Alist[k-
    1][int((i+1)/2 + j) - inp.AP_seg_no][0]**4)*VF_AG[int(2*j -1)] + (Alist[k-
    1][int((i+1)/2 - j)][0]**4)*VF_AG[int(2*j -1)])
                    else:
                        AG_1ref_2off += (1-inp.rho_G[i])*((Alist[k-
    1][int((i+1)/2 + j)][0]**4)*VF_AG[int(2*j -1)] + (Alist[k-
    1][int((i+1)/2 - j)][0]**4)*VF_AG[int(2*j -1)])
                GC_1ref.append(AG_1ref_1off + AG_1ref_2off)
            GC_ref = sum(GC_1ref)
            return GC_ref
        ###############################################################################
        ''''' Calculating the second reflection via AP '''
        def GC_2ref(i, k, Alist):
            GC_2ref = []
            AG_2ref_n_1R, AG_2ref_n_1L, AG_2ref_off_1R, AG_2ref_off_1L = 0, 0, 0, 0

            AG_2ref_n_2R, AG_2ref_n_2L, AG_2ref_off_2R, AG_2ref_off_2L = 0, 0, 0, 0

            x, y = 0, 0
            if i%2 == 0:
                AG_2ref0 = (1-inp.rho_G[i])*(Alist[k-
    1][int(i/2)][0]**4)*(VF_AG[0]**2)*inp.rho_abir*inp.rho_G[i]
                for j in range(1, int((len(VF_AG)-1)/2)):
                    if (i/2 + j) > inp.AP_seg_no - 1:
                        AG_2ref_n_1R += (1-inp.rho_G[i])*((Alist[k-
    1][int(i/2 + j) - inp.AP_seg_no][0]**4)*VF_AG[2*j]*inp.rho_abir*inp.rho_G[2*(int(i/
    2 + j) - inp.AP_seg_no)]*VF_AG[0] + VF_AG[2*j]*inp.rho_abir*Ref1((int(i/2 + j) - in
    p.AP_seg_no), k, Alist))
                        AG_2ref_n_1L += (1-inp.rho_G[i])*((Alist[k-
    1][int(i/2 - j)][0]**4)*VF_AG[2*j]*inp.rho_abir*inp.rho_G[2*int(i/2 - j)]*VF_AG[0]
    + VF_AG[2*j]*inp.rho_abir*Ref1((int(i/2 - j)), k, Alist))
                        x  = AG_2ref_n_1R + AG_2ref_n_1L
                    else:
                        AG_2ref_n_2R += (1-inp.rho_G[i])*((Alist[k-
    1][int(i/2 + j)][0]**4)*VF_AG[2*j]*inp.rho_abir*inp.rho_G[2*int(i/2 + j)]*VF_AG[0]
    + VF_AG[2*j]*inp.rho_abir*Ref1((int(i/2 + j)), k, Alist))
                        AG_2ref_n_2L += (1-inp.rho_G[i])*((Alist[k-
    1][int(i/2 - j)][0]**4)*VF_AG[2*j]*inp.rho_abir*inp.rho_G[2*int(i/2 - j)]*VF_AG[0]
    + VF_AG[2*j]*inp.rho_abir*Ref1((int(i/2 - j)), k, Alist))
                        y =  AG_2ref_n_2R + AG_2ref_n_2L
                GC_2ref.append((x+y+AG_2ref0))
            else:
                for j in range(1, int(len(VF_AG)/2)):
                    if ((i+1)/2 + j) > inp.AP_seg_no - 1:
                        AG_2ref_off_1R += (1-inp.rho_G[i])*((Alist[k-
    1][int((i+1)/2 + j) - inp.AP_seg_no][0]**4)*VF_AG[int(2*j -
    1)]*inp.rho_abir*inp.rho_G[2*(int((i+1)/2 + j) - inp.AP_seg_no)]*VF_AG[0] + VF_AG[i
    nt(2*j -1)]*inp.rho_abir*Ref1((int((i+1)/2 + j) - inp.AP_seg_no), k, Alist))
                        AG_2ref_off_1L += (1-inp.rho_G[i])*((Alist[k-
    1][int((i+1)/2 - j)][0]**4)*VF_AG[int(2*j -
    1)]*inp.rho_abir*inp.rho_G[2*int((i+1)/2 - j)]*VF_AG[0] + VF_AG[int(2*j -
    1)]*inp.rho_abir*Ref1((int((i+1)/2 - j)), k, Alist))
                        x = AG_2ref_off_1R + AG_2ref_off_1L
                    else:
                        AG_2ref_off_2R += (1-inp.rho_G[i])*((Alist[k-
    1][int((i+1)/2 + j)][0]**4)*VF_AG[int(2*j -
    1)]*inp.rho_abir*inp.rho_G[2*int((i+1)/2 + j)]*VF_AG[0] + VF_AG[int(2*j -
    1)]*inp.rho_abir*Ref1((int((i+1)/2 + j)), k, Alist))
                        AG_2ref_off_2L += (1-inp.rho_G[i])*((Alist[k-
    1][int((i+1)/2 - j)][0]**4)*VF_AG[int(2*j -
    1)]*inp.rho_abir*inp.rho_G[2*int((i+1)/2 - j)]*VF_AG[0] + VF_AG[int(2*j -
    1)]*inp.rho_abir*Ref1((int((i+1)/2 - j)), k, Alist))
                        y = AG_2ref_off_2R + AG_2ref_off_2L
                GC_2ref.append(x+y)
            GC_ref = sum(GC_2ref)
            return GC_ref
```

```
154.       ###########################################################################
```

## 2. Indoor simulation code

The indoor simulation code is also a series of combined files. Mainly, the differences between the indoor and the outdoor simulations are the input parameters and the main body of the simulation program. The view factors, emissions, and internal functions are the same.

### 2.1. The main file for starting the simulation code program

```
1.  ################## The main file for starting the simulation code program ########
2.  #Packages
3.  import numpy as np
4.  import input as inp
5.  import AP_GC_fun as fun1
6.  import fun2
7.  ###############################################################################
8.  T_amb = 298.15  #Ambient temperature
9.  #Heating element power
10. Power = np.array([19.28502277, 35.66043158, 55.08913468, 80.43396226, 109.633702, 1
    39.4933854,
11.                   179.9872045, 223.427673, 262.4159618, 362.0177836, 434.2279332, 4
    90.5695077])
12. Eng = Power/(inp.Length*inp.r_ab_o*2*np.pi)
13. ###############################################################################
14. '''''The calculation for the outer cover of the receiver'''
15. def GC_amb(H_g):
16.     err1, err2 = 1, 1
17.     T_4 = T_amb + 1
18.     while err1 > 0.0001:
19.         T_4 += 0.001
20.         Tavg_g = (T_amb + T_4)/2
21.         beta_g = 1/Tavg_g
22.         Ra_g = (9.8*beta_g*(T_4 - T_amb)*inp.pr_g*((2*inp.r_g_o)**3))/(inp.meu_g**2
    ) # Raleigh Number
23.         Nu = ((0.387*Ra_g**(1/6))/((1+(0.559/inp.pr_g)**(9/16))**(8/27)))**2
24.         h_o = (inp.k_a_G*Nu)/(2*inp.r_g_o)
25.         Q_o_g_conv = h_o*inp.A_g_o*(T_4 - T_amb)
26.         Q_o_g_rad = inp.epislon_Go[0]*inp.segma*inp.A_g_o*(T_4**4 - T_sky**4)
27.         Q_g_amb = Q_o_g_conv + Q_o_g_rad       #W
28.         err1 = (H_g - Q_g_amb)/H_g
29.     T_3 = T_4
30.     while err2 > 0.0001:
31.         T_3 += 0.001
32.         R_g_cond= (np.log(inp.r_g_o/inp.r_g_i))/(2*np.pi*inp.k_g*inp.dl)
33.         Q_g_cond= (T_3 - T_4)/R_g_cond
34.         err2 = (H_g - Q_g_cond)/H_g
35.     Tg_o = [T_4]*inp.GC_seg_no
36.     Tg_i = [T_3]*inp.GC_seg_no
37.     return Tg_i, Tg_o
38. ###############################################################################
39. '''''The calculation for the absorber pipe of the receiver'''
40. def AP_GC():
41.     print("At an ambient temperature = "+str(T_amb)+" K = "+str(T_amb -
    273.15)+" C and Ref. = "+str(inp.rho_gir_dow[0]))
42.     VF_AG = fun2.VF_AG() #Callig the view factor function from AP to GC
43.     for j in range(len(Power)):
44.         e = 1
```

```
        Glist, Tg_o = GC_amb(Power[j])
        Alist = [Glist[0] + 1]*inp.AP_seg_no
        while e > 0.0001:
            Alist = [Alist[0]+ 0.01]*inp.AP_seg_no
            b = []
            for i in range (inp.AP_seg_no):
                GA_emis = fun1.GA_emis(i, Glist)
                Ref1 = fun1.Ref1(i, Alist) #Callig the first reflections unction
                Ref2 = fun1.Ref2(i, Alist) #Callig the second reflections unction

                b_ab = (inp.epislon_ab*inp.segma*inp.dA_ab_o)*(1 + inp.rho_abir*inp.rho_G[2*i]*VF_AG[0]*(sum(VF_AG) - VF_AG[0]))*(Alist[i]**4) - (1-inp.rho_abir)*inp.segma*inp.dA_g_i*(GA_emis) \
                    - (1-inp.rho_abir)*(inp.segma*inp.epislon_ab*inp.dA_ab_o*(inp.rho_G[2*i]*VF_AG[0] + (inp.rho_G[2*i]**2)*inp.rho_abir*(VF_AG[0]**2))*(Alist[i]**4)) \
                    - (1-inp.rho_abir)*(inp.epislon_ab*inp.segma*inp.dA_ab_o)*(Ref1 + Ref2)
                b.append(b_ab)
            e = ((Eng[j]*inp.dA_ab_o) - b[10])/(Eng[j]*inp.dA_ab_o)
        print()
        print("At heating power "+str(Power[j])+" : AP Temp."+str(Alist[10] - 273.15)+" C and GC inside Temp."+str(Glist[10] - 273.15)+" C and GC outside Temp "+str(Tg_o[10]-273.15))
################################################################################
```

## 2.2. The input file

```
##############################Input file##################################################
#Package
import numpy as np
###########################################################################################
'''''      discretization   '''
AP_seg_no = 100                    #Number of AP segements
GC_seg_no = AP_seg_no*2            #Number of AP segements
AP_seg_ang = 360.0/AP_seg_no
GC_seg_ang = 360.0/GC_seg_no       #segment size in angle from the center of the pipe
AP_seg_rad = AP_seg_ang/180*np.pi
GC_seg_rad = GC_seg_ang/180*np.pi #segement size in radian
N_CV = 3                           # Number of CV along the length
Length = 3                         # RU length
dl = 2.65
###########################################################################################
'''''      Absorber pipe properties '''
#Physical properties
r_ab_i = 0.028/2
r_ab_o = 0.032/2
dt_ab = r_ab_o - r_ab_i
r_ab_m=(r_ab_o + r_ab_i)/2.0
dA_ab_o=r_ab_o*AP_seg_rad*dl
A_ab_o = 2*r_ab_o*np.pi*dl
dA_ab_i=r_ab_i*AP_seg_rad*dl
k_ab = 50.2
rho_abir = 0.32              #For bare absorber pipe
segma = 5.6697e-8
epislon_ab = 1 - rho_abir
###########################################################################################
''''' Glass Cover properties   '''
#Physical properties
r_g_i= 0.054/2
r_g_o= 0.058/2
dt_g = r_g_o - r_g_i
```

```
r_g_m= (r_g_o + r_g_i)/2.0
dA_g_i= r_g_i*GC_seg_rad*dl
dA_g_o= r_g_o*GC_seg_rad*dl
A_g_o = 2*r_g_o*np.pi*dl
k_g = 1.005
Lc = (r_g_i - r_ab_o)  #chracteristic length
#### Upper half ####
#IR radiaiton #glass transmissivity in IR is zero
rho_gir_up = [0.92]
epislon_gi_up = [0.08]
epislon_go_up = [0.08]
###lower half ####
#IR radiaiton
rho_gir_dow = [0.92]  #for bare
epislon_gi_dow = [0.08]
epislon_go_dow = [0.08]
###############
rho_G = rho_gir_up*int(GC_seg_no/4 + 1) + rho_gir_dow*int(GC_seg_no/2) + rho_gir_up
*int(GC_seg_no/4 - 1)
epislon_Go = epislon_go_up*int(GC_seg_no/4 + 1) + epislon_go_dow*int(GC_seg_no/2) +
 epislon_go_up*int(GC_seg_no/4 - 1)
epislon_Gi = epislon_gi_up*int(GC_seg_no/4 + 1) + epislon_gi_dow*int(GC_seg_no/2) +
 epislon_gi_up*int(GC_seg_no/4 - 1)
################
''''' Air outside the glass cover '''
v = 2.6                #m/s the speed of wind
h_w = (4*v**0.58)*(2*r_g_o)**(-0.42)  #h_w = 4*v**0.58 * d**-
0.42 , wher d is the diameter of the glass cover
'''''air characterstic between the glass and outside at Tavg = (294+400)/2 = 74 cel
esius = 347K'''
k_a_G= 0.02893         # thermal conductivity W/m.K
meu_g = 2.042*1E-5     # kinematic viscosity m2/s
pr_g = 0.71845
'''''air characterstic between the metal pipe and glass cover at Tavg = (T_g+ T_ab)
/2 = (373+500)/2 = 436.5 celesius = 347'''
k_a_A= 0.0371         # thermal conductivity W/m.K
meu_ab = 3.6125*1E-5  # kinematic viscosity m2/s
pr_ab = 0.7089
```

# Appendix V

# Temperature measurements

It is a challenge to measure the temperature with high accuracy because errors in the measurement readings are due to sensor nonlinearities, poor thermal contact, presence of temperature gradients, calibration drifts, radiant energy, and sensor self-heating [127]. There are four basic processes in temperature measurement [127]

1- Sensor: sensing device protect by a sheath
2- Sensor signal: the part that converts the physical changing in the sensor into an electrical signal (most types).
3- Probe: the sensor has different probe designs for various applications.
4- Measuring instrument: convert the electrical signal into a display value.

There are many types of temperature sensors. In this work, we used thermocouples, which are considered to be one of the simplest of all sensors. A thermocouple consists of two dissimilar metals types, which are called reference junction and measuring junction. The working principle is related to the physical phenomena called the Seebeck effect [122]. In the Seebeck effect, a small potential difference (mV) is generated due to the difference in temperature between two dissimilar metals. Thermocouples type K (Nickel-Chromium / Nickel-Alumel) are used in this work because they are inexpensive, reliable, accurate ($\pm$ 1 degree), and have a wide temperature range -200 ℃ to 1350 ℃ [122].

### The temperature measurement

The following are some suggested solution to minimize the temperature measurement errors [127] comes from the following:

a) **Thermal contact**
In the experimental setup, the thermocouple tip is welded using silver, see Figure IV.1, to ensure good thermal contact with the material to be measured.



Figure IV.1: Thermocouple tip is welded using silver.

b) **Condensation**
To avoid this problem, the sensor and its wiring are sealed, and the air was dry.

c) **Sensor aging**
High temperatures and chemical exposure lead to impurities, oxidation, and degrading of the sensor. Thermocouple type K is quite stable due to the Nickel content and the glass fiber twisted insulation.

d) **Delayed response in measuring value and error on the measuring instrument**

We used a single-board microcontroller with a cold-junction compensated K- thermocouple to digital converter module chip. The single-board microcontroller was an Arduino Mega [120], which was programmed using dialect features from the programming languages C and C++, see Figure IV.2. The Arduino board includes sets of analog and digital input/output pins that can be interfaced to other circuits or breadboards (Shields). The breadboard that was interfaced with the Arduino to measure the temperature is the cold-junction compensated K- thermocouple to digital converter module MAX6675 chip [121], see Figure IV.3.




Figure IV.2: Arduino Mega [120].

The MAX6675 chip is a direct digital conversion of type K-thermocouple output with cold junction compensation. This chip has a temperature reading resolution of 0.25 ℃ and exhibits accuracy of 8 least significant bits for temperature ranging from 0 °C to 700 ℃, more details of the chip specifications are in [121].

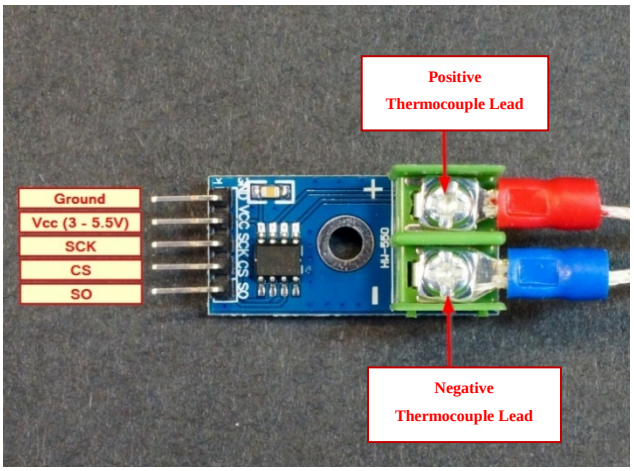



Figure IV.3: Cold-junction compensated K- thermocouple to digital converter module MAX6675 chip [128].

In our experimental setup, nine thermocouples are attached to the 9 MAX9975 chip. The temperature measurement unit of the experimental setup is shown in Figure IV.4.

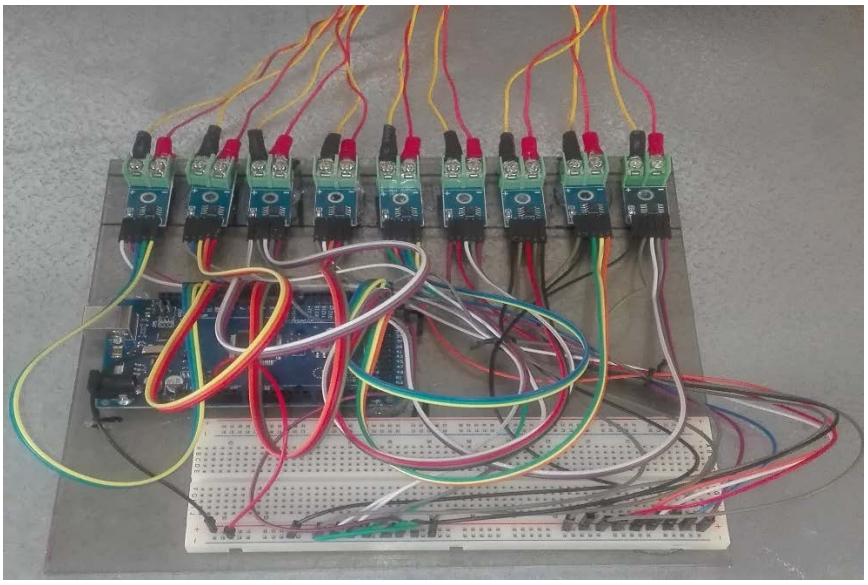


Figure IV.4: The temperature measurement unit for the experiment setup.

The Arduino code that is used to read and write the temperatures of 9 different positions in the receiver unit is as follows.

```
/* Cold-Junction-Compensated K-Thermocouple-to-
Digital Converter module MAX6675 chip
The code for reading 9 MAX6675 chips via SPI interface
 */
#include <max6675.h>    //Call max6675.h library
//For 1st MAX6675 thermocouple on absorber pipe (AP1)
int sckAP1 = 13;   // Serial clock input. connected to digital pin 13 on the microc
ontroller
int csAP1 = 12;    //Chip select. connected to digital pin 12 on the microcontrolle
r
int soAP1 = 11;    //Serial data output. connected to digital pin 11 on the microco
ntroller
MAX6675 AP1(sckAP1, csAP1, soAP1); //Create MAX665 control

//For 2nd MAX6675 thermocouple on absorber pipe (AP2)
int sckAP2 = 10;
int csAP2 = 9;
int soAP2 = 8;
MAX6675 AP2(sckAP2, csAP2, soAP2);

//For 3rd MAX6675 thermocouple on absorber pipe (AP3)
int sckAP3 = 7;
int csAP3 = 6;
int soAP3 = 5;
MAX6675 AP3(sckAP3, csAP3, soAP3);

//For 1st MAX6675 thermocouple on Outer Cavity surface (C1)
int sckC1 = 4;
int csC1 = 3;
int soC1 = 2;
MAX6675 C1(sckC1, csC1, soC1);

```

```
//For 2nd MAX6675 thermocouple on Outer Cavity surface (C2)
int sckC2 = 22;
int csC2 = 23;
int soC2 = 24;
MAX6675 C2(sckC2, csC2, soC2);

//For 3rd MAX6675 thermocouple on Outer Cavity surface (C3)
int sckC3 = 25;
int csC3 = 26;
int soC3 = 27;
MAX6675 C3(sckC3, csC3, soC3);

//For 1st MAX6675 thermocouple on Cavity Aperture (CA1)
int sckCA1 = 28;
int csCA1 = 29;
int soCA1 = 30;
MAX6675 CA1(sckCA1, csCA1, soCA1);

//For 2nd MAX6675 thermocouple on Cavity Aperture (CA2)
int sckCA2 = 31;
int csCA2 = 32;
int soCA2 = 33;
MAX6675 CA2(sckCA2, csCA2, soCA2);

//For 3rd MAX6675 thermocouple on Cavity Aperture (CA3)
int sckCA3 = 34;
int csCA3 = 35;
int soCA3 = 36;
MAX6675 CA3(sckCA3, csCA3, soCA3);

//================================================================================
//Intialization
//================================================================================
unsigned long time;
void setup() {
  Serial.begin(9600); // Set communication speed for debug window message
  Serial.println("Temperature measurement of the reciever unit of the PTC indoor");

}
//================================================================================
// Reading collection
//================================================================================
void loop() {
  //Read and write the temperature of each thermocouple modules in degree Celsius
  Serial.print("Time: ");
  time = millis();
  Serial.println(time/1000);

  Serial.print("AP1 (C) = ");
  Serial.println(AP1.readCelsius());
  //Serial.print("  ");

  Serial.print("AP2 (C) = ");
  Serial.println(AP2.readCelsius());
 // Serial.print("  ");

  Serial.print("AP3 (C) = ");
  Serial.println(AP3.readCelsius());
 // Serial.print("  ");

  Serial.print("C1 (C) = ");
  Serial.println(C1.readCelsius());
 // Serial.print("  ");

  Serial.print("C2 (C) = ");
  Serial.println(C2.readCelsius());
```

```
94. //  Serial.print("  ");
95.
96.   Serial.print("C3 (C) = ");
97.   Serial.println(C3.readCelsius());
98.   //Serial.print("  ");
99.
100.         Serial.print("CA1 (C) = ");
101.         Serial.println(CA1.readCelsius());
102.        // Serial.print("  ");
103.
104.         Serial.print("CA2 (C) = ");
105.         Serial.println(CA2.readCelsius());
106.         //Serial.print("  ");
107.
108.         Serial.print("CA3 (C) = ");
109.         Serial.println(CA3.readCelsius());
110.        // Serial.print("  ");
111.        // Serial.print("\n ");
112.         Serial.println(" ..........................................................
    ..................................................... ");
113.         delay(300000);  // Read and write every 10 minutes
114.       }
```